Computational studies of the hydrous defects in olivine, and iron-silicon isotope fractionation during the core-mantle segregation

A DISSERTATION
SUBMITTED TO THE FACULTY OF THE GRADUATE SCHOOL
OF THE UNIVERSITY OF MINNESOTA
BY

Tian Qin

IN PARTIAL FULFILLMENT OF THE REQUIREMENTS
FOR THE DEGREE OF
DOCTOR OF PHILOSOPHY

Renata M. Wentzcovitch

May, 2019

Acknowledgements

There are many people that have earned my gratitude for their contribution to my time in graduate school.

First of all, I would like to express my gratitude to my advisor Prof. Renata Wentzcovitch, who coaches me to think critically and carefully and how to be professional. Most of all, I thank her for the constant support during my time in graduate school.

In addition to my advisor, I would like to thank my thesis committee: Prof. David Kohlstedt, Prof. Marc Hirschmann, Prof. Laura Gagliardi for their kindly assistance, insightful comments and suggestions not only during my written exam, oral exam and final exam, but during the entirety of my graduate studies, motivating me to think more broadly about various aspects of my research.

I would also like to thank Koichiro Umemoto, Michel Lacerda Marcondes dos Santos, Gaurav Shukla, Qi Zhang, Prof. Jung-fu Lin and Prof. Nicolas Dauphas for their precious assistance and collaboration, which was fundamental to conduct my research. . Also, I thank my groupmates: Kanchan Sarkar, Joelson Cott-Garcia, Juan Valencia-Cardona, Zhen Zhang, Chenxing Luo, Ziyu Cai, Tianqi Wan, Hongjing Wang and Jingyi Zhuang for fruitful discussions on research and various other topics. In particular, I am grateful to Dr. Mehmet Topsakal for helping me to get familiar with the supercomputer clusters.

Furthermore, I am grateful to my previous advisors at the University of Science and Technology of China (USTC): Prof. Zhongqing Wu and Prof. Fang Huang for their guidance and advice, which are vital for my academic and personal development. Interaction with my colleagues at USTC is also very appreciated: Fei Wu, Chao Yao, Wenzhong Wang, Chen Zhou.

I also greatly appreciate all the graduate students, faculty members, researchers, staff

members in the Earth Sciences department. Discussions with them greatly broadened my horizons on science and world views. To name a few: Zhou Zhang, David Birlenbach, Peter Scheuermann, Tatsuro Tanioka, Gerard Salter, Molly Ray, Roman Zoss, Amanda Yourd, Avishek Rudra, Jennifer Caseres, Chao Qi, Meng Sun, Zhao Zhu, Chunyang Tang, Prof. David Yuen, Prof. Crystal Ng, and Prof. Max Bezade. In particular, I want to thank Jennifer Petrie, Stephanie Rosenthal, and Sharon Kressler, whose administrative work helped me through many complex situations.

My thanks also go out to the National Science Foundation (NSF/EAR-1161023 and NFS/EAR-1503084), Minnesota Supercomputing Institute (MSI), and Texas Advanced Computing Center, which supported and enabled my research..

During my studies at the University of Minnesota, I have been lucky to meet many great people outside of Earth sciences community: Barbara Beers, Hillis Byrnes and Matthew Byrnes for enlightening my stay in Minnesota.

Last but not least, I would like to thank my family, who supports me spiritually. In particular, my grandmother, Genwang Liu (1945-2018), parents, parents-in-law, uncle, aunt, sister and brother, and sisters-in-law. I especially want to thank my wife Liang Lin, who always encouraged me during the hard times. We went through many joys and sorrows. Also, I thank my son, Lang Qin, who gives me further reasons to thrive and succeed.

Dedication

In memory of my grandma, Genwang Liu. You left fingerprints of grace on our lives. You shan't be forgotten.

Abstract

This thesis presents a series of ab initio studies on two major topics of interest in geochemistry: a) water speciation in forsterite, and b) iron and silicon isotope fractionation among bridgmanite and metallic phases.

The first topic relates to the deep water cycle in the Earth; we studied the stability of two charge-balanced hydrous defects, $(2H)^{X}_{Mg}$ and $(4H)^{X}_{Si}$, in the forsterite. We systematically searched the possible configurations of these two defects and then included the contribution of vibrational energy and configurational entropy in the calculation of the formation energies of both defects. Our results reveal that the configurational entropy plays a key role in stabilizing the $(2H)^{X}_{Mg}$ defects, and further, the water speciation in forsterite is shown to be influenced by temperature and pressure. A Python program called "qha" has been developed to calculate the thermodynamic properties of these multi-configurational hydrous defects.

The second topic addresses the enigmatic and paradoxical Fe isotope composition found in the terrestrial basalts and the Si isotope composition of the bulk silicate Earth (BSE). The Fe and Si isotope fractionation factor between the mantle and core phases have been calculated. The mineral phases studied here include Fe-bearing bridgmanite, pure HCP Fe and an Fe-Si alloy. The different valence, structural site, spin states of Fe in bridgmanite are taken into consideration in the calculation of Fe isotope fractionation between silicate and metallic core. We show that the low spin Fe in the bridgmanite has a strong preference to enrich heavy isotopes. The simple-mass-balance calculations suggest that the core-mantle segregation can lead to the mantle being heavier in Fe isotopes compared to chondrites. The calculated Si isotope fractionation factor between silicate phase and the Fe-Si alloy suggests that the silicate phase enrich heavy Si isotopes. However, the calculated fractionation factor is much smaller than previous experimental estimation; one of the consequences is that it is difficult to match the silicon content in the core. Thus, our study suggests that the Earth might be non-chondritic in Si isotope or that calculations for the melt phases are really required for this case.

While these big questions have not been resolved, we shed light on a possible origin for the anomalous Fe isotope compositions of basalts, and the possible Si isotope composition

of the BE and BSE, and we have successfully explained some apparently controversial facts concerning hydrous defects in forsterite and clearly established a path for addressing more realistically the relative stability of hydrous defects.

Contents

List of Tables

List of Figures

Chapter 1

Introduction

Knowledge of our solar system and the Earth was accumulated significantly over the last several centuries. It is known that the Earth was formed by collisions and accretion during its very early history and underwent extensive melting to form a magma ocean because of the tremendous heat generated by planetesimal bombardments as well as the decay of the short-lived radiogenic isotopes [1]. In the meantime, the metallic core was segregated from the liquid silicate magma ocean due to the large density difference. Then, upon cooling, the silicate magma ocean gradually crystallized into a solid mantle.

Based on compositions of mantle samples, and mantle-derived melts and other constraints from the cosmochemical measurements of chondrites [2], the upper mantle rock is believed to be peridotitic in composition[3]. As most of these samples come from depths less than 200 km, it is reasonable to assume that the upper mantle (at least till 200 km) consists of peridotite, but whether a peridotitic composition can represent the remaining parts of the mantle remains contentious. Also, the content of olivine in peridotite obtained in different studies varies from 40–70% [4] to 66–74% [5]to ∼52% [6]. Among all the possible candidates, the most frequently invoked model composition is the standard "pyrolite" model which contains 60 % olivine [7]. The mineral combination derived from pyrolite model is described as follows: in the upper mantle, olivine transforms into wadsleyite at about 410 km (13-14 GPa), and wadsleyite transforms into ringwoodite at about 520 km (18 GPa). At about 660 km (23 GPa), ringwoodite breaks down into bridgmanite and ferropericlase. These depths match well with the depth of discontinuities shown in seismic reference models, such as PREM [8] and AK135 [9].

The remaining components consist mainly of garnet, clinopyroxene, and orthopyroxene. Both orthopyroxene and clinopyroxene dissolved into the garnet gradually and eventually form the majoritic garnet solid solution over a broad pressure range, which leads to changes in the slope of seismic velocity versus depth curves rather than indicating discrete discontinuities. At about 580 km depth, CaSiO3 perovskite begins to exsolve from the garnet, and eventually, all garnet dissolves into bridgmanite between about 660 and 750 km depth.

1.1 Hydrous defects in forsterite

There are also other phases in the mantle, for example, melts and fluids can also exist. In addition, there are a lot of trace elements dissolved in the structure of the minerals, among them, hydrogen might be one of the most interesting components. There is solid evidence showing that the hydrogen can stay in nominally anhydrous minerals (NAMs) as hydrous defects [10, 11, 12, 13]. In the geological literature, hydrogen or hydroxyl sometimes are simply named as 'water'. Water in the mantle could be in different states, such as fluid in subduction zones, as hydrous minerals within subducting slabs and as hydroxyl point defects in NAMs [13]. Water in minerals, even at part per million (ppm) level, could significantly influence the physical and chemical properties of their hosts, such as the strength [14, 15], ionic diffusivity [16], seismic velocity [17], deformation behavior [18, 19, 20, 21, 22], electrical conductivity [23], as well as the solidus [24] and mantle viscosity [25].

It is vital to know the incorporation mechanism from a microscopic perspective to understand the way hydrogen influences NAMs. The hydrous defects in forsterite, Mg end member of olivine, are under extensive investigation for decades. It is generally accepted that hydrogen would bind with oxygen near vacant Mg and vacant Si sites in forsterite, denoted as $(2H)^{X}_{Mg}$ and $(4H)^{X}_{Si}$, respectively, as shown in figure 1.1. However, previous studies give controversial results on whether the $(2H)^{X}_{Mg}$ or $(4H)^{X}_{Si}$ dominates the hydrogen incorporation [19, 26]. For example, the formation reaction of $(4H)^{X}_{Si}$ is lower than that of $(2H)^{X}_{Mg}$ in ab initio calculations [26] indicating that the $(4H)^{X}_{Si}$ is the dominant hydrous defect. But the relationship between the hydrogen content and water fugacity indicates that $(2H)^{X}_{Mg}$ is the dominant hydrous defect [12]. Additional evidence

from calculated Si and metal diffusivity suggest that $(2H)^{X}_{Mg}$ should be the dominant hydrous defect in olivine [27].

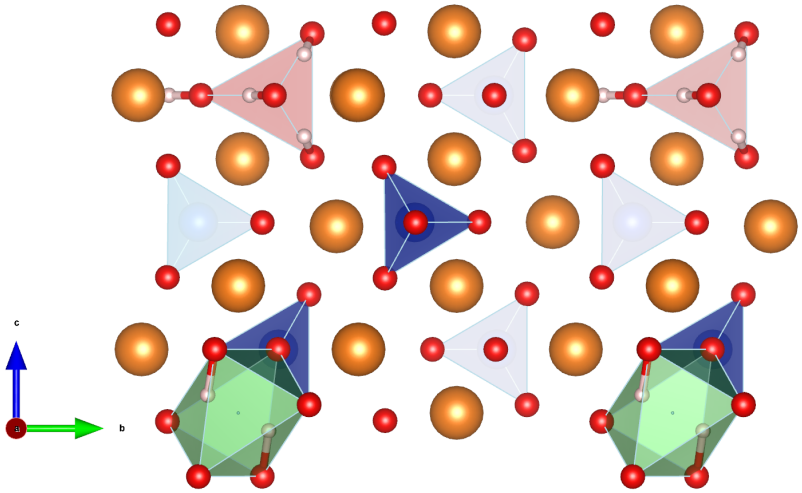

Figure 1.1: Structure of forsterite with $(4H)^{X}_{Si}$ and $(2H)^{X}_{Mg}$ defects, shown in pink and light green polyhedra, respectively. Yellow(large size), blue(middle size), and red(small size) spheres represent Mg, Si and O atoms.

More hydrous Mg sites than Si sites are needed to hold the same amount of water. Therefore the lattice configurational entropy of these defects differ, favoring the Mg defect at high temperatures. In addition, there are multiple configurations for each defect, and this can lead different internal configurational entropies. We studied the effects of the number of configurations of each defect, lattice configurational entropy and vibrational contribution on the stability of the two defects, see chapter 4 for more details.

1.2 Fe and Si isotope fractionation among mantle and core phases

In the past decades, Fe isotopic abundances have been used to study the histories of accretion and differentiation of Earth [28, 29, 30, 31, 32, 33, 34, 35, 36, 37, 38, 39]. Recent studies show that the iron in terrestrial basalts, for example, the mid-ocean ridge basalts (MORBs), enrich the heavy Fe isotope (^{56}Fe) by +0.1 ‰ relative to primitive

chondrites [40]. However, the basalts from Mars and Vesta show chondritic Fe isotopic composition within uncertainty.

There are at least three different interpretations of these observations:

- Some studies believe that the iron isotopic composition of Earth's mantle is chondritic, and the systematically isotopically heavier iron isotopic signature of terrestrial basalts are caused by the magma evolution [41, 37, 42].

- Some other studies show Fe isotopes fractionate during the core-mantle separation [32, 43] with lighter Fe isotope going into metallic core, leaving the rest of Earth isotopically heavier.

- Another alternative interpretation is Earth may have evaporated some light Fe isotope into space during accretion [31, 44]. A recent published Mg isotope study [45]supports this evaporation mechanism.

The difficulties raised are mainly due to the inaccessibility of the deep Earth. Also, it is not easy to simulate the core-mantle segregation process experimentally. One reason is it occurred under the extremely high temperature and pressure conditions, and also the exact composition of the Earth's "core" or metal phase is unknown, even though we know there must be some "light" elements alloyed with iron to match the density deficit. In addition, it is contentious whether the iron isotope composition of peridotite samples can represent the iron isotope composition of the whole mantle or even only the upper mantle. Therefore, there are many aspects yet unclear on both the silicate and metallic phases, which are both crucial to understand the origin of Fe isotope signature in the Earth and the cause of the difference between the Fe isotopic composition among Earth, Mars, and Vesta.

Fe isotope fractionation data can potentially be used as a new tool to study the light element in the core. Shahar et al. (2016) studied Fe isotope fractionation among Fe-bearing bridgmanite and various Fe alloy [34], they found that hydrogen or carbon in the alloy can cause large Fe isotope fractionation between the silicate and metal phase, while oxygen in the alloy has limited effect on the Fe isotope fractionation. In addition, a recent study shows that Ni can be the key factor to cause iron isotope fractionation in many planets [29], because Ni in the metal phase would cause the lighter isotope

enrichment in the metal phase when coexisting with Fe-bearing silicate phases. Another recent experimental study shows that light elements and Ni in the metal phase will not affect the isotope fractionation properties [30]. These discrepancies suggest the effect of light elements in the metallic phase on iron isotope composition on the mantle needs more investigations. Moreover, the iron-bearing bridgmanite model in these recent studies is oversimplified, for example, only Fe^{2+} in Mg site is considered, or use the basaltic glass to represent the mantle phase, which might not be sufficient. For example, we know the Fe can be Fe^{2+} and Fe^{3+}, and Fe^{3+} can locate in Si and Metal site and Fe^{3+} in Si site also can be transformed from high spin to low spin states between 40 and 70 GPa [46, 47]. All of these aspects could affect the fractionation properties.

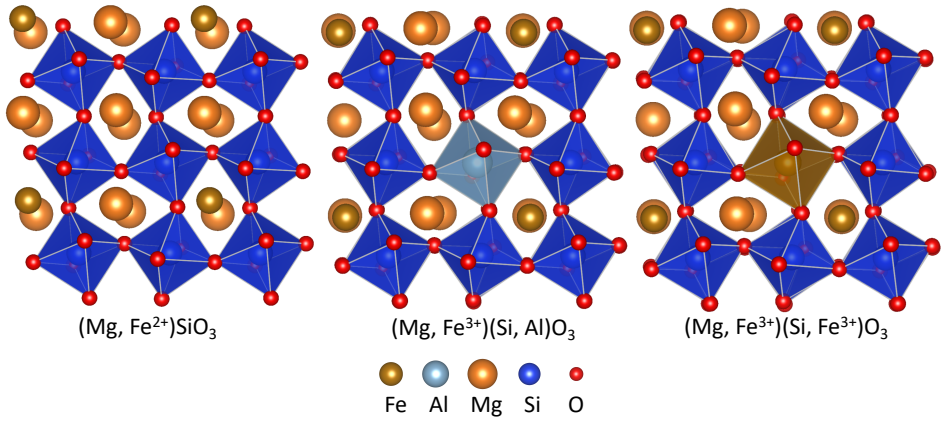

Figure 1.2: Different Fe-bearing bridgmanite models considered in the current study.

In this study, we considered the Fe in different valence states, different site and different spin states in the core-mantle segregation conditions, see figure 1.2. The results and implications are summarized in chapter 5. In addition, we investigated the iron isotope fractionation between pure metal iron and iron-silicon alloy, and the silicon isotope fractionation between bridgmanite and the iron-silicon alloy in chapter 6.

This thesis is divided into the following chapters: in chapter 2, the methods used

in the thesis, such as the density functional theory and equation of state, are introduced; in chapter 3, we summarize the method to calculate the free energy of the multi-configuration within the QHA; in chapter 4, the study of the stability of two important hydrous defects,$(2H)^{X}_{Mg}$ and $(4H)^{X}_{Si}$, in forsterite are investigated. After considering entropic and vibrational contributions, the results show that the stability of these two defects is a function of pressure and temperature, more specifically, the $(2H)^{X}_{Mg}$ defects dominate at mantle conditions; in chapter 5, the iron isotope fractionation between various Fe-bearing bridgmanite and metal iron at the proposed core-mantle segregation condition are studied. The effects of valence states, different sites, and spin states are all considered in the study and the results show that core-mantle segregation could leave the detectable imprint on the iron isotope composition of the bulk silicate earth; in chapter 6, fractionation of silicon isotopes between Fe-Si alloy and bridgmanite at mantle conditions are reported.

Chapter 2

Theoretical methods

This chapter briefly addresses some theoretical backgrounds of *ab initio* or first-principles calculations. Starting from the fundamental quantum mechanics principles, followed by some common approximations in the practical calculations, and then followed by the density functional perturbation theory (DFPT) that has been used to calculate the vibrational density of state (VDOS), which plays an important role to get accurate thermodynamic properties. They are followed by the brief introduction of the equation of state (EOS) and quasi-harmonic approximation (QHA). At last, the method to calculate the equilibrium stable isotope fractionation factor is briefly introduced.

2.1 Basics of *ab initio* calculations

This section starts with the basic equation in quantum mechanics, namely, the Schrödinger equation. There is no exact solution for almost any practical systems, therefore, many approximations are adopted to make the calculation feasible and within reasonable accuracy.

2.1.1 Schrödinger equation and wave functions

In classical mechanics, the particles of macroscopic system obey the Newtonian laws, the exact position and momentum can be measured accurately or can be predicted if the initial status, such as the position and velocity, of the particle are known. However, the particles in the microscopic systems were observed disobey the Newtonian laws, but

according to the laws of some form of wave motions, nowadays, we know it follows the Schrödinger equation.

2.1.2 The Born-Oppenheimer approximation

The Hamiltonian of a many-body system consisting of nuclei and electrons can be expressed explicitly as:

$$\hat{H} = -\frac{\hbar^2}{2m_e}\sum_i \nabla_i^2 + \frac{1}{2}\sum_{i\neq j}\frac{e^2}{|\mathbf{r}_i - \mathbf{r}_j|} + \sum_{i,\alpha}\frac{Z_\alpha e^2}{|\mathbf{r}_i - \mathbf{R}_\alpha|} - \frac{\hbar^2}{2M_\alpha}\sum_\alpha \nabla_\alpha^2 + \frac{1}{2}\sum_{\alpha\neq\beta}\frac{Z_\alpha Z_\beta e^2}{|\mathbf{R}_\alpha - \mathbf{R}_\beta|} \tag{2.1}$$

where the index i, j run on electrons, α, β on nuclei; $\mathbf{r}$ and $\mathbf{R}$ denotes the positions of electrons and nuclei, respectively. m and M denotes the masses of electron and nuclei. Z_α is the atomic number of nucleus α.

The first term of equation (2.1) is the kinetic energy of electrons (sometimes represented as $\hat{T}_\mathbf{r}$), the second term is the interactions among the electrons ($\hat{V}_{ee}$), the third term is the Coulomb potential acting on the electrons ($\hat{V}_{ext}$), the fourth term represents the kinetic energy of nuclei ($\hat{T}_\mathbf{R}$), and the last term is the Coulomb interactions among the ions ($\hat{V}_{II}$).

The solution of this system can be found by solving the eigenvalue problem by the time-independent Schrödinger equation:

$$\hat{H}\Psi(\mathbf{r},\mathbf{R}) = E\Psi(\mathbf{r},\mathbf{R}), \tag{2.2}$$

where $\Psi(\mathbf{r},\mathbf{R})$ is the total wave function of the system. In principle, all the physical properties can be derived if this Schrödinger equation can be solved exactly. The exact solution of equation (2.2) is not possible for most real systems. However, by using some approximations, this equation can be solved at reasonable accuracy. For example, as the electrons are much lighter than the nuclei (the mass of a proton is about 1836 times the mass of an electron), the nuclei move much slower than the electrons. It is reasonable to separate the movement of nuclei and electrons. To a good approximation, one can consider the electrons in a molecule to be moving in the field of fixed nuclei. Then the electronic and ionic degrees of freedom can be decoupled within the Born-Oppenheimer approximation [48] or adiabatic approximation.

Within the Born-Oppenheimer approximation, the fourth term in equation (2.1), the kinetic energy of the nuclei, can be neglected; the last term, the repulsion between the nuclei, can be considered as constant. Any constant added to an operator only adds to the operator eigenvalues and does not affect the operator eigenfunctions. The remaining terms in equation (2.1) describing the motion of electrons in the field of nuclei, and are called the electronic Hamiltonian:

$$\hat{H}_{elec} = -\frac{\hbar^2}{2m_e}\sum_i \nabla_i^2 + \frac{1}{2}\sum_{i\neq j}\frac{e^2}{|\mathbf{r}_i - \mathbf{r}_j|} + \sum_{i,\alpha}\frac{Z_\alpha e^2}{|\mathbf{r}_i - \mathbf{R}_\alpha|} \tag{2.3}$$

The solution of a Schrödinger equation involving the electronic Hamiltonian is the electronic wave function:

$$\hat{H}_{elec}\psi_{\mathbf{R}}(\mathbf{r}) = E_{elec}\psi_{\mathbf{R}}(\mathbf{r}) \tag{2.4}$$

here the $\psi_{\mathbf{R}}(\mathbf{r})$ is the electronic wave function, which describes the motion of the electrons and explicitly depends on the coordinates of electrons, and depends parametrically on the coordinates of the nuclei.

The energy E_{elec} is the electronic energy; the total energy for fixed nuclei must also include the nuclear repulsion part:

$$E_{total} = E_{elec} + \sum_{\alpha\neq\beta}\frac{Z_\alpha Z_\beta e^2}{|\mathbf{R}_\alpha - \mathbf{R}_\beta|}. \tag{2.5}$$

In addition, the total wave function can be expressed as

$$\Psi(\mathbf{r}, \mathbf{R}) = \Phi(\mathbf{R})\psi_{\mathbf{R}}(\mathbf{r}), \tag{2.6}$$

where the $\Phi(\mathbf{R})$ and $\psi_{\mathbf{R}}(\mathbf{r})$ are the ionic and electronic wave functions, respectively.

The significance of the Born-Oppenheimer approximation is to separate the movement of electrons and nuclei, and simplify the Schrödinger equation, but equation (2.4) is still too complicated to solve exactly due to the electron-electron interactions. In order to study the real system, a more advanced framework, namely, density functional theory (DFT) is adopted to perform practical calculations.

2.2 Density functional theory (DFT)

DFT has been the most widely used methods in the *ab initio* calculations to study the properties of interested condensed matter systems, such as crystalline, molecules, proteins, two-dimensional materials. In the framework of DFT, the many-body system is described using the density of the particle instead of using the many-body wave function. The DFT is based on the Hohenberg-Kohn (HK) theorem[49], which claims that all properties of a system can be considered to be functionals of its ground state density. Together with the Born-Oppenheimer approximation[48] and Kohn-Sham ansatz[50], the practical DFT calculations are available.

2.2.1 The Hohenberg-Kohn (H-K) theorem

DFT provides a practical way to describe the ground state properties of a system in terms of the ground state electronic charge density. DFT was proven to be an exact theory of many-body system by Hohenberg and Kohn [49] in 1964. The Hohenberg-Kohn theorems relate to any system consisting of electrons moving under the influence of an external potential The theory is based upon two theorems.

The first theorem states as the ground-state energy from Schrödinger equation is a unique functional of the electron density. Another way to restate this theorem is that the ground-state electron density uniquely determines all properties, including the energy and wave function, of the ground state.

Although the first H-K theorem rigorously proves that a functional of the electron density exists and can be used to solve the Schrödinger equation, the theorem can not give what the functional is. In addition, the second theorem add more constraints on the property of the functional by indicating that the electron density that minimizes the energy of the overall functional is the true electron density corresponding to the full solution of the Schrödinger equation.

The proof of the first theorem proceeded by *reductio ad absurdum*. Imagine there exist two different potentials $V_{ext}^{(1)}(\mathbf{r})$ and $V_{ext}^{(2)}(\mathbf{r})$ giving rise to the same ground state electron density, $n(\mathbf{r})$. $V_{ext}^{(1)}(\mathbf{r})$ and $V_{ext}^{(2)}(\mathbf{r})$ belong to distinct Hamiltonians $\hat{H}^{(1)}(\mathbf{r})$ and $\hat{H}^{(2)}(\mathbf{r})$, which give rise to distinct wave functions $\Psi^{(1)}(\mathbf{r})$ and $\Psi^{(2)}(\mathbf{r})$, respectively.

According to the variational principle, no wave function can give an energy that is

less than the energy of $\Psi^{(1)}(\mathbf{r})$ for $\hat{H}^{(1)}(\mathbf{r})$.

$$E^{(1)} = \langle \Psi^{(1)} | \hat{H}^{(1)}(\mathbf{r}) | \Psi^{(1)} \rangle < \langle \Psi^{(2)} | \hat{H}^{(1)}(\mathbf{r}) | \Psi^{(2)} \rangle \tag{2.7}$$

Assuming the ground state is non-degenerate, the inequality strictly holds. The right side in the equation (2.7) can be rewritten as

$$\begin{aligned} \langle \Psi^{(2)} | \hat{H}^{(1)}(\mathbf{r}) | \Psi^{(2)} \rangle &= \langle \Psi^{(2)} | \hat{H}^{(2)}(\mathbf{r}) | \Psi^{(2)} \rangle + \langle \Psi^{(2)} | \hat{H}^{(1)}(\mathbf{r}) - \hat{H}^{(2)}(\mathbf{r}) | \Psi^{(2)} \rangle \\ &= E^{(2)} + \int d\mathbf{r} [V_{ext}^{(1)}(\mathbf{r}) - V_{ext}^{(2)}(\mathbf{r})] n_0(\mathbf{r}) \end{aligned} \tag{2.8}$$

Interchanging the two labels in equation (2.8), we find that

$$\begin{aligned} \langle \Psi^{(1)} | \hat{H}^{(2)}(\mathbf{r}) | \Psi^{(1)} \rangle &= \langle \Psi^{(1)} | \hat{H}^{(1)}(\mathbf{r}) | \Psi^{(1)} \rangle + \langle \Psi^{(2)} | \hat{H}^{(1)}(\mathbf{r}) - \hat{H}^{(2)}(\mathbf{r}) | \Psi^{(2)} \rangle \\ &= E^{(1)} + \int d\mathbf{r} [V_{ext}^{(2)}(\mathbf{r}) - V_{ext}^{(1)}(\mathbf{r})] n_0(\mathbf{r}) \end{aligned} \tag{2.9}$$

Adding equation (2.8) and equation (2.9) leads to the inconsistency

$$E^{(1)} + E^{(2)} < E^{(2)} + E^{(1)} \tag{2.10}$$

Thus, the first H-K theorem has been proven.

For the second H-K theorem, there exists a universal functional $F[n(\mathbf{r})]$ of the density, independent of the external potential $V_{ext}(\mathbf{r})$, such that the global minimum value of the energy functional $E[n(\mathbf{r})] \equiv \int n(\mathbf{r}) V_{ext}(\mathbf{r}) d\mathbf{r} + F[n(\mathbf{r})]$ is the exact ground state energy of the system and the exact ground state electron density $n(\mathbf{r})$ minimizes this functional. Thus the exact ground state energy and density are fully determined by the functional $E[n(\mathbf{r})]$.

The universal functional $F[n(\mathbf{r})]$ can be written as

$$F[n(\mathbf{r})] \equiv T[n(\mathbf{r})] + E_{int}[n(\mathbf{r})], \tag{2.11}$$

where the $T[n(\mathbf{r})]$ is the kinetic energy and $E_{int}[n(\mathbf{r})]$ is the interaction energy of the system. The treatment of the kinetic and internal potential energies are the same for all system.

According to variational principle, for any wave function Ψ', the energy functional $E[\Psi']$ can be represented as:

$$E[\Psi'] \equiv \langle \Psi' | \hat{T} + \hat{V}_{int} + \hat{V}_{ext} | \Psi' \rangle \tag{2.12}$$

The energy functional $E[\Psi']$ has its global minimum value only when Ψ' is the ground state wave function Ψ_0, with the number of particles is kept constant.

$$N[n(\mathbf{r})] \equiv \int n(\mathbf{r}) d\mathbf{r} = N \tag{2.13}$$

where N is the number of particles in the system.

According to the first H-K theorem, Ψ' must correspond to a ground state with particle density $n'(\mathbf{r})$ and external potential $V'_{ext}(\mathbf{r})$, then $E[\Psi']$ is a functional of $n'(\mathbf{r})$. According to variational principle, if the density $n'(\mathbf{r})$ is not the ground state, then $E[n'(\mathbf{r})] > E[n_0(\mathbf{r})]$, as shown below :

$$\begin{aligned} E[\Psi'] &= \langle \Psi' | \hat{T} + \hat{V}_{int} + \hat{V}_{ext} | \Psi' \rangle \\ &= E[n'(\mathbf{r})] \\ &= \int n'(\mathbf{r}) V'_{ext}(\mathbf{r}) d\mathbf{r} + F[n'(\mathbf{r})] \\ &> E[\Psi_0] \\ &= \int n_0(\mathbf{r}) V_{ext}(\mathbf{r}) d\mathbf{r} + F[n_0(\mathbf{r})] \\ &= E[n_0(\mathbf{r})] \end{aligned} \tag{2.14}$$

Thus the energy functional $E[n(\mathbf{r})]$ evaluated for the correct ground state electron density $n_0(\mathbf{r})$ is indeed lower than the value of this functional for any other density $n(\mathbf{r})$. Therefore by minimizing the total energy functional of the system with respect to variations in the density $n(\mathbf{r})$, the exact ground state electron density and energy are known.

In spite of these conceptually appealing developments, the practical use fo the DFT was still not possible due to the universal functional $F[n(\mathbf{r})]$ is unknown. This difficulty was overcome by Kohn and Sham[50] in 1965, who proposed the well known Kohn-Sham ansatz.

2.2.2 The Kohn-Sham equation

The Kohn-Sham ansatz replaces the many-body interacting system with an auxiliary independent-particle system and assume the two systems have exactly ground state electron density. This fictitious non-interacting system can be described with the single particle Schrödinger equation in an *effective local potential* $V_{KS}(\mathbf{r})$[50]. The Hamiltonian of this auxiliary independent-particle system is

$$\hat{H}_{KS} = -\frac{\hbar^2}{2m_e}\nabla^2 + V_{KS}(\mathbf{r}) \tag{2.15}$$

For a system with N independent electrons, the ground state is obtained by solving N one-electron Schrödinger equations,

$$\hat{H}_{KS}\psi_i(\mathbf{r}) = \varepsilon_i\psi_i(\mathbf{r}) \tag{2.16}$$

where the ε_i are the eigenvalues of the Kohn-Sham Hamiltonian. The wave functions ψ_i are the eigenfunctions of the auxiliary fictitious non-interacting system, therefore, these wave functions have no direct physical meaning.

Then the electron density of the auxiliary system is constructed from:

$$n(\mathbf{r}) = \sum_{i=1}^{N} |\psi_i(\mathbf{r})|^2 \tag{2.17}$$

The universal functional $F[n(\mathbf{r})]$ can be defined as

$$F[n(\mathbf{r})] = T[n(\mathbf{r})] + E_H[n(\mathbf{r})] + E_{XC}[n(\mathbf{r})] \tag{2.18}$$

The first term of equation (2.18) is the kinetic energy of the non-interacting electrons, which can be calculated from:

$$T[n(\mathbf{r})] = -\frac{\hbar^2}{2m_e}\sum_{i=1}^{N}\langle\psi_i(\mathbf{r})|\nabla_i^2|\psi_i(\mathbf{r})\rangle = -\frac{\hbar^2}{2m_e}\sum_{i=1}^{N}\int \psi_i(\mathbf{r})^*\nabla_i^2\psi_i(\mathbf{r})d\mathbf{r} \tag{2.19}$$

The second term is the Hartree functional, which contains the classic electrostatic

energy of the electron density interacting with itself:

$$E_H[n(\mathbf{r})] = \frac{e^2}{2}\int\int \frac{n(\mathbf{r})n(\mathbf{r}')}{|\mathbf{r}-\mathbf{r}'|}d\mathbf{r}d\mathbf{r}' \tag{2.20}$$

And the third term is the exchange-correlation energy, which accounts for all the effects due to the interaction of electrons. The exchange-correlation energy is defined as the difference of the energies between the real interacting many-body system and the fictitious non-interacting system.

The ground state energy of a many-electron system can be obtained by minimizing the energy functional $E[n(\mathbf{r})] = F[n(\mathbf{r})] + \int n(\mathbf{r})V_{ext}(\mathbf{r})d\mathbf{r}$ with the constrain that the number of the electrons unchanged.

$$\delta\left\{F[n(\mathbf{r})] + \int n(\mathbf{r})V_{ext}(\mathbf{r})d\mathbf{r} - \mu\left(\int n(\mathbf{r})dr - N\right)\right\} = 0 \tag{2.21}$$

where μ is the Lagrange multiplier, the physical meaning here is the chemical potential.

From equation (2.21), we get the

$$\begin{aligned}\mu &= \frac{\delta F[n(\mathbf{r})]}{\delta n(\mathbf{r})} + V_{ext}(\mathbf{r}) \\ &= \frac{\delta T[n(\mathbf{r})]}{\delta n(\mathbf{r})} + \frac{\delta E_H[n(\mathbf{r})]}{\delta n(\mathbf{r})} + \frac{\delta E_{XC}[n(\mathbf{r})]}{\delta n(\mathbf{r})} + V_{ext}(\mathbf{r})\end{aligned} \tag{2.22}$$

The last three terms in equation (2.22) is defined as the Kohn-Sham potential V_{KS}

$$\begin{aligned}V_{KS} &= \frac{\delta E_H[n(\mathbf{r})]}{\delta n(\mathbf{r})} + \frac{\delta E_{XC}[n(\mathbf{r})]}{\delta n(\mathbf{r})} + V_{ext}(\mathbf{r}) \\ &= e^2\int \frac{n(\mathbf{r}')}{|\mathbf{r}-\mathbf{r}'|}d\mathbf{r}' + \frac{\delta E_{XC}[n(\mathbf{r})]}{\delta n(\mathbf{r})} + V_{ext}(\mathbf{r})\end{aligned} \tag{2.23}$$

The equation (2.16), equation (2.17) and equation (2.23) are known as Kohn-Sham equations. Through the Kohn-Sham approach, the many-body interacting system can be solved using a fictitious non-interacting system in an effective potential V_{KS}, However, these single particle Schrödinger -like equations are highly nonlinear because the effective potential V_{KS} depends on its own solutions. Due to these reasons, the Kohn-Sham equations must be solved self-consistently.

Up to this stage, the Kohn-Sham equations are still unsolvable due to the form of the exchange-correlation energy functional $E_{KS}n(\mathbf{r})$ In the equation (2.23) is unknown. Thus a further approximation on $E_{KS}n(\mathbf{r})$ has to be adopted to make the DFT a practical tool for *ab-initio* or first-principles calculations.

Local density approximation (LDA) and generalized gradient approximation (GGA)

In order to make the Kohn-Sham equation solvable, the exchange-correlation term can be approximated as a local or nearly local functional of the electron density:

$$E_{XC}[n(\mathbf{r})] = \int n(\mathbf{r})\epsilon_{XC}[n(\mathbf{r}), r]d\mathbf{r}, \tag{2.24}$$

where the $\epsilon_{XC}[n(\mathbf{r}), r]$ is the exchange-correlation energy per electron at point $\mathbf{r}$, and this energy depends on the density $n(\mathbf{r})$ in the vicinity the point $\mathbf{r}$. According to Kohn and Sham, the exchange-correlation energy per electron at a point $\mathbf{r}$ is close to the limit of a homogeneous electrons gas, this is known as the local density approximation (LDA). The total exchange-correlation functional $E_{XC}^{LDA}[n(\mathbf{r})]$ can be represented as:

$$E_{XC}^{LDA}[n(\mathbf{r})] = \int n(\mathbf{r})\epsilon_{XC}^{hom}[n(\mathbf{r})]d\mathbf{r}. \tag{2.25}$$

where the $\epsilon_{XC}^{hom}[n(\mathbf{r})]$ is the exchange energy density for the homogeneous electron gas, and it is a function of the electron density alone.

The $\epsilon_{XC}^{hom}[n(\mathbf{r})]$ can be further decomposed into exchange energy density $\epsilon_{X}^{hom}[n(\mathbf{r})]$ and correlation energy density $\epsilon_{C}^{hom}[n(\mathbf{r})]$. Thus the exchange-correlation energy functional can be decomposed into exchange energy functional $E_{X}^{LDA}[n(\mathbf{r})]$ and correlation energy function $E_{C}^{LDA}[n(\mathbf{r})]$, respectively. The $\epsilon_{X}^{hom}[n(\mathbf{r})]$ can be expressed analytically while the $\epsilon_{C}^{hom}[n(\mathbf{r})]$ does not have an exact analytical form, but can be calculated based on quantum Monte Carlo simulations [51]. Depending on the analytic forms used for $\epsilon_{C}^{hom}[n(\mathbf{r})]$, many different local density approximations were proposed, for example, Perdew-Zunger [52] and Perdew-Wang [53].

LDA gives the correct sum rule to the exchange-correlation hole in spite of it is very simple. The LDA has proven to be a good approximation to determine structural

and vibrational properties of metals, semiconductors and insulators. However, LDA makes large errors in predicting the band gaps for semiconductors and insulators. To overcome these, further approximations of the exchange-correlation energy functional beyond LDA by adding gradient corrections to the density, known as the generalized gradient approximation[54], given by

$$E_{XC}^{GGA} = \int n(\mathbf{r})\epsilon_{XC}^{hom}[n(\mathbf{r}), |\nabla n(\mathbf{r})|]d\mathbf{r}. \tag{2.26}$$

The GGA improves the estimation of the energy band gap in semiconductors, and insulators, but it does not work very well for the structural and elastic properties of the solids as the LDA does. For example, according to many static calculations, LDA normally underestimate the volume and overestimate the elastic properties, while GGA overestimates the volume and underestimate the elastic properties. Without considering the contributions from vibrational effects, the error of both LDA and GGA are within few percentages, However, the vibrational energy would increase the volume at high temperature, for example, the calculated volume of the common minerals in the mantle would increase about 2% [55]. Therefore, after considering the vibrational energy, the LDA results of volume and elastic properties match well with the experimental data, while GGA will further overestimate volume and underestimate the elastic properties. Overall, LDA is better to study the minerals in the mantle condition.

Nevertheless, for the system has localized and strongly correlated electrons, such as transition metal oxides, neither GGA and LDA perform well, this leads to other approximations beyond LDA and GGA, such as LDA+U method to account for the strong correlations of d electrons in transition elements and f electrons in lanthanide and actinides.

Solving Kohn-Sham Equations

As mentioned in the previous context, the Kohn-Sham equations can only be solved self-consistently due to the effective Kohn-Sham potential, V_{KS}, are closely related with the electron density $n(\mathbf{r})$. The self-consistency loop of the calculation is shown in figure 2.1.

The calculation process starts with a trial electron density, which normally built

from the superposition of the atomic electron density. Then the effective Kohn-Sham potential can be created from the initial trial electron density. After solving the Kohn-Sham equations, the new electron density can be generated from the newly solved wave functions. Then the self-consistent conditions are checked. The conditions can be the change of the electron density or total energy or total force less than the chosen threshold, or the combination of some of these individual conditions. If the self-consistent criteria are not fulfilled, a new iteration will start with a new electron density, which is normally built from mixing the newly calculated electron density with the electron density from previous iterations. This loop calculations continue till self-consistency is reached, then various quantities can be calculated, such as the total energy, electron density, the effective Kohn-Sham potential, forces, stress.

2.2.3 The Bloch theorem

Atoms form an infinite periodic structure in a perfect crystal, thus the external potential is also periodic.

$$V_{ext}(\mathbf{r}) = V_{ext}(\mathbf{r} + \mathbf{R}), \tag{2.27}$$

where $\mathbf{R}$ is the translational vector, which consists of an integer linear combination of three lattice vectors of the primitive unit cell of the crystal ($\mathbf{R} = n_1\mathbf{a_1} + n_2\mathbf{a_2} + n_3\mathbf{a_3}$, $\mathbf{a_i}$ are the lattice vectors and n_i are any integers).

The solution of the periodic system must satisfy a fundamental property called Bloch's theorem, which sate that the solution can be expressed as a sum of terms with the form

$$\psi_{\mathbf{k}} = \exp(i\mathbf{k}\cdot\mathbf{r})u_{\mathbf{k}}(\mathbf{r}), \tag{2.28}$$

where $u_{\mathbf{k}}(\mathbf{r})$ is periodic in space with the same periodicity as the supercell and have the relationship of $u_{\mathbf{k}}(\mathbf{r}) = u_{\mathbf{k}}(\mathbf{r}+\mathbf{R})$, $\mathbf{k}$ is the (crystal) momentum, or electron wave vector within the first Brillouin Zone.

As $u_{\mathbf{k}}(\mathbf{r})$ is periodic in space, it can be expand in terms of a special set of plane waves to simplify the calculation:

$$u_{\mathbf{k}}(\mathbf{r}) = \sum_{\mathbf{G}} c_{\mathbf{G}} \exp[i\mathbf{G}\cdot\mathbf{r}] \tag{2.29}$$

where the summation is over all vectors defined by $\mathbf{G} = m_1\mathbf{b_1} + m_2\mathbf{b_2} + m_3\mathbf{b_3}$, m_i are integers, and $\mathbf{b_i}$ are the so called reciprocal lattice vectors defined as

$$\begin{aligned}
\mathbf{b_1} &= 2\pi \frac{\mathbf{a_2} \times \mathbf{a_3}}{\mathbf{a_1} \cdot (\mathbf{a_2} \times \mathbf{a_3})} \\
\mathbf{b_2} &= 2\pi \frac{\mathbf{a_3} \times \mathbf{a_1}}{\mathbf{a_2} \cdot (\mathbf{a_3} \times \mathbf{a_1})} \\
\mathbf{b_3} &= 2\pi \frac{\mathbf{a_1} \times \mathbf{a_2}}{\mathbf{a_3} \cdot (\mathbf{a_1} \times \mathbf{a_2})}
\end{aligned} \tag{2.30}$$

Combing the equation (2.28) and equation (2.29) gives

$$\psi_{\mathbf{k}}(\mathbf{r}) = \sum_{\mathbf{G}} c_{\mathbf{k}+\mathbf{G}} \exp[i(\mathbf{k}+\mathbf{G}) \cdot \mathbf{r}]. \tag{2.31}$$

This equation requires a summation over an infinite number of possible values of $\mathbf{G}$, which cannot be achieved for practical calculations. However, the functions apprearing in equation (2.31) have a simple interpretation as solutions of the Schrödinger equation:

$$E = \frac{\hbar^2}{2m_e} |\mathbf{k}+\mathbf{G}|^2 \tag{2.32}$$

It is reasonable to expect that the solutions with lower energies are more physically important than solutions with high energies. In practice, an energy cut-off, $E_{cut} = \frac{\hbar^2}{2m} G_{cut}^2$, is set to truncate the infinite sum above to include only solutions with kinetic energies less than this value.

$$\psi_{\mathbf{k}}(\mathbf{r}) = \sum_{|\mathbf{k}+\mathbf{G}|<G_{cut}} c_{\mathbf{k}+\mathbf{G}} \exp[i(\mathbf{k}+\mathbf{G}) \cdot \mathbf{r}]. \tag{2.33}$$

The energy cut-off value and the $\mathbf{k}$-vector grid need to be set before performing calculations, one can start with a series of testing calculations to determine the appropriate $\mathbf{k}$-vector grid and energy cutoff value.

2.2.4 Pseudopotential method

As the core electrons in atoms are associated with rapidly oscillating wave functions, large energy cutoffs must be used to get accurate results in the calculations. But most

of the properties we are interested in, such as chemical bonding and other physical characteristics are dominated by the less tightly bound valence electrons. Thus, core electrons are not important from this perspective and would consume significant computational resources. To overcome this circumstance, pseudopotential method has been adopted as it can reduce the computational cost substantially.

The valence electrons are considered moving in an effective potential produced by the core and core electrons. The goal of using the pseudopotential method is to reproduce all relevant properties outside the core region within a good accuracy compared with the all-electron calculation results. What a pseudopotential do in the calculation is to replace the electron density from a chosen set of core electrons with a smoothed density, which selected to match various important physical properties of the true ion core. This is the so-called frozen core approximation. And because of the smoothed density in the pseudopotential method, A smaller energy cutoff is required in the calculation, which also means less computational resources are needed.

There are several types of pseudopotentials are widely used in practice, such as the norm-conserving pseudopotentials [56, 57] and ultrasoft pseudopotentials [58, 59]. projector augmented-wave method [60, 61, 62], most of the time, these methods produce promising results. In this study, the norm-conserving and ultrasoft pseudopotentials have been used in the calculations.

2.3 Phonon calculations

A common criticism about DFT calculations is the properties obtained are static, or there is no temperature effect considered. There are a lot of situations we want to study the properties of a material at the ambient condition or higher temperature, such as the conditions in the mantle. One important fact is atoms in the material actually vibrate near their equilibrium positions. The vibrations contribute to the material's energy even at 0 K via the so-called zero-point energy. Furthermore, the vibrations can be measured experimentally using spectroscopy and be calculated theoretically. In this section, the basic theory about calculating the frequencies of vibrations (also named as phonon) are briefly introduced.

The Born-Oppenheimer energy surface, $E(\mathbf{R})$, can be expanded in a Taylor series,

$$E(\mathbf{R}) = E(\mathbf{R})_0 + \sum_I \frac{\partial E(\mathbf{R})}{\partial \mathbf{R}_I}\mathbf{R}_I + \frac{1}{2}\sum_{I,J}\frac{\partial^2 E(\mathbf{R})}{\partial \mathbf{R}_I \partial \mathbf{R}_J}\mathbf{R}_I\mathbf{R}_J + \cdots \tag{2.34}$$

where the R_I denotes the coordinate of the I^{th} nucleus. Only the first three terms matters in the harmonic approximation. The first derivative term is zero because it is evaluated at the equilibrium state and in the energy minimum state, namely, $\frac{\partial E(\mathbf{R})}{\partial \mathbf{R}_I} \equiv 0$. The second derivative in the third term is called the Hessian matrix, and it is the key element to calculate the vibrational frequencies, which given by the following equation:

$$\det\left|\frac{1}{\sqrt{M_I M_J}}\frac{\partial^2 E(\mathbf{R})}{\partial \mathbf{R}_I \partial \mathbf{R}_J} - \omega^2\right| = 0 \tag{2.35}$$

where $M_{I/J}$ are the mass of the I^{th}/J^{th} nucleus.

Thus the calculation of vibrational frequencies relies on the first and second derivatives of the energy surface $E(R)$, which can be accomplished using the Hellmann-Feynman theorem[63].

The Hamiltonian in the Born-Oppenheimer approximation of the system with interacting electrons moving in the field of fixed nuclei is given by:

$$\hat{H}_{BO} = -\frac{\hbar^2}{2m_e}\sum_i \nabla_i^2 + \frac{1}{2}\sum_{i\neq j}\frac{e^2}{|\mathbf{r}_i - \mathbf{r}_j|} - \sum_{i,I}\frac{Z_I e^2}{|\mathbf{r}_i - \mathbf{R}_I|} + \frac{1}{2}\sum_{I\neq J}\frac{Z_I Z_J e^2}{|\mathbf{R}_I - \mathbf{R}_J|} \tag{2.36}$$

According to the Hellmann-Feynman theorem, the first derivative of the eigenvalues of a Hamiltonian equals the expectation value of the derivative of the Hamiltonian. In equation form, for the eigenvalue equation: $H_\lambda \Psi_\lambda = E_\lambda \Psi_\lambda$, we have: $\frac{\partial E_\lambda}{\partial \lambda} = \langle \Psi_\lambda | \frac{\partial H_\lambda}{\partial \lambda} | \Psi_\lambda \rangle$. Therefore, the force acting on the I^{th} nucleus can be given by:

$$\begin{aligned}
\mathbf{F}_I &= -\frac{\partial E(\mathbf{R})}{\partial \mathbf{R}_I} \\
&= -\langle \Psi(\mathbf{R}) | \frac{\partial \hat{H}_{BO}(R)}{\partial \mathbf{R}_I} | \Psi(\mathbf{R}) \rangle \\
&= -\int n_{\mathbf{R}}(\mathbf{r})\frac{\partial V_{ext}(\mathbf{r})}{\partial \mathbf{R}_I} dr - \frac{\partial E_N(\mathbf{R})}{\partial \mathbf{R}_I}
\end{aligned} \tag{2.37}$$

where $V_{ext}(r) = \sum_{i,I} \frac{Z_I e^2}{|\mathbf{r}_i - \mathbf{R}_I|}$, which denotes the electron-nucleus interaction, and $E_N(\mathbf{R}) = \frac{1}{2}\sum_{I \neq J} \frac{Z_I Z_J e^2}{|\mathbf{R}_I - \mathbf{R}_J|}$, which denotes the electrostatic interaction between nuclei. $n_{\mathbf{R}}(r)$ is the ground-state electron charge density corresponding to the $\mathbf{R}$, nuclear configurations, we use $n(\mathbf{r})$ in the context.

Thus the Hessian of $E(\mathbf{R})$ can be estimated through Hellmann-Feynmann theorem by:

$$\begin{aligned} \frac{\partial^2 E(\mathbf{R})}{\partial \mathbf{R}_I \partial \mathbf{R}_J} &\equiv -\frac{\partial \mathbf{F}_I}{\partial \mathbf{R}_J} \\ &= \int \frac{\partial n(\mathbf{r})}{\partial \mathbf{R}_J} \frac{\partial V_{ext}(\mathbf{r})}{\partial \mathbf{R}_I} d\mathbf{r} + \int n(\mathbf{r}) \frac{\partial^2 V_{ext}(\mathbf{r})}{\partial \mathbf{R}_I \partial \mathbf{R}_J} d\mathbf{r} + \frac{\partial^2 E_N(\mathbf{R})}{\partial \mathbf{R}_I \partial \mathbf{R}_J} \end{aligned} \tag{2.38}$$

The calculation of the Hessian of $E(\mathbf{R})$ in the equation (2.38) requires the electron density, $n(\mathbf{r})$, and its linear response to a distortion of the geometry, $\frac{\partial n(\mathbf{r})}{\partial \mathbf{R}_I}$, which can be determined using the density functional perturbation theory (DFPT) [64, 65], or the small displacement method[66].

2.4 Equation of state

2.4.1 Generalities of equation of state

The thermodynamic state of a system is usually defined by pressure P, temperature T, and specific volume V (or specific mass ρ), and linked by some mathematical relationship called equation of state (EOS). For example, the well-known equation of state for ideal gases would be expressed in $PV = nRT$, where n the amount of gas in molar and R is the gas constant.

For solid, the simplest isothermal EOS can be derived from the definition of the bulk modulus K,

$$K = -\frac{dP}{d\ln V} = \frac{dP}{d\ln \rho}. \tag{2.39}$$

If the bulk modulus K is not changing with some certain pressure range, for example, $K = K_0$, then the EOS can be derived by integrating the equation (2.39) with the assumption $K = K_0$:

$$V = V_0 \exp\left(-\frac{P}{K_0}\right). \tag{2.40}$$

However, this assumption only works in a limited pressure range since the solid is more difficult to compress at high pressure, or bulk modulus is significantly large at high pressure; thus the K is not constant. There are many different EOS can be adopted, such as the Murnaghan's, Birch–Murnaghan EOS, and the Vinet EOS to study the EOS of minerals in the high pressure, such as at the mantle conditions. In this study, the Birch–Murnaghan equation of state has been used.

2.4.2 Eulerian finite strain Birch–Murnaghan equation of state

As one of the most widely used equation of state , Eulerian finite strain Birch–Murnaghan equation of state (or just called the Birch–Murnaghan equation of state) The Birch–Murnaghan equation of state can be obtained in the linear elastic regime, here the brief derivation of Birch–Murnaghan equation of state is introduced.

Eulerian finite strain

In the Eulerian scheme, the coordinates x_i of a point in the initial unstrained state expressed as a function of its coordinates X_i in the strained state and the strain u_i:

$$x_i = X_i - u_i. \tag{2.41}$$

We determine the distance between two neighboring points P (coordinates: x_i with i = 1, 2, 3)) and Q (coordinates: $x_i + dx_i$) by:

$$ds^2 = \sum_i (dx_i)^2, \tag{2.42}$$

then, the distance changes after applying the strains by:

$$dS^2 - ds^2 = \sum_i (dX_i)^2 - \sum_i (dx_i)^2 = 2\sum_i dX_i du_i - \sum_i (du_i)^2. \tag{2.43}$$

Assuming the strains **u** are continuous and differentiable in terms of x_i, such as:

$$du_i = \sum_k \frac{du_i}{dX_k} dX_k, \tag{2.44}$$

then the Eulerian finite strain tensor ε_{ij} is defined by:

$$dS^2 - ds^2 = 2\sum_{ij} \varepsilon_{ij} dX_i dX_j, \tag{2.45}$$

with:

$$\varepsilon_{ij} = \frac{1}{2}\left(\frac{\partial u_i}{\partial X_j} + \frac{\partial u_j}{\partial X_i}\right) - \frac{1}{2}\sum_k \frac{\partial u_k}{\partial X_i}\frac{\partial u_k}{\partial X_j} = \frac{1}{2}\left(\delta_{ij} - \frac{1}{2}\sum_k \frac{\partial u_k}{\partial X_i}\frac{\partial u_k}{\partial X_j}\right) \tag{2.46}$$

For the isotropic compressional strain caused by the application of hydrostatic pressure,

$$\frac{\partial u_1}{\partial X_1} = \frac{\partial u_2}{\partial X_2} = \frac{\partial u_3}{\partial X_3} = \frac{\theta}{3}, \tag{2.47}$$

and

$$\theta = \sum_i \frac{\partial u_i}{\partial X_i} = \frac{\Delta V}{V_0}. \tag{2.48}$$

From the equation (2.46) and the equation (2.47) we have

$$\varepsilon_{ij} = \varepsilon \delta_{ij}, \tag{2.49}$$

with

$$\varepsilon = \frac{\theta}{3} - \frac{1}{2}\left(\frac{\theta}{3}\right)^2. \tag{2.50}$$

According to the definition of Eulerian finite strain, the volume of an elementary cube is $V = (dX_1)^3$ in the strained state, and the volume of the unstrained state can be written as

$$V_0 = \left[dX_1\left(1 - \frac{\partial u_1}{\partial X_1}\right)\right]^3, \tag{2.51}$$

and substitute equation (2.47) back to this equation, then

$$V_0 = \left[dX_1\left(1 - \frac{\theta}{3}\right)\right]^3, \tag{2.52}$$

thus the volume ratio of the unstrained and strained system can be expressed by:

$$\frac{V_0}{V} = \left(1 - \frac{\theta}{3}\right)^3. \tag{2.53}$$

Substituting equation (2.50) into equation (2.53) to get the volume ratio unstrained to strained systems:

$$\frac{V_0}{V} = (1 - 2\varepsilon)^{3/2}\,. \tag{2.54}$$

As the ε is negative for positive pressures, here the "compression" $f = -\varepsilon$ [67] is introduced, and equation (2.54) changes to

$$\frac{V_0}{V} = (1 + 2f)^{3/2}. \tag{2.55}$$

Relationship between the Helmholtz free energy and the f

The isothermal bulk modulus at $P = 0$ is:

$$K_{0,T} = -\lim_{P\to 0}\left(\frac{PV}{\Delta V}\right)_T. \tag{2.56}$$

Since $P = -\left(\frac{\partial F}{\partial V}\right)_T$, and substitute equation (2.48) into equation (2.56), it changes to

$$K_{0,T} = \lim_{P\to 0}\left(\frac{1}{\theta}\frac{\partial F}{\partial V}\right)_T. \tag{2.57}$$

To simplify equation (2.55) by expand the equation to the first order:

$$\frac{V}{V_0} = (1 + 2f)^{-3/2} \approx 1 - 3f, \tag{2.58}$$

and thus:

$$dV \approx -3V_0 df. \tag{2.59}$$

Substituting equation (2.59), equation (2.50) back to equation (2.57), it turns to:

$$K_{0,T} \approx \lim_{P\to 0}\left(\frac{1}{3f}\frac{\partial F}{3V_0\partial f}\right)_T \tag{2.60}$$

or

$$9K_{0,T}V_0 \approx \lim_{P\to 0}\left(\frac{1}{f}\frac{\partial F}{\partial f}\right)_T \tag{2.61}$$

In the framework of the Birch–Murnaghan EOS, the Helmholtz free energy of the

solid in terms of the "compression" f [67] is expressed as

$$F(T) = a(T)f^2 + b(T)f^3 + c(T)f^4 + \cdots . \tag{2.62}$$

The second order Birch–Murnaghan equation of state can be derived by expanding the Helmholtz free energy is to the second order only, for example, $F(T) = a(T)f^2$, then the $a(T)$ be derived by substituting this Helmholtz free energy to equation (2.61).

$$a(T) = \frac{9}{2} K_{0,T} V_0, \tag{2.63}$$

and the compression f in terms of the volume ratio is:

$$f = \frac{1}{2}\left[\left(\frac{V_0}{V}\right)^{2/3} - 1\right], \tag{2.64}$$

then the pressure can be derived by:

$$P(T) = \frac{3K_{0,T}}{2}\left[\left(\frac{V_0}{V}\right)^{7/3} - \left(\frac{V_0}{V}\right)^{5/3}\right]. \tag{2.65}$$

Similarly, the third order Birch–Murnaghan equation of state can be derived by expanding the Helmholtz free energy to the third order, namely, $F(T) = a(T)f^2 + b(T)f^3$. After a similar derivation to that of the second order Birch–Murnaghan equation of state is given by:

$$P = \frac{3K_{0,T}}{2}\left[\left(\frac{V_0}{V}\right)^{7/3} - \left(\frac{V_0}{V}\right)^{5/3}\right]\left\{1 + \frac{3}{4}(K'_{0,T} - 4)\left[\left(\frac{V_0}{V}\right)^{2/3} - 1\right]\right\}. \tag{2.66}$$

where, $K'_{0,T}$ is the derivative of the bulk modulus with respect to pressure.

In practice, the relationship of Helmholtz free energy and f can be fitted by equation (2.62), or by 2.66, and obtaining the Helmholtz free energy on a denser volume grid, then all other thermodynamic properties can be derived numerically, a Python program, `qha`, has been coded to perform these fittings and calculations automatically, see chapter 3 for details.

2.5 Thermodynamic properties within quasiharmonic approximation (QHA)

The QHA is a phonon-based model to calculate volume-dependent thermodynamic properties. It is developed from the harmonic approximation (HA). In HA, the vibrational frequencies are independent of inter-atomic distance, which could lead to nonphysical results, such as the thermal expansion is always zero. While in QHA, the vibrational frequencies are assumed volume dependent. Thermodynamic properties of solids are well described within the QHA conjugated with the LDA and pseudopotentials below melting temperatures. The details of this topic have been addressed in chapter 3.

2.6 Equilibrium stable isotope fractionation

In general, the chemical behavior of an element is determined by the electronic structure, and the nucleus plays an insignificant role in chemical interactions. However, from the quantum mechanics perspective, the mass of an atom affects the vibrational energy and therefore the strength of the chemical bonds. Moreover, because of the difference of the isotopes of an element, the strength of chemical bonds varies a bit, and eventually can lead to the different partition of isotopes among different phases, this process called isotope fractionated among phases.

In this section, some definitions of isotope fractionation are briefly introduced, followed by the theoretical backgrounds on how to calculate the equilibrium stable isotope factor.

2.6.1 The fractionation factor α and δ notation

The fractionation factor is defined as the ratio of two isotopes in one phase A divided by the corresponding ratio for another phase B:

$$\alpha_{A-B} = \frac{R_A}{R_B} \tag{2.67}$$

where, R_A or R_B are the isotope ratio in phase A and B, respectively. For example, for iron isotopes (^{54}Fe and ^{56}Fe), the fractionation factor between two phase are given by:

$(^{56}\mathrm{Fe}/^{54}\mathrm{Fe})_A/(^{56}\mathrm{Fe}/^{54}\mathrm{Fe})_B$.

In practical, it is more often to use the δ notation to represent the isotope composition of some phase, which is defined in below:

$$\delta_{sample} = \left(\frac{R_{sample}}{R_{standard}} - 1 \right) \times 1000(‰) \tag{2.68}$$

where the $R_{standard}$ is the isotope ratio of the standard phase, for iron isotopes, the standard phase is called IRMM-014, which is distributed by the Institute for Reference Materials and Measurements [68].

For two phases A and B, the δ values and the fractionation factor α are related by:

$$\delta_A - \delta_B = \Delta_{A-B} \approx 10^3 \ln \alpha_{A-B} \tag{2.69}$$

For the calculation purpose, a β factor is also introduced. If phase B is a fictitious perfect gas of element X, the isotope fractionation factor is then defined as the reduced partition function ratio, or beta factor β [69]. In this case, the fractionation factor between two phases is given by:

$$\alpha_{A-B} = \beta_A/\beta_B, \tag{2.70}$$

Then, $10^3 \ln \alpha_{A-B} = 10^3 \ln \beta_A - 10^3 \ln \beta_B$.

2.6.2 $10^3 \ln \beta$ calculations

According to the Urey model[70] or Bigeleisen-Mayer equation[71] on isotope fractionation, the reduced partition function ratio, or the β facor is given by:

$$\beta = \prod_i^{3N-3} \frac{\mu_{ih}}{\mu_{il}} \frac{\exp(-\frac{1}{2}\mu_{ih})}{1-\exp(-\mu_{ih})} \frac{1-\exp(-\mu_{il})}{\exp(-\frac{1}{2}\mu_{il})} \tag{2.71}$$

where $\mu_{il,h} = \hbar\omega_{ih,l}/k_B T$, h and l refer to the heavy and light isotope, respectively. T is the temperature in Kevin, $\hbar$ is the Boltzmann's constant, and ω_i is the vibrational frequency of the i^{th} mode. This product runs over all 3N-3 phonon modes, N is the number of atoms in the cell. Please refer to the references for a full derivation of this

reduced partition function ratio [70, 71, 69, 72, 73, 74].

One interesting fact of the $10^3\beta$ is IT proportional to $1/T^2$ at high-temperature range. For the i^{th} vibrational mode β_i can be expressed as:

$$\beta_i = \frac{\mu_h}{\mu_l}\frac{\exp(-\frac{1}{2}\mu_h)}{1-\exp(-\mu_h)}\frac{1-\exp(-\mu_l)}{\exp(-\frac{1}{2}\mu_l)} \tag{2.72}$$

At high temperature range, the μ would be very small, and the $\exp(-\mu)$ can be expand in the Taylor series $1-\mu+\frac{\mu^2}{2!}-\frac{\mu^3}{3!}+\cdots$, then equation (2.72) can be rewrite to

$$\begin{aligned}\beta_i &= \frac{\mu_h}{\mu_l}\frac{\exp(-\frac{1}{2}\mu_h)}{\exp(-\frac{1}{2}\mu_l)}\frac{1-\exp(-\mu_l)}{1-\exp(-\mu_h)} \\ &= \frac{\exp(-\frac{1}{2}\mu_h)}{\exp(-\frac{1}{2}\mu_l)}\frac{1-\frac{\mu_i}{2}+\frac{\mu_i^2}{6}}{1-\frac{\mu_h}{2}+\frac{\mu_h^2}{6}}.\end{aligned} \tag{2.73}$$

Then the $10^3\ln\beta_i$ can be calculated approximately by:

$$\begin{aligned}\ln\beta_i &= \frac{1}{2}(u_i-u_h)+\ln(1-\frac{\mu_i}{2}+\frac{\mu_i^2}{6})-\ln(1-\frac{\mu_h}{2}+\frac{\mu_h^2}{6}) \\ &\approx \frac{u_l^2-u_h^2}{6} \\ &= \frac{\hbar^2(\omega_l^2-\omega_h^2)}{6k_B^2T^2} \\ &\propto \frac{1}{T^2}\end{aligned} \tag{2.74}$$

Thus, the calculated $\ln\beta$ factor should be approximately proportional to $1/T^2$ at a high-temperature range, but this property does not hold at a low-temperature range. Actually, at a low-temperature range, the $\ln\beta$ factor is approximately proportional to $1/T$. Therefore, if plot the $10^3\ln\beta$ versus $1/T^2$ for a large temperature range, the relationship is not linear, but slightly curved.

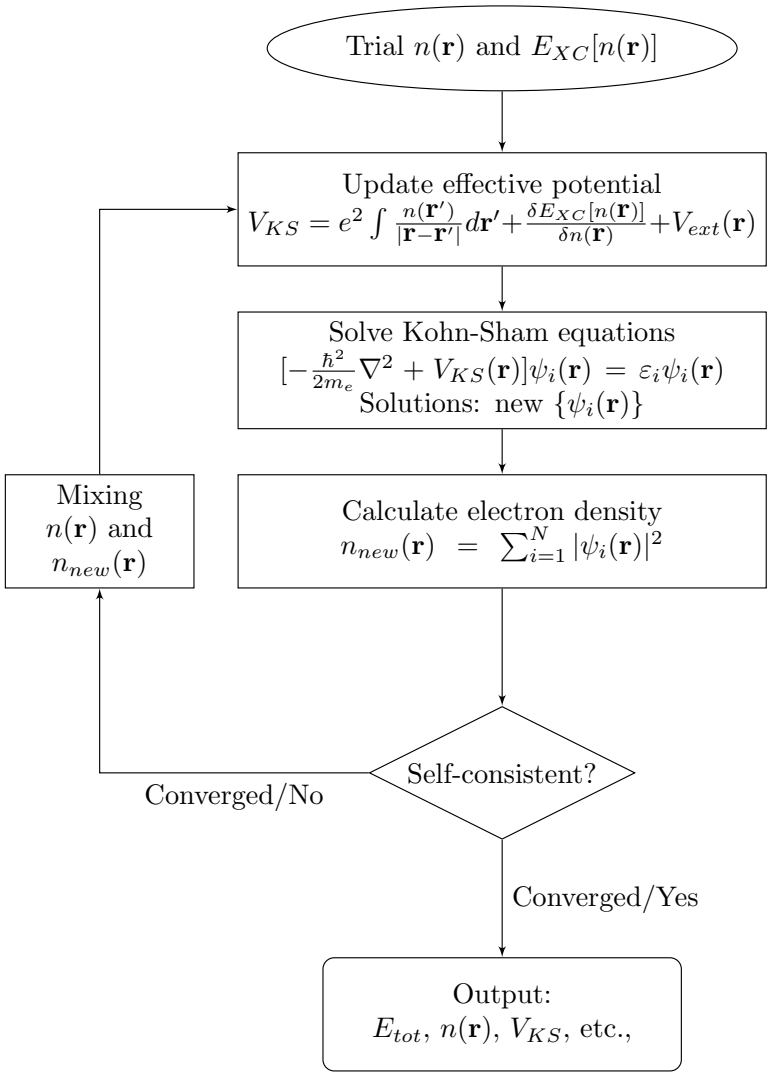

Figure 2.1: Flow chart of the self-consistency loop for solving Kohn-Sham equations.

Chapter 3

`qha`: A Python package to calculate thermodynamical properties for multi-configuration systems

In this work, we present a Python package, `qha`, which can calculate the equation of state and various thermodynamic properties of both single- and multi-configuration crystalline materials within a user-specified pressure and temperature range in the framework of the quasi-harmonic approximation (QHA). Two examples, one for single-configuration calculation and the other for multi-configuration calculation, are also distributed along with source code. Apart from its versatility, `qha` has been tested to be both accurate and computationally efficient.

3.1 Introduction

Investigation of materials properties at extreme conditions of pressure (P) and temperature (T) can be quite challenging to experiments, depending on the property and conditions. In general, predictive computational studies of materials properties can complement experimental approaches or provide information challenging to experiments. Among the numerous statistical mechanics approaches used to investigate thermodynamics properties computationally, the quasiharmonic approximation (QHA) proved to

be exceedingly useful as long as T is not "too close" to the melting temperature, T_M. The combination of *ab-initio* vibrational spectra based on density functional theory (DFT) with the QHA helped to clarify the power of such approach and approximately the range of T in which it can be realistically applied. Mineral physics studies have played an important role in this exploration of the QHA's performance because there is a considerable amount of detailed measurements to compare with computationally predicted thermal equations of state and thermodynamic properties ([75]; [76]). In general, the QHA works very well in conjunction with the local density approximation (LDA) and pseudopotentials up to $\sim 0.7\,T_M$ for strongly bonded materials such as oxides and silicates ([76]; [77]). One can verify this pressure dependent range of validity of the QHA by comparing predictions of the most sensitive property to anharmonic effects, the thermal expansivity, with measurements. Careful use of the QHA is also helping us to assess more precisely the performance of various exchange-correlation functionals ([78]; [79]; [80]; [81]).

The QHA approach evolved from the harmonic approximation (HA), where the dependence of the energy on atomic displacements is treated quadratically. The small vibrational amplitude compared to the interatomic distances at low T justifies this approximation. One limitation of the HA is that vibrational frequencies do not depend on crystal volumes, which leads to unphysical conclusions such as no thermal expansion or infinite thermal conductivity ([82]). The QHA overcomes this problem and most limitations of the HA by allowing the interatomic force constants and vibrational frequencies to be volume dependent ([82]; [83]; [84]). Today, research on the limits of validity of the QHA, or the importance of anharmonic effects, and the performance of exchange-correlation functionals for structural and vibrational properties are interweaved ([78]; [79]; [81]). Therefore, it is extremely important to perform such calculations with care to assess the origin of discrepancies between predictions and measurements.

There are several published ([65]; [85]; [86]; [87]) and unpublished([75]; [88]; [89]; [90]; [91]) implementations of the QHA to calculate thermodynamics and thermoelastic properties of materials. So far, all published codes address the free energy and the thermodynamic properties of single configuration systems. Here we present a code to compute these properties for phases consisting of multiple configurations, e.g., disordered solid solutions, H-disordered phases such as ice-Ih, and multi-configuration defects. The

formalism behind the code presented here has been successfully used to compute: 1) the order-disorder phase boundary between ice-VIII and ice-VII, the high-density phases of H_2O-ice ([91]); 2) the relative stability of hydrous defects $(4\,H)^x_{Si}$ and $(2\,H)^x_{Mg}$ in Mg_2SiO_4-forsterite at high P and T ([92]); 3) the effect of disorder and iron concentration on the spin crossover diagram of Fe^{3+}-bearing $MgSiO_3$-bridgmanite ([93]). The multi-configuration approach enables these types of problems to be addressed more realistically, with the limitation being the number of configurations included.

Apart from their restrictions on one configuration, some of the existing published implementations of the QHA are either hard-coded within another *ab-initio* software ([86]) or prepared for a particular operating system ([85]; [87]), which makes them not easy to fit in other users' code without a deep understanding of their implementation. Therefore, we created this independent Python package to calculate the thermodynamic properties of materials with either single or multiple configurations. The necessary inputs are the volume dependent *ab-initio* static energies and phonon frequencies for each configuration, as well as the user specified P- and T-range of the calculation. Phonon frequencies can be calculated by density functional perturbation theory (e.g., [64]) or finite displacement methods (e.g., [66]; [87]) using several available *ab-initio* software, such as QUANTUM ESPRESSO ([94], [95]), VASP ([96]), ABINIT ([97]), etc.

The paper outline is as follows. The next section presents detailed fundamental equations on which the code is based. Section 3.3 shows the structure of this code. In section 3.4, we show the structure of input files for the program, followed by the description of output files. Our conclusions are presented in section 3.6.

3.2 Methods used in the program `qha`

3.2.1 Partition function and Helmholtz free energy of a one-configuration system

The partition function of a system with only one configuration can be written as

$$Z_{\mathrm{QHA}}(T,V) = \exp\left(-\frac{E(V)}{k_B T}\right) \cdot \prod_{q=1,m=1}^{N_q,N_m} \frac{\exp\left(-\frac{\hbar\omega_{q,m}(V)}{2k_B T}\right)}{1-\exp\left(-\frac{\hbar\omega_{q,m}(V)}{k_B T}\right)}, \tag{3.1}$$

where $Z_{\mathrm{QHA}}(T,V)$ is the partition function in the QHA of the system whose volume is V, N_q and N_m are the number of q-points sampled in the Brillouin zone and the number of modes per q-point, and $\omega_{q,m}$ denotes the frequencies of the qth q-point and mth mode of that point. $\hbar$ and k_B are Planck constant and Boltzmann constant, respectively. T is the temperature in Kelvin. Then the Helmholtz free energy can be derived from $Z_{\mathrm{QHA}}(T,V)$

$$\begin{aligned} F_{\mathrm{QHA}}(T,V) &= -k_B T \ln Z_{\mathrm{QHA}}(T,V) \\ &= E(V) + \sum_{q=1,m=1}^{N_q,N_m} \left\{ \frac{\hbar\omega_{q,m}(V)}{2} + k_B T \ln\left[1 - \exp\left(-\frac{\hbar\omega_{q,m}(V)}{k_B T}\right)\right]\right\}, \end{aligned} \tag{3.2}$$

with $E(V)$ being the static energy, i.e., the energy for the lattice with clamped ions, and the second term being the vibrational energy contributed by the phonons.

3.2.2 Partition function and Helmholtz free energy of a multi-configuration system

Suppose a system consists of N_{conf} configurations, which are grouped into N_c symmetrically-distinct configurations with the degeneracies $\{g_n\}$ (n is the index of each symmetrically-distinct configuration), that is, $\sum_{n=1}^{N_c} g_n = N_{\mathrm{conf}}$. For such a multi-configuration system, the partition function is

$$Z_{\mathrm{QHA}}(T,V) = \sum_{n=1}^{N_c} g_n \left\{ \exp\left(-\frac{E_n(V)}{k_B T}\right) \cdot \prod_{q=1,m=1}^{N_q,N_m} \left[\frac{\exp\left(-\frac{\hbar\omega^n_{q,m}(V)}{2k_B T}\right)}{1-\exp\left(-\frac{\hbar\omega^n_{q,m}(V)}{k_B T}\right)}\right]^{w_q^n}\right\}, \tag{3.3}$$

where E_n and w_q^n are the static energy of nth configuration and its qth q-point weight. Then the Helmholtz free energy can be obtained accordingly as

$$\begin{aligned} F_{\mathrm{QHA}}(T,V) = -k_B T \cdot \\ \ln\left\{ \sum_{n=1}^{N_c} g_n \exp\left(-\frac{E_n(V)}{k_B T}\right) \cdot \prod_{q=1,m=1}^{N_q,N_m} \left[\frac{\exp\left(-\frac{\hbar\omega^n_{q,m}(V)}{2k_B T}\right)}{1-\exp\left(-\frac{\hbar\omega^n_{q,m}(V)}{k_B T}\right)}\right]^{w_q^n}\right\}. \end{aligned} \tag{3.4}$$

To calculate the vibrational spectra for all configurations are frequently computationally demanding. If the vibrational spectra of all configurations are expected to be

very similar to each other, it might be possible to use a single spectrum of only one representative configuration for all configurations, as the expense of accuracy, in order to reduce computational cost.

In this case, $F(T,V)$ can be simplified as

$$F_{\mathrm{QHA}}(T,V) = -k_B T \ln\left[\sum_{n=1}^{N_c} g_n \exp\left(-\frac{E_n(V)}{k_B T}\right)\right] + \sum_{q=1,m=1}^{N_q,N_m} w_q \left\{\frac{\hbar\omega_{q,m}(V)}{2} + k_B T \ln\left(1-\exp\left(-\frac{\hbar\omega_{q,m}(V)}{k_B T}\right)\right)\right\}, \quad (3.5)$$

where the first term is the static contribution (F_{static}), and the second term is the vibrational contribution ($F_{\mathrm{vibrational}}$).

3.2.3 Alignment of volumes

According to equation (3.3)-equation (3.5), the phonon frequencies are required at the same volume for all configurations. However, calculations not always guarantee this result. Usually structural optimizations are performed at several target pressures ([98]; [99]) for all configurations. This procedure leads to slightly different volumes optimized at each pressure for each configuration. Therefore we only can calculate phonon frequencies at volumes which are not exactly equal to each other among the configurations. To circumvent this issue, single-configuration calculations are first performed for each configuration to obtain a series of free energies, $F_n(T,V)$, according to equation (3.2). Then $F_n(T,V)$'s are fit by a finite strain equation of state (see next section) at each T for all configurations on a regular and unique volume mesh, $\{V_i\}$ (where $i = 1,\ldots,N_V$, with N_V to be the number of volumes mesh points), to give $F_n(T,V_i)$, from which the partition functions for all configurations are

$$Z_n(T,V_i) = \exp\left(-\frac{F_n(T,V_i)}{k_B T}\right). \quad (3.6)$$

Then, the multi-configuration partition function is:

$$Z(T,V_i) = \sum_{n=1}^{N_c} g_n Z_n(T,V_i), \quad (3.7)$$

from which the total free energy is obtained in the single and regular volume mesh

$$F(T, V_i) = -k_B T \ln Z(T, V_i). \tag{3.8}$$

3.2.4 The equation of state fitting

Considering the input volumes may be sparse for thermal properties derivation, a third order finite strain Birch–Murnaghan equation of state fitting ([**?**]), whose order can be controlled by users (third to fifth order of Eulerian strain), is adopted to obtain free energies on the denser and regular volume mesh ($\{V_i\}$ mentioned above). The denser volume mesh is determined automatically based on the user-defined T- and P-range. As the internal pressure for a fixed volume usually increases with increasing T, which could lead to the lack of data at the low-P-high-T regimes, the volume mesh is expanded slightly to overcome this issue. After obtaining the Helmholtz free energy on this finer volume mesh, all other thermodynamic properties can be calculated numerically according to table 3.1.

Table 3.1: Equations used to calculate thermodynamic properties.

Property name	Equation used
Pressure P	$P = -\left(\frac{\partial F}{\partial V}\right)_T$
Entropy S	$S = -\left(\frac{\partial F}{\partial T}\right)_V$
Internal energy U	$U = F + TS$
Enthalpy H	$H = U + PV$
Gibbs free energy G	$G = F + PV$
Thermal expansion coefficient α	$\alpha = \frac{1}{V}\left(\frac{\partial V}{\partial T}\right)_P$
Thermodynamic Grüneisen parameter γ	$\gamma = \frac{B_T \alpha V}{C_V}$
Isothermal bulk modulus B_T	$B_T = -V\left(\frac{\partial P}{\partial V}\right)_T$
Adiabatic bulk modulus B_S	$B_S = B_T(1 + \gamma\alpha T)$
Volumetric heat capacity C_V	$C_V = \left(\frac{\partial U}{\partial T}\right)_V$
Isobaric heat capacity C_P	$C_P = C_V(1 + \gamma\alpha T)$

3.3 The qha distribution

3.3.1 Flowchart/calculation procedure of the qha

qha is written in Python 3, and the main calculation routine is done in run.py, the sequence of steps is adopted is shown in figure 3.1 and described briefly below:

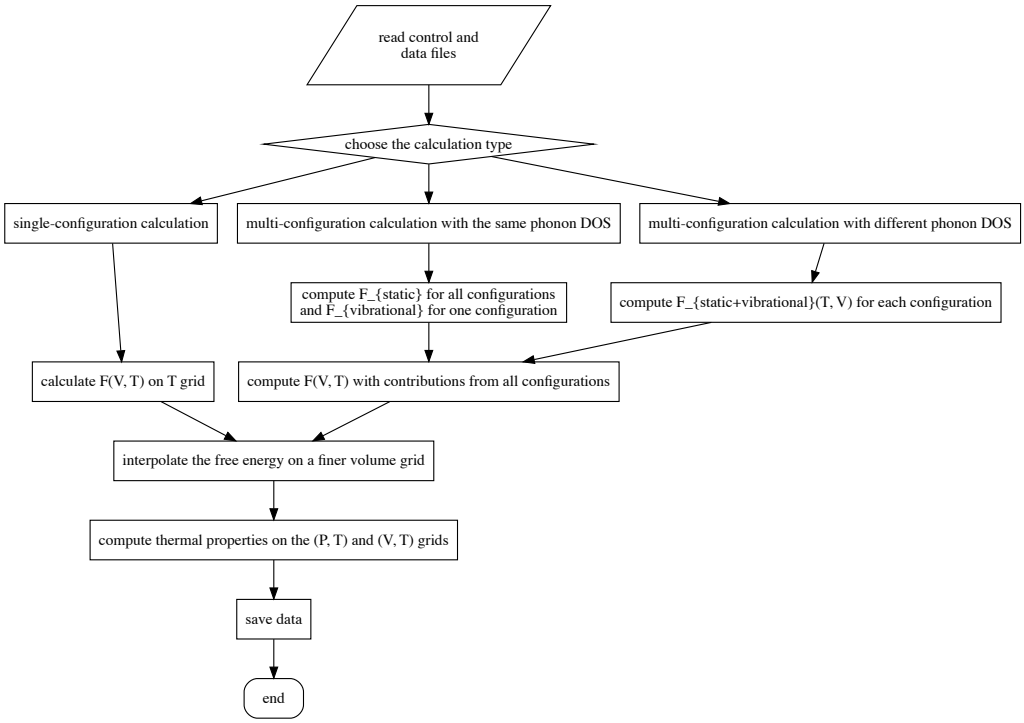

Figure 3.1: Flow chart of the calculation process in the qha main script.

1. Read the data and calculation settings files, check section 3.4 below for details of the organization and preparation of these files.

2. Determine the calculation type based on the input.

   (a) If it is a single-configuration calculation, the Helmholtz free energy is calculated based on equation (3.2).

(b) If it is a multi-configuration calculation, the Helmholtz free energy is calculated as in equation (3.4) or equation (3.8) depending on the choice of vibrational spectrum.

3. Fit the free energy to a finite-strain equation of state on a dense and unique volume mesh.

4. Calculate the thermodynamic properties on the dense (T, V) and (T, P) grids numerically.

5. Save all the calculated properties to text files using user-specified temperatures and pressures, and plot results if desired.

A description of the modules used by `run.py` is summarized in table 3.2.

3.3.2 Documentation and examples

The documentation is distributed with `qha` source code and generated by Sphinx (`http://www.sphinx-doc.org`). Two examples are given in the examples directory to display the full features of the `qha` package. The ice VII and silicon examples demonstrate calculations of thermodynamic properties for multi-configuration and single-configuration systems, respectively, with input data, computational settings, and visualized results provided.

3.3.3 Installation

We recommend using the Python `pip` (`https://pypi.org/project/pip/`) package manager to install the package.

For installation from the source code, change the working directory to the `qha` top-level directory and run command `pip install /path/to/top/level/directory` to install the package.

3.4 Input and output files

3.4.1 Description of input files

The `qha` code has two types of input files: the data file and the calculation control file. The data file, which will be referred to as `input` or `inputN` below, contains data for QHA calculation extracted from the *ab-initio* calculation software output. The control file, by default with name `settings.yaml`, specifies the computational settings. All allowed settings are listed in table 3.3 in detail. We have three types of calculations: single-configuration, multiple configurations but sharing the same phonon density of states, and multiple configurations with different phonon density of states. The type can be specified inside the settings file.

Table 3.3: Parameters in the `settings.yaml` file in YAML syntax

Parameter name (Keys)	Values (with a default value if apply)
`calculation`	The type of calculation a user wants to perform. Allowed values are `single`, `same phonon dos` and `different phonon dos`.
`NT`	Number of temperatures on the grid
`DT`	The interval between two nearest temperatures on the grid
`NTV`	Number of volumes (or equivalently, pressures) on the gird
`DELTA_P`	The interval between two pressures on the grid, the default value is 0.1 GPa
`DELTA_P_SAMPLE`	Pressure-sampling interval, used for output, the default value is 1 GPa
`T_MIN`	Desired minimum temperature to calculate, in Kelvin, the default value is 0 K.
`P_MIN`	Desired minimum pressure to calculate, in GPa

Continued on next page

Table 3.3: continued from previous page

Parameter name (Keys)	Values (with a default value if apply)
`input`	Name(s) of the input file(s). • In a single-configuration calculation, only the path of the file is needed, • In a multi-configuration calculation, the names of the inputs files and the corresponding configurational degeneracies are given in a YAML dictionary.
`static_only`	Whether to include only the static energy in the calculation. Allowed values are `True` (do not include) or `False` (include, default).
`order`	Order of Birch–Murnaghan equation-of-state fitting, `3` (default), `4` or `5`
`energy_unit`	Energy unit in the output file, either `ry` (default) or `ev`
`thermodynamic_properties`	Determines which thermodynamic properties will be calculated. Allowed values are: • `F`, the Helmholtz free energy F • `G`, the Gibbs free energy G • `U`, the internal energy U • `H`, the enthalpy H • `V`, the volume V • `Cp`, the isobaric heat capacity C_P • `Cv`, the volumetric heat capacity C_V • `Bt`, the isothermal bulk modulus B_T • `Btp`, the derivative of the isothermal bulk modulus with respect to pressure B'_T • `Bs`, the adiabatic bulk modulus B_s • `alpha`, the thermal expansion coefficient α

Continued on next page

Table 3.3: continued from previous page

Parameter name (Keys)	Values (with a default value if apply)
	• `gamma`, the thermal Grüneisen parameters γ
`target`	The default value is `parallel`. This is a Numba package option. Allowed options are `cpu` (used on single-threaded CPU), `parallel` (used on multi-core CPU), `cuda` (used on CUDA GPU).
`results_folder`	The path to store all calculated values, the default value is `./results`, which is a directory named `results` in the same folder as the `input` file.
`T4FV`	Temperature for $F(T_i, V)$ plotting. By default is `['0', '300']`.
`high_verbosity`	Two verbosity levels are implemented, `True` or `False` (default).

The structure of the input file for a single-configuration system is shown in table 3.4 (see the input file of silicon in the `examples` directory for a reference). For a system with multiple configurations, the input file for each configuration is organized in the same way as that of the single configuration. The degeneracy of each configuration is specified after the name of the corresponding input file in the settings file (`settings.yaml`).

Table 3.4: Structure of the input file and brief descriptions

Structure of the input data	Notes
# Comment line	First 3 lines are comments, plus the description of the calculation, but can also be empty.
# Additional comment line	
	Continued on next page

Table 3.4: continued from previous page

Structure of the input data	Notes
# Number of volumes, q-vectors, normal mode, formula units	
nv nq np nm	number of calculated volumes, q-vectors, normal mode, formula units
	An empty line, not required.
P= P_1 V= V_1 E= E_1	P_1, V_1, and E_1 are pressure (in arbitrary unit), volume (in ${a_0}^3$) and energy (in Rydberg) of the first volume calculation
$q_1(x)$ $q_1(y)$ $q_1(z)$	first q-point from first volume
$\omega_{1,1}$	Vibrational frequencies (in cm^{-1}) obtained from *ab-initio* calculation, the total number of vibrational modes is three times the number of atoms in the system.
$\omega_{1,2}$ $\vdots$ $\omega_{1,3N}$	
$q_2(x)$ $q_2(y)$ $q_2(z)$	All the data from the rest q-points are organized as the same way as showed for the first q-point.
$\omega_{2,1}$ $\omega_{2,2}$ $\vdots$ $\omega_{2,3N}$ $\vdots$ $q_{N_q}(x)$ $q_{N_q}(y)$ $q_{N_q}(z)$ $\omega_{N_q,1}$	

Continued on next page

Table 3.4: continued from previous page

Structure of the input data	Notes
$\omega_{N_q,2}$ $\vdots$ $\omega_{N_q,3N}$	
	An empty line, but not required.
P= P_2 V= V_2 E= E_2	All data from other volumes are structured in the same way as the first volume shown above
$\vdots$	
	An empty line, not required.
`weights`	The weights of different q-points below; this line must contain keyword `weight` or `weights`.
$q_1(x)$ $q_1(y)$ $q_1(z)$ w_{q_1}	q-point's coordinates followed by its weight in the Brillouin zone, there are `nq` lines in total for this part.
$\vdots$ $q_{N_q}(x)$ $q_{N_q}(y)$ $q_{N_q}(z)$ w_{N_q}	

For a system with multiple configurations where all configurations have the same vibrational spectrum, the input files are prepared in the same way mentioned above, and the calculation can be done using equation (3.4) as shown in the ice VII example. The calculation can also be performed as indicated in equation (3.5) with all configurations having the same vibrational spectrum for computational efficiency. In this case, the keyword `same_phonon_dos` should be set to `true` in the settings file (check table 3.3 for details). All parameters of the computational settings are listed in the control file (`settings.yaml`) using YAML syntax (see the syntax of YAML on website `http://yaml.org/`). Users can also refer to the latest documentation hosted on GitHub (`https://mineralscloud.github.io/qha/tutorials/run.html#how-to-make-settings`).

For calculations performed with the QUANTUM ESPRESSO, we implemented a small helper script to generate the input file for the `qha` code from its output. Please refer to the `examples/silicon/make_input` directory as an example.

3.4.2 Output files and analysis

The Helmholtz free energy (F), enthalpy (H), internal energy (U), Gibbs free energy (G), thermal expansion coefficient (α), Grüneisen parameter (γ), and specific heat (C_p and C_v) can be calculated and saved to the corresponding text files as functions of T and P or V (see table 3.5 for the most important list of output files). See code documentation for more details.

For each physical property, the output file name follows a specific format as `abbreviation_tp/tv_unit`. The `abreviation` corresponds to the settings of the `thermodynamic_properties` key in table 3.3; `tp/tv` indicates the data is organized as a function of T and P or V; `unit` means the unit of the properties, which can be `ry` (Rydberg) , `ev` (electron-volt) , `ang3` (Å^3), and `bohr3` ($a_0{}^3$). Users can specify the pressure intervals being saved in the results file by setting the `DELTA_P_SAMPLE` value, which is 1 GPa by default. Please see table 3.3 for details.

3.5 Test case

The method implemented in this code has been successfully used to study of the ice-VIII to –VII, an ordered-disordered phase boundary ([91]). The main remaining discrepancy between the measured and computed phase boundary seemed to be related to the supercell size. In that study, 16 molecule supercells consisting of 2 interpenetrating ice-Ic lattices are built for both phases. The ice VII supercell has 8100 configurations in total, but can be reduced to 52 symmetrically distinct configurations.

The calculation used Perdew—Burke—Ernzerhof functional for the exchange-correlation ([54]) and norm-conserving pseudopotentials ([100]). A plane-wave basis set with a cutoff energy of 100 Ry and a $2 \times 2 \times 2$ k-point mesh were adopted for all supercells. Each of the 52 supercell structures are optimized at several pressures ([98]; [99]) before performing phonon calculations for the zone-center phonon mode. The post-processed outputs of the QUANTUM ESPRESSO are given as input for `qha`, and two of

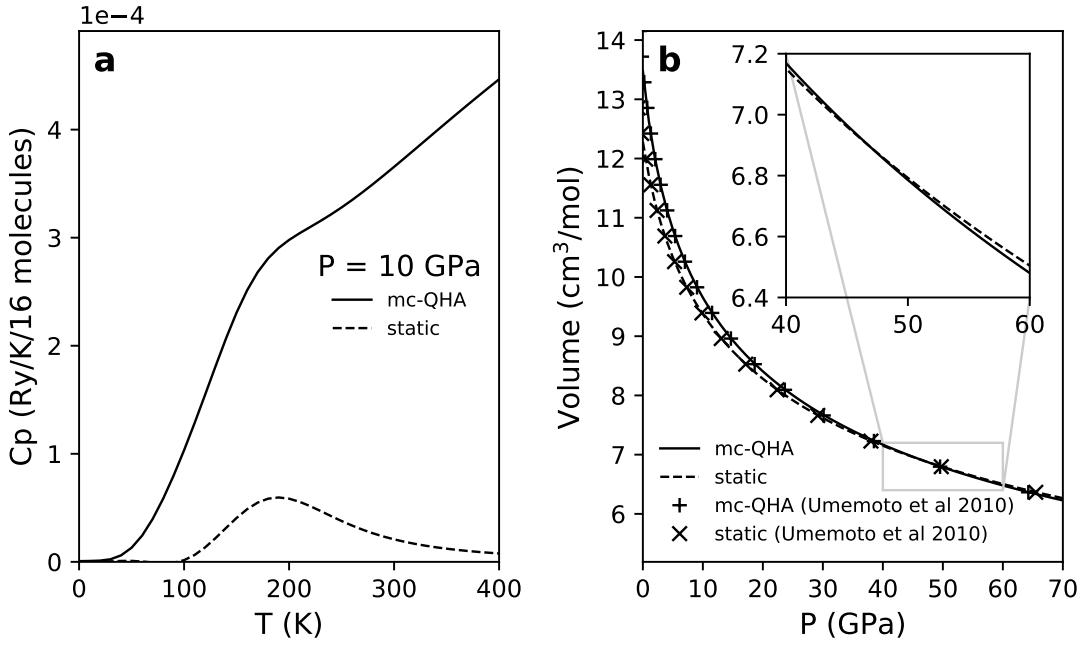

Figure 3.2: (A) C_P as a function of temperature at 10 GPa for a 16-molecule supercell, the solid line denotes the full C_P in QHA, while the dashed line includes only static contribution; (B) volume as a function of pressure in both full-QHA and static calculations.

the calculated thermodynamic properties are shown in figure 3.2. In figure 3.2 (a), the molar heat capacity at constant pressure of ice for static and full-QHA cases are plotted. They are different from each other at finite temperature due to temperature-dependent vibrational entropy. The transition temperatures T_c are pinpointed by the peak of the specific heat $C_P(P,T)$. In figure 3.2 (b), two compression curves (the third-order Birch–Murnaghan equations of state) are shown for static and full-QHA cases. Below 40 GPa, the full-QHA volume is larger than the static one. This is a normal effect of the QHA; the zero-point motion and the increase of temperature lead to volume expansion in usual materials. Above 50 GPa, however, the full-QHA volume becomes smaller than the static one. This behavior is specific to the hydrogen-bond systems in which the O – H stretching phonon-mode frequencies decrease rapidly ([101]). In figure 3.3 we plot the probabilities of the 52 configurations dependent on temperatures and pressures. On the left panel,

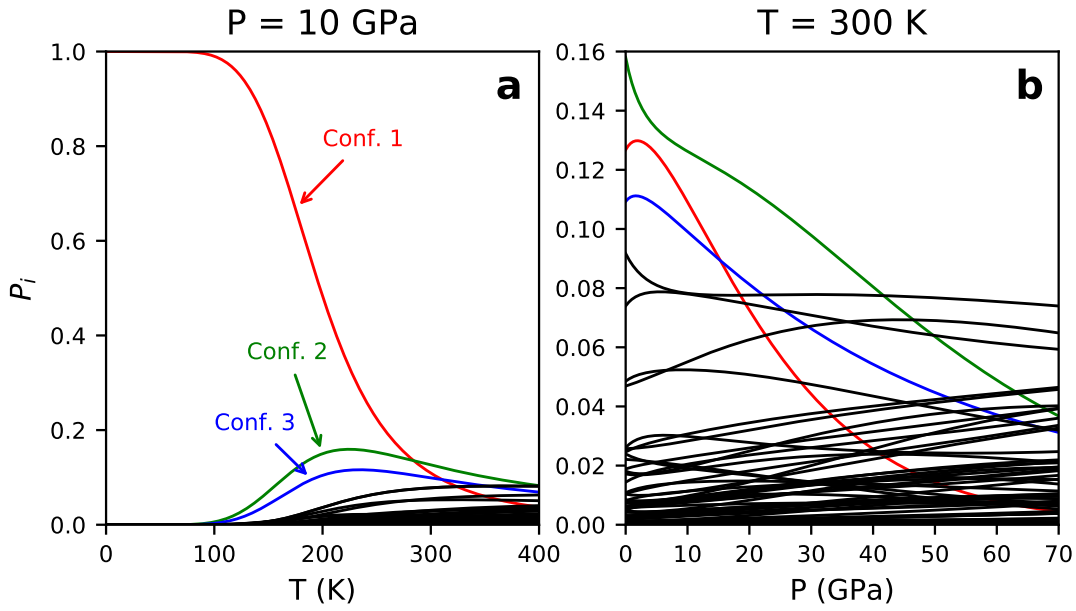

Figure 3.3: Probabilities of the 52 symmetrically inequivalent configurations generated by the 16-molecule supercell at: (a) 10 GPa and (b) 300 K.

at very low T, the probability of the first configuration, i.e., VIII phase is almost 1. With increasing temperature, the first configuration starts to be less dominant while the other configurations starting emerging. Such molecular reorientation will continue until the transition to phase VII is completed. Such growth and decay of configurations also happen with increasing/decreasing P at constant T (see the right panel of figure 3.3). Thus, the contributions from the second to the last configurations are not negligible and must be all taken into account. These results produced by the `qha` package coincide well with published results.

The settings files for both QHA and static calculation are listed in the table 3.3.

To execute the program, just enter the `examples/ice VII/` directory and run command `qha run settings.yaml`.

The execution time is about 20 s on a standard desktop. Run `qha plot settings.yaml` in the same directory for plotting the results if a quick check is desired. All calculated thermodynamic properties are stored as text files in the `examples/ice`

`VII/results` directory.

3.6 Conclusions

The `qha` package can calculate the equation of state and the thermodynamic properties for both single- and multi-configuration system within the framework of QHA. Also as the `qha` package is very extensible, it can easily be integrated with other Python packages such as `abipy` ([102]).

Table 3.2: A description of the core modules

Module name	Description
`settings.py`	Provide some default computational settings, which can be overridden by user settings.
`calculator.py`	Provide three classes that deal with single- and multi-configuration calculations. For the latter, one class for same phonon DOS and the other for different phonon DOS are given.
`statmech.py`	Calculate the vibrational contribution to Helmholtz free energy.
`single_configuration.py`	If there is only one configuration, its free energy on the coarser (V, T) grid is calculated.
`same_phonon_dos.py`	Calculate the free energy for a multi-configuration system, with only one phonon DOS provided. The vibrational contribution to its Helmholtz free energy is calculated the same way as in a single-configuration calculation, but with the static part using equation (3.5).
`different_phonon_dos.py`	Calculate the free energy for a multi-configuration system using the equation (3.8).
`fitting.py`	Provide Birch–Murnaghan equation-of-state fitting functions.
`grid_interpolation.py`	Perform Birch–Murnaghan equation-of-state fitting on the automatically generated volume grid.
`thermodynamics.py`	Given the Helmholtz free energy and equation of state as intermediate input, all thermodynamic properties are calculated.
`v2p.py`	Convert thermodynamic properties from (T, V) grid to (T, P) grid
`unit_conversion.py`	Contain functions of unit-conversions
`out.py`	Write all calculated thermodynamic properties into text files

Table 3.5: A list of the important output properties as functions of temperature and pressure

Property name	Output
Helmholtz free energy	`f_tp_ry.txt` or `f_tp_ev.txt`
Gibbs free energy	`g_tp_ry.txt` or `g_tp_ev.txt`
Internal energy	`u_tp_ry.txt` or `u_tp_ev.txt`
Enthalpy	`h_tp_ry.txt` or `h_tp_ev.txt`
Volume	`v_tp_bohr3.txt` or `v_tp_ang3.txt`
Isobaric heat capacity	`cp_tp_jmolk.txt`
Volumetric heat capacity	`cv_tp_jmolk.txt`
Isothermal bulk modulus	`bt_tp_gpa.txt`
Derivative of the isothermal bulk modulus with respect to pressure	`btp_tp.txt`
Adiabatic bulk modulus	`bs_tp_gpa.txt`
Thermal expansion coefficient	`alpha_tp.txt`
Thermal Grüneisen parameters	`gamma_tp.txt`

Chapter 4

Ab initio study of water speciation in forsterite

In this ab initio study, we expand previous investigations of charge-balanced hydrous Mg ($(2H)^{X}_{Mg}$) and Si ($(4H)^{X}_{Si}$) defects in forsterite, the Mg end-member of olivine, to address the relative stability of these two defects. First, we systematically search for $(2H)^{X}_{Mg}$ configurations to find possible defect states; second, we include the contribution of vibrational energy and defect configurational entropy in the calculation of formation energies of both defects; third, we address the effect of pressure and temperature simultaneously on their relative stability. Based on these considerations, we demonstrate that hydrous Mg defects ($(2H)^{X}_{Mg}$) can be stabilized with respect to hydrous Si defects ($(4H)^{X}_{Si}$) at relevant mantle conditions and that configurational entropy and vibrational free energy play key roles in this stabilization. Our results reveal that water speciation in olivine is influenced by temperature and pressure. As mantle physical and chemical properties may be affected by the speciation of water in olivine, application of experimental results to the mantle should account for the temperature- and pressure-dependent changes in water speciation.

4.1 Introduction

A feature unique to our planet is that over 70% of its surface is covered by liquid water, which is an essential factor of its habitability. Over the decades, it has become evident

that water is not only present at Earth's surface, but is also stored in large quantities in its interior [103, 10, 104, 11, 13]. Recently, a ringwoodite inclusion in diamond revealed that the mantle transition zone is at least locally "wet" with near 1 wt% H_2O [105]. Plate tectonics is responsible for the deep-Earth water cycle, carrying hydrous minerals and water-bearing sediments into the mantle via subduction. Water then returns to the surface by magmatic degassing beneath mid-ocean ridges and oceanic islands [106, 107]. Most of the water in Earth's surface today might come from the degassing of the Earth's mantle through volcanism shortly after the Earth formed [108].

Water is transported into the mantle during subduction chiefly as hydroxyl groups in hydrous silicate minerals [106, 107, 109, 110]. As most hydrous minerals are not stable along the normal mantle geotherm, water delivered to the convecting mantle is believed to be stored chiefly as hydrous defects (hydroxyl point defects) in minerals that do not contain hydrogen in their stoichiometric formulas. These so-called nominally anhydrous minerals (NAMs) include olivine, pyroxene, and garnet [10]. Though present in modest concentrations, these defects dramatically influence the physical and chemical properties of their hosts, including the electrical conductivity [23, 111, 112] and viscosity [113, 114, 18, 21, 22], the latter having a strong effect on mantle processes such as convection. Water also decreases the solidus temperature of mantle rocks and, consequently, the extent and composition of partial melting [115, 116].

To understand the influence of water on mantle properties, the mechanisms of water incorporation in olivine, the most voluminous mineral in the upper mantle, must be clarified. In the past few decades, this problem has been addressed by various methods, for example, IR spectroscopy [117, 118, 119, 120, 121, 122, 123, 124, 125, 126, 127, 128, 129], Raman spectroscopy [130], NMR spectroscopy [131, 132], and theoretical calculations [133, 134, 135, 136, 137, 138, 139, 26]. Several water incorporation mechanisms in olivine have been proposed. Among them, the most likely ones are the formation of hydroxyl groups (OH^-) associated with vacant Mg and Si vacancies [133, 135, 140, 137, 138, 139, 26, 128], represented, respectively, as $(2H)^{X}_{Mg}$ and $(4H)^{X}_{Si}$ with Kröger-Vink notation [141]. These defects in forsterite, the Mg end-member of olivine, have been investigated extensively. Nevertheless, a long-standing debate remains concerning the relative thermodynamic stability of these defects [12]. Measurements of cation diffusion and hydrogen solubility in olivine suggest that hydrous defects are chiefly

associated with metal (Mg and Fe) vacancies (octahedral vacancies) [27, 142]. In contrast, IR spectroscopy [119, 143, 120, 124, 126, 127, 128] and NMR [132] indicate that hydrous defects associated with the Si vacancy dominate in olivine. Also, ab initio calculations have consistently indicated that the Si hydrous defect, $(4H)^{X}_{Si}$, is energetically favored over the Mg defect, $(2H)^{X}_{Mg}$ [140, 139, 26, 144].

In this ab initio study, we expand previous investigations of the charge-balanced hydrous Mg and Si defects, $(2H)^{X}_{Mg}$ and $(4H)^{X}_{Si}$, in forsterite (Mg_2SiO_4) to address their relative stability. First, we explore systematically the configurations for the $(2H)^{X}_{Mg}$ defect. Multiple possible configurations of both $(2H)^{X}_{Mg}$ and $(4H)^{X}_{Si}$ are considered in this study. Second, we include the contribution of vibrational free energy and defect configurational entropy in the calculation of formation energies of these defects. Third, we address the effect of pressure and temperature simultaneously on their relative stability. Based on these results, we demonstrate that the Mg defect may be stabilized with respect to Si defect at relevant mantle conditions. We conclude that vibrational free energy, configurational entropy, and proper identification of the configurations of these defects are essential to determining the relative stability field of hydrous defects.

4.2 Methods

4.2.1 Chemical reactions to create these hydrous defects

To investigate the relative stability of $(2H)^{X}_{Mg}$ and $(4H)^{X}_{Si}$ defects, the formation energies are calculated from the following two reactions between forsterite and water:

$$H_2O + 16\,Mg_2SiO_4 = H_2Mg_{31}Si_{16}O_{64} + MgO^{(\text{periclase})} \tag{4.1}$$

$$2\,H_2O + 16\,Mg_2SiO_4 = H_4Mg_{32}Si_{15}O_{64} + SiO_2{}^{(\text{quartz/stishovite})}. \tag{4.2}$$

Here, H_2O is an isolated water molecule, and Mg_2SiO_4 is forsterite; the products $H_2Mg_{31}Si_{16}O_{64}$ and $H_4Mg_{32}Si_{15}O_{64}$ are hydrogen-bearing olivine with two protons associated with a Mg vacancy and four protons associated with a Si vacancy, respectively. At upper mantle conditions, MgO and SiO_2 in these equations further react with react with pyroxene ($MgSiO_3$) and forsterite (Mg_2SiO_4) to form forsteriteand pyroxene,

respectively, which in turn become

$$H_2O + MgSiO_3 + 15\,Mg_2SiO_4 = H_2Si_{31}Si_{16}O_{64} \tag{4.3}$$

$$2\,H_2O + 17\,Mg_2SiO_4 = H_4Mg_{32}Si_{15}O_{64} + 2\,MgSiO_3. \tag{4.4}$$

Therefore, the formation energies of one $(2H)^{X}_{Mg}$ ($G_r^{(2H)^{X}_{Mg}}$) and one $(4H)^{X}_{Si}$ ($G_r^{(4H)^{X}_{Si}}$) defect, without considering the lattice configurational entropy are given by

$$G_r^{(2H)^{X}_{Mg}} = G_{H_2Mg_{31}Si_{16}O_{64}} - (G_{H_2O} + G_{MgSiO_3} + 15G_{Mg_2SiO_4}) \tag{4.5}$$

$$G_r^{(4H)^{X}_{Si}} = G_{H_4Mg_{32}Si_{15}O_{64}} + 2G_{MgSiO_3} - (2G_{H_2O} + 17G_{Mg_2SiO_4})\,. \tag{4.6}$$

Since we are interested in the relative stability of these defects, the quantity ΔG_f is calculated as equation (4.6) – 2 × equation (4.5), which results in the same reaction considered by Walker et al. [139] in their equation 3. Here, Gibbs free energies of all phases are obtained by ab initio computations. The hydrous defects $H_2Mg_{31}Si_{16}O_{64}$ and $H_4Mg_{32}Si_{15}O_{64}$ are investigated using a 2 × 1 × 2 supercell of forsterite with 2 and 4 protons substituting for one Mg or Si cation, respectively. Seven previously identified configurations for the $(4H)^{X}_{Si}$ defect and nine configurations of the $(2H)^{X}_{Mg}$ defect are considered in our calculations and illustrated in figure 4.1.

4.2.2 Gibbs free energy

The Gibbs free energy of these multi-configurational system are calculated using the method described in chapter 3. As calculating the vibrational density of state (VDOS) of hydrogen-bearing olivine for every symmetrically inequivalent configuration is computational resource demanding, we use a single VDOS for all $(2H)^{X}_{Mg}$ defects and another for all $(4H)^{X}_{Si}$ defects. These VDOSs were obtained using the lowest energy configurations. As shown in figure 4.2, the VDOS for pure olivine and olivine with $(2H)^{X}_{Mg}$ and $(4H)^{X}_{Si}$ are similar, except for peaks associated with OH^- modes. Thus the equation (3.4) is used to calculate the Helmholtz free energy. Then the pressure are given by $P(V,T) = -\left(\frac{\partial F(V,T)}{\partial V}\right)_T$, and the Gibbs free energy are calculated with $G(P,T) = F(V,T) + P(V,T)V$, including the internal configurational entropy, but exclusive of the lattice configurational entropy.

4.2.3 Lattice configuration entropy

A key ingredient in this study is the (lattice) configurational entropy. Since one $(4H)^{X}_{Si}$ contains four protons and one $(2H)^{X}_{Mg}$ contains two, twice the number of $(2H)^{X}_{Mg}$ defects as $(4H)^{X}_{Si}$ defects are required to account for a given amount of hydrogen. Therefore, the lattice configurational ("mixing") entropies are different, which changes the relative formation energies of $(2H)^{X}_{Mg}$ and $(4H)^{X}_{Si}$ defects as well as their relative stabilities. At low defect concentrations, defect-defect interactions are expected to be negligible and the configurational entropy is

$$S^{v}_{conf} = -R\left[(1-x_v)\ln(1-x_v) + x_v \ln x_v\right], \tag{4.7}$$

where x_v is the number of vacancies per formula unit, that is, the number of $(2H)^{X}_{Mg}$ and $(4H)^{X}_{Si}$ per formula unit.

The assumption that all hydrous vacancies are locally charge balanced, that is, all of the protons are located in the vacant Mg or Si sites[133, 140, 137, 138, 139, 26, 145] is made in this calculation. After considering the lattice configurational entropies, the difference in formation energy between $(2H)^{X}_{Mg}$ and $(4H)^{X}_{Si}$ defects in one mole of forsterite is given by

$$\Delta G_r(P,T) = \left[x_{(2H)^{X}_{Mg}} N_A G_r^{(2H)^{X}_{Mg}} - TS_{conf}^{(2H)^{X}_{Mg}}\right] - \left[x_{(4H)^{X}_{Si}} N_A G_r^{(4H)^{X}_{Si}} - TS_{conf}^{(4H)^{X}_{Si}}\right]. \tag{4.8}$$

Here, $x_{(2H)^{X}_{Mg}}$ and $x_{(4H)^{X}_{Si}}$ are the concentration of the two hydrous defects, and N_A is Avogadro's number. The equation above clearly indicates that the relative stability of these defects depends on defect concentration (water content), temperature, and pressure.

4.2.4 DFT calculations

At the low defect concentrations relevant for the mantle, the probability of interactions between the hydrous defects considered in this paper is small. Therefore, we use a supercell composed of 112 atoms in defect-free forsterite with a single defect as previously used by Umemoto et al. [26]. For the hydrous Mg vacancies reported in previous studies, the lowest-energy configuration consists of two protons bonded to two oxygen ions lying

nearly along the O2-O1 edges of a Mg1 vacancy. As there are six oxygen ions per Mg-O polyhedron, there are 15 ($_6C_2$) possible configurations, not all equivalent, if all the protons are located inside of the Mg1 vacancy, and as one or two protons can point outward of the Mg1 vacancy, there are actually more possibilities. Therefore, a series of different structures were systematically created and optimized to search for possible configurations. Static calculations for all structures were performed with Local Density Approximation (LDA) [52] and Generalized Gradient Approximation (GGA) [54] exchange-correlation functionals using the Quantum-ESPRESSO software [95]; the planewave cutoff was chosen to be 544 eV. The pseudopotentials for Si, O, and H were generated by Vanderbilt's method [58], and the pseudopotential for Mg was generated by von Barth-Car's method [146]. The details of GGA pseudopotentials of Si, O, Mg, and H are the same as those used in Umemoto et al. [26], and the LDA pseudopotentials of Si, O, and Mg are the same as those used in Umemoto et al. [147]. Brillouin Zone sampling was performed on a displaced 2 × 2 × 2 grid for all supercells. The vibrational density of states (VDOS) for defect free structures were obtained using the GGA functional using density functional perturbation theory [64]. For strongly bonded materials such as oxides and silicate, VDOS, and thermodynamics properties obtained from LDA and GGA calculations often are similar, but for structures with hydrous defects, the GGA functional is more appropriate [148]. The dynamical matrices were computed on a 2 × 2 × 2 q-point grid. Obtained force constant matrices were then interpolated on a 6 × 6 × 6 q-point gird. The VDOS of the pyroxene and pure olivine are originally from Yu et al.[149, 150].

4.3 Results

4.3.1 Defect structures

All investigated hydrous defects are presented in figure 4.1 and table 4.1, listed in order of increasing static energy obtained in GGA level. Nine configurations of $(2H)^{X}_{Mg}$ were found based on a systematic search starting from essentially random structures. Configurations 3 and 5–8 of $(2H)^{X}_{Mg}$ are twofold degenerate owing to the mirror symmetry plane perpendicular to the c axis in defect-free forsterite. The others are non-degenerate. Configurations 1–7 of the $(4H)^{X}_{Si}$ defect were all previously identified

[140, 139, 151, 26, 132]. Configurations 1, 2, 4, and 6 of $(4H)^{X}_{Si}$ are from our previous study[26], while Configurations 3, 5, and 7 of $(4H)^{X}_{Si}$ correspond to Configurations 3–5 in Xue et al. [132]. Configurations 2, 3, and 4 of $(4H)^{X}_{Si}$ are twofold degenerate owing to the mirror symmetry plane perpendicular to the c axis in defect-free forsterite, while the others are non-degenerate. In Configurations 4 and 6, four protons stay close to the surface of the $(4\,H)_{Si}O_4$ tetrahedron In Configurations 1 and 2, one proton points away from the $((4\,H)_{Si}O_4$ tetrahedron; in Configurations 3 and 5, two protons point away from the (4H)SiO4 tetrahedron and in Configuration 7 three protons point away from the $(4\,H)_{Si}O_4$ tetrahedron ([132]). Among all configurations of the $(4H)^{X}_{Si}$ defect, the most stable ones are Configurations 1, 2, and 3, consistent with previous studies [152, 26, 132]. The energy differences between other configurations and Configuration 1 agree with those in Xue et al. [132] (see table 4.1). Information about the energies, probabilities, and structures of these defects are shown in the table 4.1 and the supplementary file (Deposit item AM-18-56262, supplemental table and CIF. `http://www.minsocam.org/MSA/AmMin/TOC/2018/May2018_data/May2018_data.html`). The probabilities of finding configurations in thermodynamic equilibrium at a given temperature are given by

$$p_i = \frac{w_i \exp\left(\frac{E_i}{k_B T}\right)}{\sum_j w_j \exp\left(\frac{E_j}{k_B T}\right)} \tag{4.9}$$

where w_i and E_i are the configurational degeneracy and static energy for the i-th configuration [134, 138, 26].

Previous studies indicate that the formation energy of the Mg1 vacancy is 0.54 eV lower than that of the Mg2 vacancy [140, 26]. Similarly, the formation energy of the hydrous Mg1 defect is lower than that of the hydrous Mg2 defect [140, 151, 26]; thus, we focus here on hydrous Mg1 defects only. Some of the configurations of $(2H)^{X}_{Mg}$ were proposed by Walker et al.[138], including all the configurations with protons connected to two oxygen ions inside or along the edges of the oxygen octahedron. The structure of the lowest-energy configuration of $(2H)^{X}_{Mg}$ has two protons bonded to O2 ions, sitting close to the O2-O1 edge of the Mg1 octahedral vacancy. However, the energy difference between this and other structures are somewhat different from those calculated by Walker et al. [138]. This difference is likely caused by the use of different methods, Mott-Littleton

Table 4.1: Degeneracies, relative energies, and probabilities of various defects (static calculation)

$(4H)^{X}_{Si}$	Degeneracy	$E_{Conf.x} - E_{Conf.1}$ (eV)	Prob.(300 K)	Prob.(1500 K)
Conf. 1	1	0.00 (0.00)	0.497 (0.186)	0.225 (0.199)
Conf. 2	2	0.02 (–0.02)	0.458 (0.806)	0.386 (0.465)
Conf. 3	2	0.08 (0.10)	0.045 (0.008)	0.243 (0.184)
Conf. 4	2	0.23 (0.21)	0.000 (0.000)	0.076 (0.078)
Conf. 5	1	0.23 (0.27)	0.000 (0.000)	0.038 (0.025)
Conf. 6	1	0.33 (0.20)	0.000 (0.000)	0.018 (0.042)
Conf. 7	1	0.36 (0.45)	0.000 (0.000)	0.014 (0.006)
$(2H)^{X}_{Mg}$				
Conf. 1	1	0.00 (0.00)	0.996 (0.500)	0.603 (0.417)
Conf. 2	1	0.14 (0.24)	0.004 (0.000)	0.204 (0.065)
Conf. 3	2	0.29 (0.33)	0.000 (0.000)	0.128 (0.065)
Conf. 4	1	0.48 (0.00)	0.000 (0.500)	0.015 (0.417)
Conf. 5	2	0.52 (0.58)	0.000 (0.000)	0.022 (0.009)
Conf. 6	2	0.54 (0.55)	0.000 (0.000)	0.018 (0.012)
Conf. 7	2	0.63 (0.73)	0.000 (0.000)	0.009 (0.003)
Conf. 8	2	0.89 (0.55)	0.000 (0.000)	0.001 (0.012)
Conf. 9	1	0.93 (1.01)	0.000 (0.000)	0.000 (0.000)

Numbers outside (inside) parentheses correspond to PBE-GGA(LDA) results.

method in Walker et al. [138] and density functional theory in our study. The formation energies of configurations having two protons sitting along the edges or pointing to the interior of the oxygen octahedron are normally lower than configurations containing one or two protons pointing out of the oxygen octahedron. The latter ones have high formation energies and are less probable (see table 4.1)

The energy differences obtained with LDA are listed in parentheses in table 4.1. They differ slightly from those obtained with GGA. For example, with LDA, Configuration 2 of $(4H)^{X}_{Si}$ becomes more stable than Configuration 1, but Configurations 1–3 are still the most stable ones. For the $((2H)^{X}_{Mg}$ defect, Configuration 4 turns into Configuration 1 after lattice relaxation with LDA, while with GGA this structure change occurs after 8 GPa. Configuration 5 of $(2H)^{X}_{Mg}$ turns into Configuration 6 at 10 GPa and 12 GPa with LDA and GGA calculations, respectively. Configurations 6 and 2 turn out to be the same after optimization in LDA calculations, while they remain distinct in GGA

calculations. These pattern of defect relaxation indicates strong anharmonic effects, with possibly shallow local energy minima in configuration space, and confirms that anharmonic effects can be very sensitive to the choice of exchange-correlation functional when relatively weak bonds are involved [78].

Substitution of Mg or Si by H atoms increases the average distance between oxygen ions in the substitutional site and the polyhedron volume. The volumes of regular SiO_4 and Mg_1O_6 polyhedra are 2.32 and 12.10 $Å^3$ at 0 GPa and 2.25 and 11.20 $Å^3$ at 12 GPa, respectively, demonstrating that the volume of SiO_4 and Mg_1O_6 polyhedra decrease by 3.0 and 7.4%, respectively, as pressure increases to 12 GPa. For all defect configurations, the $(4\,H)_{Si}O_4$ tetrahedron at 0 GPa is much larger (40%) and more compressible than the regular SiO_4 tetrahedron. On the one hand, the volume of the defect in Configuration 1 changes from 3.27 $Å^3$ at 0 GPa to 2.85 $Å^3$ at 12 GPa (volume compressed by 12.8%). On the other hand, the $(2\,H)_{Mg}O_6$ octahedron is only slightly larger (4% larger) than that of Mg_1O_6, with its volume changing from 12.58 $Å^3$ at 0 GPa to 11.01 $Å^3$ at 12 GPa (volume compressed by 12.5%). Generally, the OH bond length in$(2H)^{X}_{Mg}$ is larger than that in $(4H)^{X}_{Si}$, and most of these bond lengths increase with increasing pressure, a sign of hydrogen bond formation with another oxygen across the interstitial site [153, 154, 155].

4.3.2 Stability of dominant defects

After computing vibrational free energies and configurational entropies of the two types of hydrous vacancies considered in this study, the difference in formation energies vs. water content, temperature, and pressure (see equation (4.8)) can be computed. This free energy difference, $\Delta_r^{LDA}(P,T)$ and $\Delta_r^{GGA}(P,T)$ at 0 and 12 GPa are shown in figure 4.3. It is clear that the formation energy difference and, therefore, the predominance of one defect population over the other, depend on both pressure and temperature. Both LDA and GGA calculations predict that $(2H)^{X}_{Mg}$ defects dominate at high temperatures, while $(4H)^{X}_{Si}$ defects dominate at ambient temperature. For instance, at a typical upper mantle pressure and temperature (12 GPa and 1700 K), the hydrous Mg defect is more stable. The key to this high-temperature stabilization is the configurational entropy.

4.4 Discussion

To investigate the origin of the relative stability of these two defects at different pressures and temperatures, we recalculated the free energy difference (equation (4.8)) by examining the effect of various terms contributing to the free energy difference at GGA level. First, figure 4.3 clearly indicates that by increasing pressure the stability field of the hydrous Si defect is extended to higher temperatures. This pressure effect is best investigated at 0 K. In Figure 4, the enthalpy difference $\Delta G_{\mathrm{r}}^{GGA}(P,0) = \Delta H_r(P,0)$ and the contribution of $P\Delta V\mathrm{r}(P)$ to ΔH_{r} are plotted as a function of pressure. The stability of the $(4\mathrm{H})_{\mathrm{Si}}^{\mathrm{X}}$ defect increases with increasing pressure primarily because this defect is more compressive than the hydrous Mg defect, as noted above. Therefore, it is clearly very important to obtain the correct pressure dependences for these defect structures.

The stabilization of the $(2\mathrm{H})_{\mathrm{Mg}}^{\mathrm{X}}$ defect with increasing temperature is easier to understand. This defect is stabilized by entropy; but, as indicated above, there are several contributions to the configurational entropy, including the lattice configurational entropy and the entropy caused by different internal configurations of certain hydrous defect. The latter can be investigated by considering different numbers of $(2\mathrm{H})_{\mathrm{Mg}}^{\mathrm{X}}$ and $(4\mathrm{H})_{\mathrm{Si}}^{\mathrm{X}}$ defects separately.

Effects of internal configuration entropy of $(2\mathrm{H})_{\mathrm{Mg}}^{\mathrm{X}}$ and $(4\mathrm{H})_{\mathrm{Si}}^{\mathrm{X}}$ defects are illustrated in figure 4.5a and figure 4.5b, respectively, as plots of temperature vs. water content. Below (above) the line the free energy difference favors $(4\mathrm{H})_{\mathrm{Si}}^{\mathrm{X}}$ defects $(2\mathrm{H})_{\mathrm{Mg}}^{\mathrm{X}}$ defects. In figure 4.5a, the relative stability of $((2\mathrm{H})_{\mathrm{Mg}}^{\mathrm{X}}$ defect increases by increasing the number of $(2\mathrm{H})_{\mathrm{Mg}}^{\mathrm{X}}$ configurations considered, but changes little when the number of configurations exceeds seven. This result can be explained by the probabilities of these configurations (table 4.1). The probabilities of Configurations 8–9 are negligible even at high temperature due to their high formation energies. A similar trend is also observed for $(4\mathrm{H})_{\mathrm{Si}}^{\mathrm{X}}$ defect configurations. The stability of this type of defect changes little when these low probability configurations are included. The most influential configurations are those with low energy and high probability. Therefore, taking more configurations with larger formation energies of $(2\mathrm{H})_{\mathrm{Mg}}^{\mathrm{X}}$ and $(4\mathrm{H})_{\mathrm{Si}}^{\mathrm{X}}$ defects will not change further their relative stability. Figure 4.5 indicates that nine configurations of $(2\mathrm{H})_{\mathrm{Mg}}^{\mathrm{X}}$ and seven configurations of $(4\mathrm{H})_{\mathrm{Si}}^{\mathrm{X}}$ defects are sufficient to investigate the relative stability of these two

defect types. This result clearly points to the importance of proper identification and sampling of possible defect configurations in these calculations.

The impact of various entropy sources on the formation energy difference of these two hydrous defects is illustrated in figure 4.6 as function of temperature and water content. Figures 4.6a and 4.6b include contributions from the internal configurational entropy for variable numbers of defect configurations in each site and exclude contributions from vibrational (entropic or enthalpic) free energy, Gvib, as well as "mixing" free energy, $G_{\mathrm{mix}} = \breve{} TS_{\mathrm{conf}}$, where S_{conf} is given by equation (4.7). These figures indicate how the relative stability of these defects varies with the number of configurations identified. In particular, the $(4\mathrm{H})^{\mathrm{X}}_{\mathrm{Si}}$ defect stability can be overestimated if an insufficient number of $(2\mathrm{H})^{\mathrm{X}}_{\mathrm{Mg}}$ defect configurations is included. Figures 4.6c and 4.6d demonstrate that inclusion of vibrational effects further stabilize the $(2\mathrm{H})^{\mathrm{X}}_{\mathrm{Mg}}$ relative to the $(4\mathrm{H})^{\mathrm{X}}_{\mathrm{Si}}$ defect. This effect is due to the lower frequency of O-H vibrational modes in the $(2\mathrm{H})^{\mathrm{X}}_{\mathrm{Mg}}$ (see figure 4.2). Figures 4.6e and 4.6f indicate that the $(2\mathrm{H})^{\mathrm{X}}_{\mathrm{Mg}}$ defect stability increases to a greater extent when the contribution of lattice configuration entropy (G_{mix}) is include. For nearly the same water content, the number of $(4\mathrm{H})^{\mathrm{X}}_{\mathrm{Si}}$ defects is half the number of $(2\mathrm{H})^{\mathrm{X}}_{\mathrm{Mg}}$ defects, and, therefore, the $(4\mathrm{H})^{\mathrm{X}}_{\mathrm{Si}}$ defects contribute less entropy resulting in the destabilization of $(4\mathrm{H})^{\mathrm{X}}_{\mathrm{Si}}$ at higher temperatures. This effect is clearly dependent of water content in the range of water concentration expected in natural olivine samples, that is, less than 1000 ppmw [13]. A comparison between the diagrams presented in figures 4.5a - 4.5b and 4.6a - 4.6f provides a clear indication of the necessity to include all internal defect configurations, G_{mix}, and G_{vib}simultaneously in these calculations. This conclusion is general and applies to all hydrous defects in nominally anhydrous minerals. The results discussed above clearly point out the increase stability of the $(2\mathrm{H})^{\mathrm{X}}_{\mathrm{Mg}}$ defect with increasing temperature.

Our results correspond to situations where thermodynamic equilibrium can be achieved in the presence of enstatite. As pointed out earlier [139], the relative stability of these defects depends on the nature of coexisting phases. However, the increased stability of the $(2\mathrm{H})^{\mathrm{X}}_{\mathrm{Mg}}$ defect with increasing temperature is independent of the coexisting phase. This situation is primarily due to the lattice configuration entropy effect. Here we emphasize that the internal configuration entropy of these defects also affects their relative stability. It is not a trivial exercise to identify all of them and calculations need

to be approximate. Besides, as pointed out above, ab initio calculations have systematic errors that are not easily accessible and anharmonic effects might be important as well. Also, one can easily imagine other defect states not addressed here, for example, similar Mg2 defects, interstitial protons, etc. For instance, $\left\{(3\mathrm{H})^{/}_{\mathrm{Si}} + \mathrm{H}^{\cdot}_{i}\right\}^{\mathrm{x}}$, i.e., three protons in the Si vacancy and one proton in the interstitial site, or similarly $\left\{(\mathrm{H})^{/}_{\mathrm{Mg}} + \mathrm{H}^{\cdot}_{i}\right\}^{\mathrm{x}}$, have much larger entropy owing to the large number of configurations available for interstitial protons. The free energy of these defects should also be carefully investigated for obtaining a full picture of their relative stability. Therefore, direct comparison of these results with experimental observations can be subtle and difficult.

4.5 Implications

Our results have some interesting implications, despite their uncertainties. The destabilization of $(4\mathrm{H})^{\mathrm{X}}_{\mathrm{Si}}$ with respect to the $(2\mathrm{H})^{\mathrm{X}}_{\mathrm{Mg}}$ defect with increasing temperature, as shown in figure 4.3, should produce changes in experimental IR spectra, if equilibrium conditions are achieved. Similarly, the populations of different $(4\mathrm{H})^{\mathrm{X}}_{\mathrm{Si}}$ or $(2\mathrm{H})^{\mathrm{X}}_{\mathrm{Mg}}$ defects also depend on temperature (see table 4.1) and could equally well produce changes in IR spectra. The precise temperature at which such spectral changes should manifest is difficult to predict accurately given the factors mentioned above. Nevertheless, our results might explain a change in the IR spectrum of hydrous olivine, that is, a reversible change in intensity of the 3612 cm^{-1} peak, upon heating and cooling [156]. This prominent low-temperature band is thought to belong to the $(4\mathrm{H})^{\mathrm{X}}_{\mathrm{Si}}$ group, confirming our observation that equilibrium between different types of hydrous defects are temperature dependent. This band involves the coupled stretching of the four OH^{-} groups of one particular $(4\mathrm{H})^{\mathrm{X}}_{\mathrm{Si}}$ configuration and suggests that a change in the defect geometry with temperature might explain the change of IR band without requiring proton migration or a change in the nature of the hydrous defect [144]. Indeed, even within the quasi harmonic approximation (QHA), results presented in table 4.1 suggest that the probability of different $(4\mathrm{H})^{\mathrm{X}}_{\mathrm{Si}}$ defect configurations can vary considerably within the temperature range of Yang and Keppler's experiment [156]. For example, while the most stable configuration of $(4\mathrm{H})^{\mathrm{X}}_{\mathrm{Si}}$ defect is marginally more likely at 300 K, the second most stable configuration is more likely at 1500 K. While probabilities shown in table 4.1 might carry

significant uncertainties, this type of result is consistent with the proposal of Balan et al. [144]. This possibility should be addressed in the future with anharmonic calculations of the IR spectra of these different defect configurations. Our calculations indicate that water speciation in olivine is influenced by temperature and pressure, in addition to the well-known influence of the surroundings. As mantle properties may be affected by the speciation of water in olivine, application of experimental results to the mantle should account for these water-speciation dependencies.

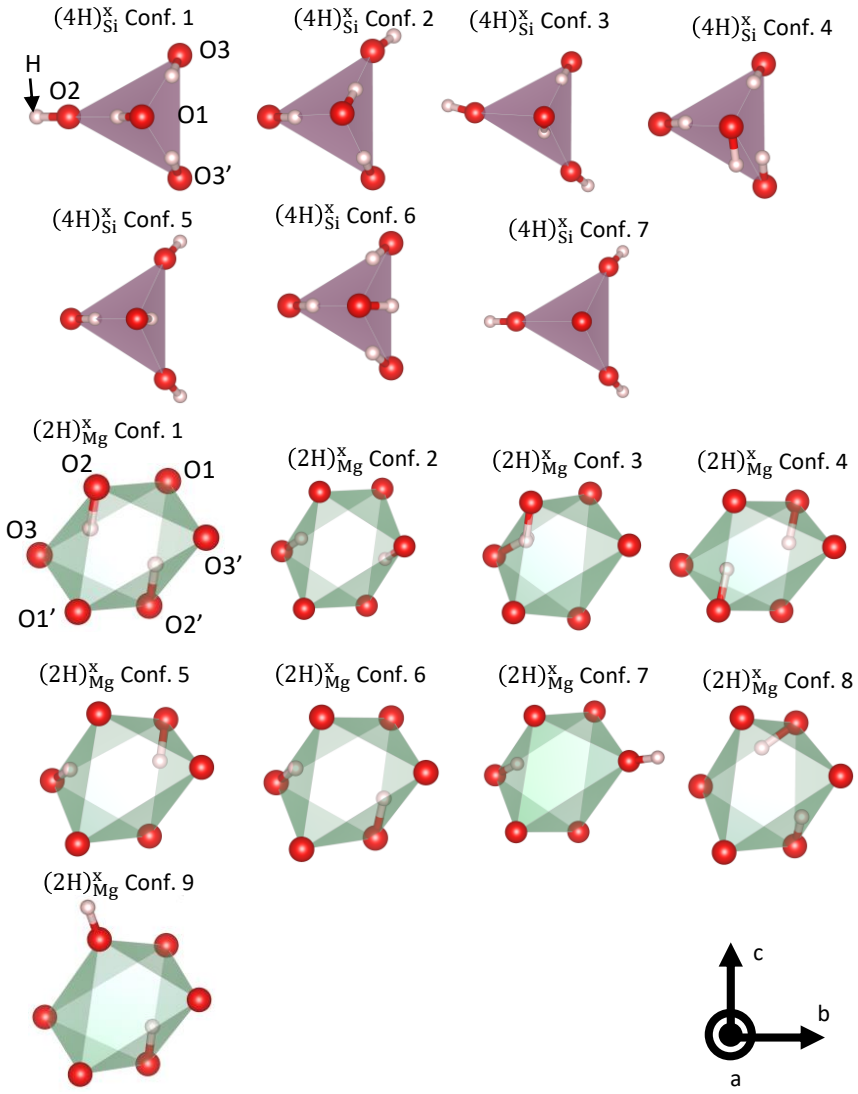

Figure 4.1: Configurations of $(4H)^{X}_{Si}$ and $(2H)^{X}_{Mg}$ defects. Red and white spheres represent oxygen ions and protons, respectively. Pink and green polyhedra represent vacant Si and Mg sites. Configurations 1, 2, 4, and 6 of $(4H)^{X}_{Si}$ and configuration 1 of $(2H)^{X}_{Mg}$ are from Umemoto et al., [26]. Configurations 3, 5, and 7 of $(4H)^{X}_{Si}$ are from Xue et al., [132] with the fourth hydrogen in configuration 7 existing just beneath O1. Configurations 1–6 and 8 of $(2H)^{X}_{Mg}$ were described in the Walker et al [138].

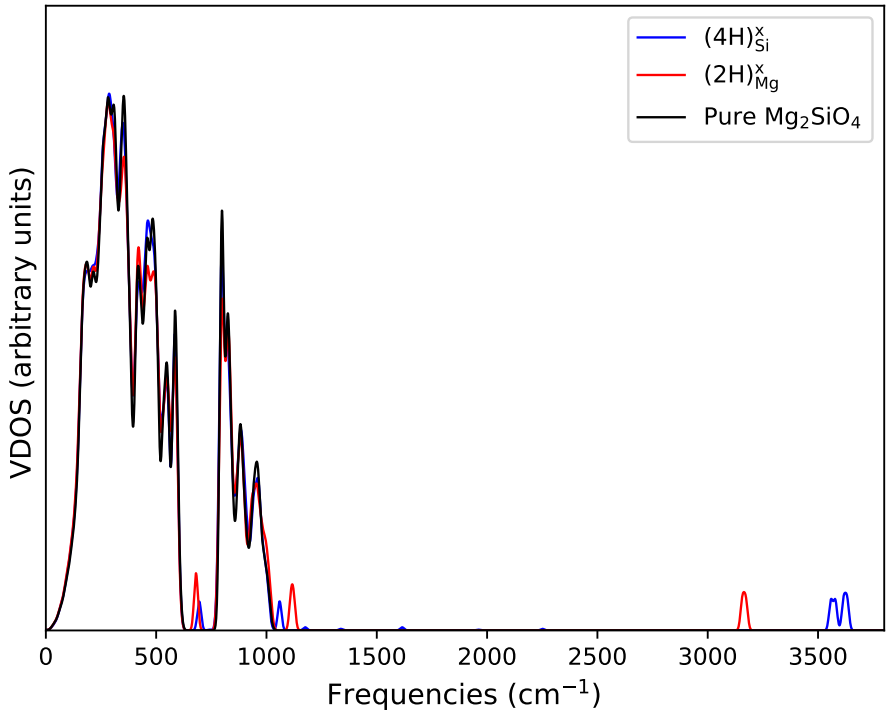

Figure 4.2: Vibrational density of states (VDOS) at GGA level for a $2 \times 1 \times 2$ supercell of forsterite at 0 GPa (see text for q point sampling). Black, red, and blue correspond to defect-free, one $(2H)^{X}_{Mg}$ and one $(4H)^{X}_{Si}$ defect configurations, respectively.

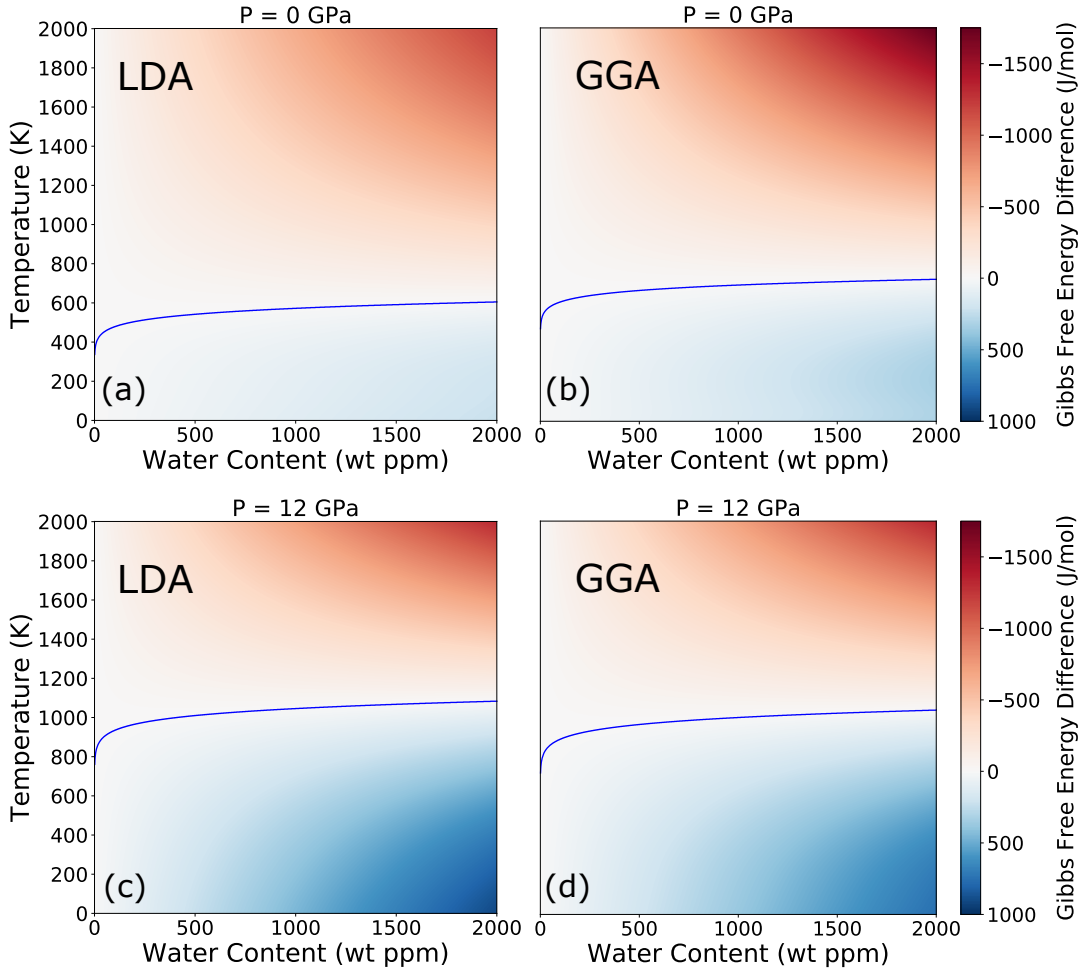

Figure 4.3: Gibbs free energy difference between the two hydrous defects considered in this study, $\Delta_{\mathrm{r}}^{LDA,GGA}(P,T)$ given by equation (4.8), in temperature–water concentration space at (a) LDA result at 0 GPa and (b) GGA result at 0 GPa; (c) LDA result at 12 GPa and (d) GGA result at 12 GPa. $(2\mathrm{H})_{\mathrm{Mg}}^{\mathrm{X}}$ is more (less) stable than $(4\mathrm{H})_{\mathrm{Si}}^{\mathrm{X}}$ defects in the red (blue) regions. The total number of distinct $(2\mathrm{H})_{\mathrm{Mg}}^{\mathrm{X}}$ and $(4\mathrm{H})_{\mathrm{Si}}^{\mathrm{X}}$ configurations considered in this study are 9 and 7, respectively. The solid line denotes the boundary between the red and blue regions, that is, $\Delta G_{\mathrm{r}}(P,T) = 0$.

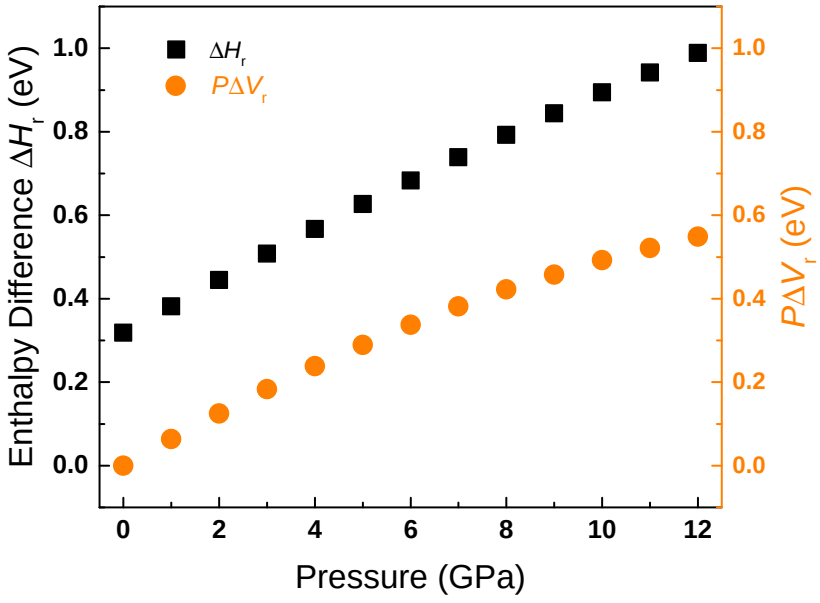

Figure 4.4: Enthalpy difference, $\Delta H_r(P,0) = 2H_{\mathrm{r}}^{(2\mathrm{H})^{\mathrm{X}}_{\mathrm{Mg}}} - H_{\mathrm{r}}^{(4\mathrm{H})^{\mathrm{X}}_{\mathrm{Si}}}$ or $\Delta H_{\mathrm{r}}(P,0) = \Delta E_{\mathrm{r}}(P) + P\Delta V_{\mathrm{r}}(P)$ and $P\Delta V_{\mathrm{r}}(P)$ obtained from equation (4.3) and equation (4.4) at 0 K (static calculation) plotted vs. pressure.

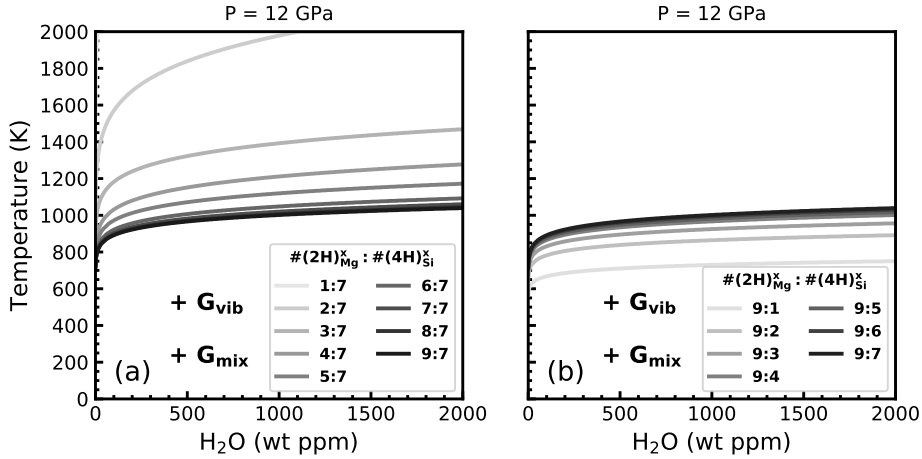

Figure 4.5: $\Delta G_{\mathrm{r}}^{GGA}(P,T) = 0$ (see equation (4.8)) at 12 GPa including different internal configuration energy contributions plotted parametrically in temperature–water content space. In (a) various numbers of distinct $(2\mathrm{H})^{\mathrm{X}}_{\mathrm{Mg}}$ configurations and seven distinct $(4\mathrm{H})^{\mathrm{X}}_{\mathrm{Si}}$ configurations are considered, while in (b) nine $(2\mathrm{H})^{\mathrm{X}}_{\mathrm{Mg}}$ and various numbers of $(4\mathrm{H})^{\mathrm{X}}_{\mathrm{Si}}$ distinct configurations are considered. The ratio of the number of distinct configurations, $\#(2\mathrm{H})^{\mathrm{X}}_{\mathrm{Mg}} : \#(4\mathrm{H})^{\mathrm{X}}_{\mathrm{Si}}$, are shown in the legend.

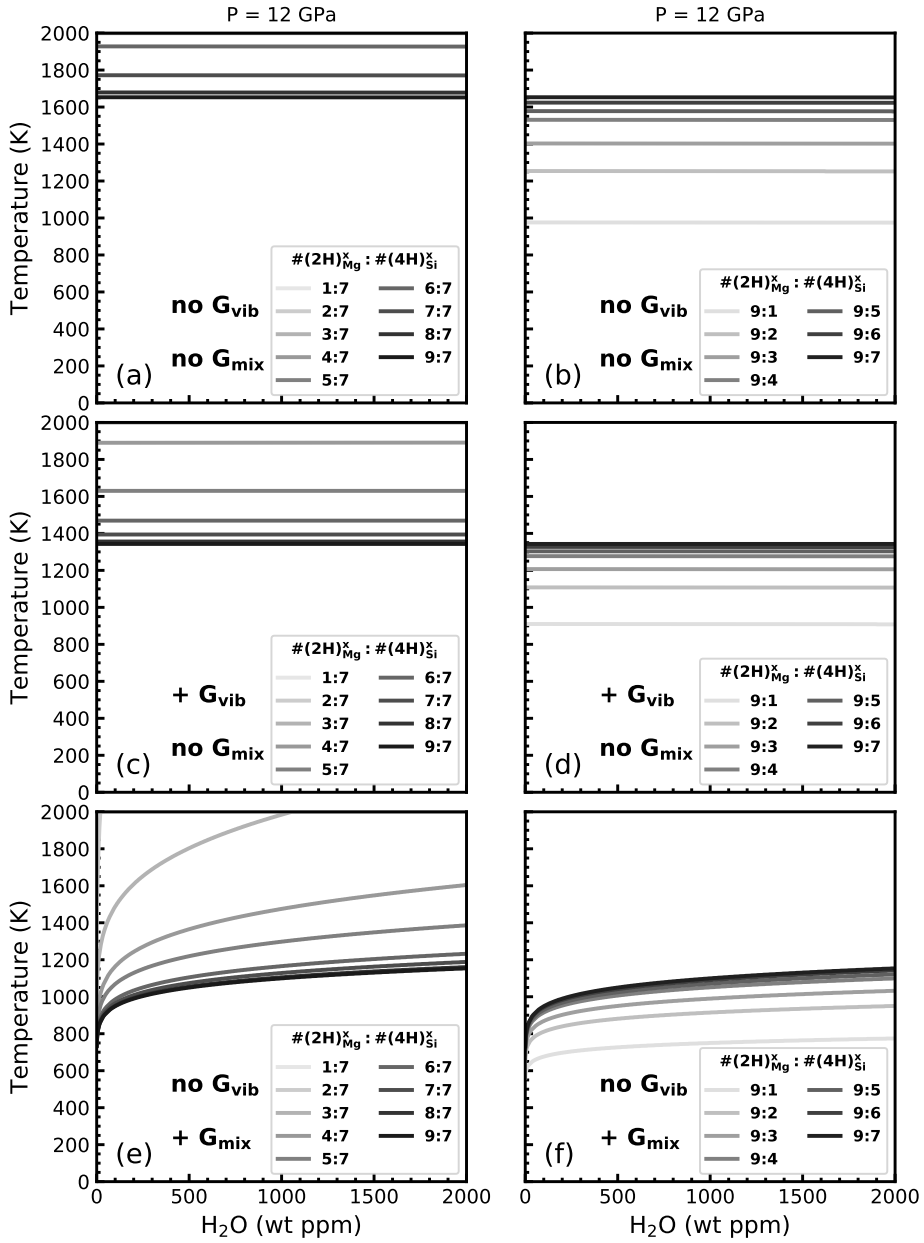

Figure 4.6: Plots of $\Delta G_{\mathrm{r}}^{GGA}(P,T) = 0$ (see equation (4.8)) at 12 GPa including different internal configuration energy contributions plotted parametrically in temperature–water content space. (a and b) exclude G_{vib} and G_{mix}, (c and d) include G_{vib} and exclude G_{mix}, (e and f) exclude G_{vib} and include G_{mix}. The ratio of the number of distinct configurations, $\#(\mathrm{2H})^{\mathrm{X}}_{\mathrm{Mg}}$:$\#(\mathrm{4H})^{\mathrm{X}}_{\mathrm{Si}}$, are shown in the legend.

Chapter 5

Fe isotope fractionation in Fe-bearing bridgmanite

Ab initio investigation of the Fe isotope fractionation between Fe-bearing bridgmanite and metallic hexagonal close-packed (HCP) Fe at core-mantle segregation condition (40–60GPa, 3000–4000K) revealed that the low-spin Fe in bridgmanite can enrich more heavy Fe isotopes. Consequently, this might cause the bulk silicate Earth (BSE) Fe isotopically heavier than chondrites by ~ 0.04 ‰ (in δ^{56}Fe). In contrast to the scenario on the Earth, the core of smaller planets like Mars and Vesta formed at a shallower depth and the Fe in the silicate phases is in the high spin state, therefore, no significant Fe isotope fractionation can be caused by the core formation process. Consequently, the core-mantle segregation process can explain the inconsistent observations of the Fe isotopic signature on Earth and on other smaller planets or chondrite.

5.1 Introduction

In the past decades, Fe isotopic abundances have been used to study the accretion and differentiation of Earth or to constrain the light elements in the core [28, 29, 30, 31, 44, 32, 33, 157, 34, 37, 38, 158, 43, 39]. Recent studies reveal that the Fe in terrestrial basalts are isotopically heavier than that of chondrites. For example, the mid-ocean ridge basalts (MORBs) enrich the heavy Fe isotope (^{56}Fe) by +0.1 ‰ relative to chondrites [40], while the basalts from Mars and Vesta have chondritic Fe isotopic composition

within uncertainty [44, 37].

There are different interpretations of these observations. Fe isotopes fractionate during the core-mantle segregation with more light Fe isotope going into the metallic core, leaving the remaining part of Earth isotopically heavier [32, 43]. However, some studies show that the Fe isotope will not fractionate between silicate and metal phase [159, 160]. In addition, the primordial Earth may evaporate more light Fe isotope during or after accretion [45, 31, 44]. Other studies proposed that the mantle has chondritic Fe isotopic composition [41, 37, 42], and the systematic elevated Fe isotopic composition of basalts actually originated in magmatic differentiation [161, 40].

Accurate Fe isotope fractionation factors among silicate phases and metal phases at core formation condition are required to determine whether the core formation process could fractionate the iron isotope in the Earth. Due to the inaccessibility of the core-mantle segregation event both physically and temporally, this can only be investigated experimentally and theoretically at the proposed conditions, or through meteorites samples. For example, a few studies measured the iron isotopic composition of separated olivine and metal phases from the pallasite [37, 162], or silicate phases and metallic phases (iron or iron alloy) at high pressures [159, 30, 160, 34, 39]. According to the basic idea of isotope fractionation within the harmonic model, any factor that can affect the chemical bond strength can alter the isotope ratio and cause the isotope fractionation. Normally, the isotope fractionation will be proportional to $1/T^2$ in the harmonic model, but if the temperature is too high, for example, near the melting point, then anharmonicity would be nonnegligible, and the isotope fractionation properties might be totally different. As the structure of the silicate phase might change with pressure, the isotope fractionation data derived from low pressure might be only suitable for studying small planets or asteroids but cannot be extrapolated to the core formation conditions of early Earth. In addition, Fe in bridgmanite (ABO_3 type silicate perovskite), the most voluminous mineral in the lower mantle, can be positioned in the A and B sites of bridgmanite and in different valence states, with Fe^{3+} in the B site undergoing spin crossover at lower mantle pressures [163, 46, 47]. Therefore, the effects of pressure, iron valence, spin states, and crystallographic site on iron isotope fractionation need to be clarified to investigate the isotopic fractionation between bridgmanite and metallic iron.

Recent studies revealed that Fe^{3+} could also be abundant Frost:2004. Therefore, the

$(Mg, Fe^{3+})(Si, Fe^{3+})O_3$ model is also included in this study. In addition, as the Fe^{3+} and Al can substitute for Mg and Si in the lower mantle [164, 165, 166], $(Mg, Fe^{3+})(Si, Al)O_3$ is also investigated. Together with the $(Mg, Fe^{2+})SiO_3$, the influence of the valence state, the crystallographic site, and spin state on the Fe isotope fractionation (and the average force constant $\langle F \rangle$) of Fe-bearing bridgmanite can be studied. Pure HCP iron is used to represent the metal phase during the core-mantle segregation process. Then the equilibrium Fe isotope fractionation factors among these phases are used to deduce the isotopic signature of the bulk silicate Earth.

5.2 Method and Calculation Details

5.2.1 Fe isotope nomenclature and the reduced partition function ratio (β factor)

Fe isotope fractionation in the literature has been reported either in the form of $^{56}Fe/^{54}Fe$ or $^{57}Fe/^{54}Fe$ relative to the standard metallic iron reference IRMM-14 in the notation δ^{56} Fe or δ^{57} Fe, which is defined as

$$\delta^{56}\mathrm{Fe} = \left[\frac{\left(^{56}\mathrm{Fe}/^{54}\mathrm{Fe}\right)_{\mathtt{sample}}}{\left(^{56}\mathrm{Fe}/^{54}\mathrm{Fe}\right)_{\mathtt{IRMM-014}}} - 1 \right] \times 10^3. \tag{5.1}$$

The δ^{57}Fe is also defined in a similar method and normally, $\delta^{57}\mathrm{Fe} \approx 1.475 \times \delta^{56}\mathrm{Fe}$ as only mass-dependent fractionation is expected. n this study, we report the Fe isotope fractionation in terms of the $^{56}Fe/^{54}Fe$ ratio. The equilibrium Fe isotope fractionation factor between phase A and phase B is given as the α notation.

$$10^3 \ln \alpha_{A-B} \approx \Delta^{56}\mathrm{Fe}_{\mathrm{A-B}} = \delta^{56}\,\mathrm{Fe}_{\mathrm{A}} - \delta^{56}\,\mathrm{Fe}_{\mathrm{B}} \tag{5.2}$$

If phase B is a perfect gas of element X, then the isotope fractionation factor is defined as the reduced partition function ratio or the β factor [69]. Therefore, $\alpha_{\mathrm{A-B}}$ can be calculated as $\alpha_{\mathrm{A-B}} = \beta_{\mathrm{A}}/\beta_{\mathrm{B}}$, and $\delta^{56}\mathrm{Fe}_{\mathrm{A}} - \delta^{56}\mathrm{Fe}_{\mathrm{B}} \approx 10^3 (\ln \beta_{\mathrm{A}} - \ln \beta_{\mathrm{B}})$. Here the β factor can be calculated by equation (2.71) described in chapter 2.

The reduced partition function ratios or the β factor also can be derived from the mean force constant of the iron bonds, $\langle F \rangle$, using NRIXS spectroscopy by $10^3 \ln \beta =$

$2904\frac{\langle F\rangle}{T^2}$ [167]. In this study, we report our isotope data in both $10^3 \ln\beta$ and $\langle F\rangle$ format in order to compare with previous studies.

5.2.2 DFT calculations

All calculations were performed using the local density approximation (LDA) augmented by the self- and structurally consistent Hubbard U_{sc} (LDA+U_{sc} method)[168, 169, 170] since standard DFT functionals do no capture strong correlation effects of 3d electrons properly. The pseudopotentials used here are the same as in the [171]. The plane-wave kinetic energy and charge density cut-off are 40 and 160 Ry, respectively. All calculations of Fe-bearing bridgmanite were performed in the 40-atoms supercells. One of the eight Mg^{2+} ions in A site is substituted by one Fe2+ ion to get $(Mg, Fe^{2+})SiO_3$; substituting a nearest-neighbor Mg2+−Si4+ pair by a Fe3+−Fe3+ or a Fe3+−Al pair to get $(Mg, Fe^{3+})(Si, Fe^{3+})O_3$ or $(Mg, Fe^{3+})(Si, Al)O_3$ [172, 171]. Electronic states were sampled on a shifted $2 \times 2 \times 2$ and $12 \times 12 \times 10$ k-point grid [173] for all modeled Fe-bearing bridgmanite and HCP iron, respectively.

The structures at a series of pressure were optimized using the variable cell-shape damped molecular dynamics [98, 99] prior to conducting any further calculations. Convergence threshold of the total energy and atomic force for ionic minimization were less than 10-6 Ry and 10-4 Ry/a.u, respectively. Phonons have been calculated for all the system using density functional perturbation theory (DFPT) [64] within the LDA+U functional [174]. Calculated force constants [175, 172, 171] and dynamical matrices sampled a regular q-point grid ($2 \times 2 \times 2$ for bridgmanite and $4 \times 4 \times 3$ for HCP iron) in the Brillouin Zone, then they were interpolated in a denser q-point grid ($8 \times 8 \times 8$ for bridgmanite and $20 \times 20 \times 20$ for HCP Fe) to obtain the vibrational density of states, the key element to obtain the reduced partition function ratio.

5.3 Results and Discussion

The calculated $10^3 \ln\beta_{^{56/54}Fe}$ of Fe isotope for all models at 60 GPa are plotted in figure 5.1. This is the suggested pressure of the core formation proceeded in the early Earth history [30, 34, 176, 177].

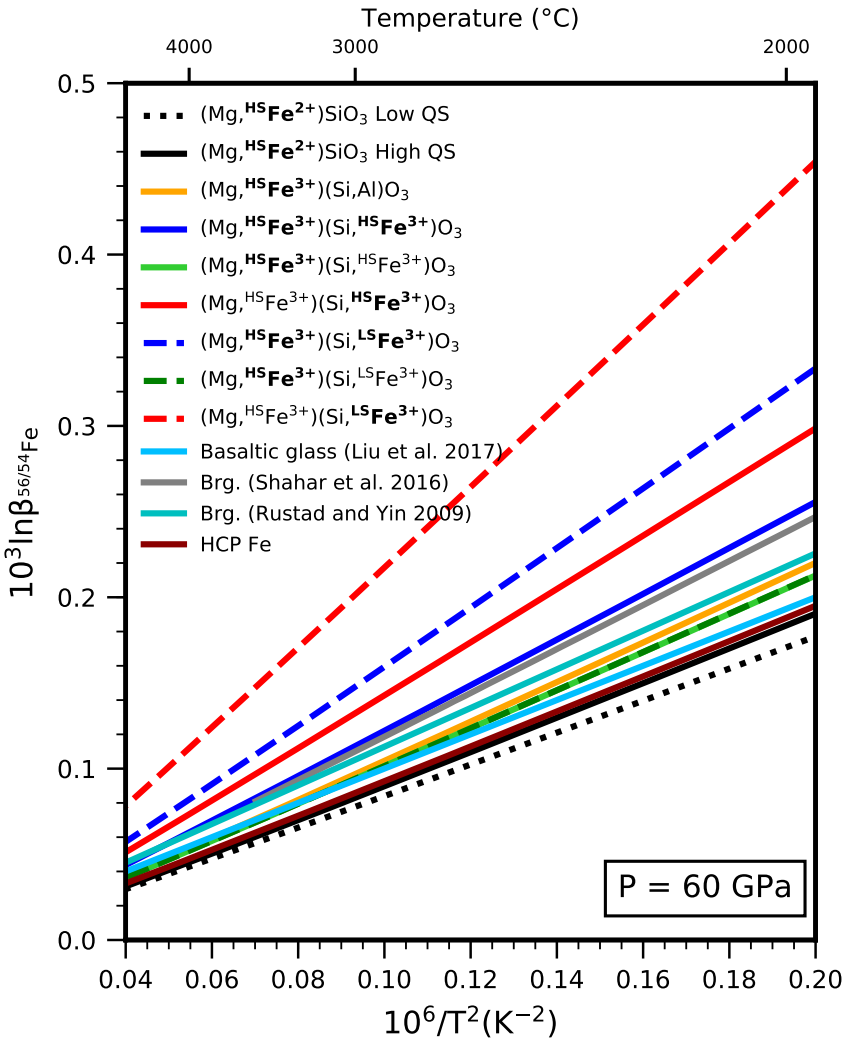

Figure 5.1: $10^3 \ln \beta_{56/54_{Fe}}$ of different configurations of Fe in bridgmanite and pure HCP Fe at 60 GPa, the typical pressure expected for core formation in early Earth. Spin states are denoted by HS (high spin) and LS (low spin). Low and high quadrupole splitting (QS) states are marked with low and high QS, respectively. The selected site considered for Fe isotope fractionation is represented by bold fonts. Comparison with bridgmanite [34] and basaltic glass [30] are also shown here.

The isotope fractionation properties of Fe in A and B sites are investigated separately, the investigated Fe site is marked in bold font in the chemical formula. For example, $(Mg, {}^{\mathbf{HS}}\mathbf{Fe^{2+}})SiO_3$ (the superscripts HS or LS on the left side of Fe cation means the high or low spin state) indicates the Fe in the A site is addressed, while $(Mg, {}^{\mathbf{HS}}\mathbf{Fe^{3+}})(Si, {}^{HS}Fe^{3+})O_3$ and $(Mg, {}^{HS}Fe^{3+})(Si, {}^{\mathbf{LS}}\mathbf{Fe^{3+}})O_3$ indicates that the Fe in A and B sites are addressed separately. However, the measurement of Fe isotope cannot distinguish the substitutional Fe in the A or B site, thus the Fe isotope fractionation in A and B sites should be considered simultaneously if they both exist, which is corresponding to the isotope fractionation of $(Mg, {}^{\mathbf{HS}}\mathbf{Fe^{3+}})(Si, {}^{\mathbf{HS/LS}}\mathbf{Fe^{3+}})O_3$. Or the Fe isotope fractionation properties can be estimated by using the weighted average among $(Mg, {}^{\mathbf{HS}}\mathbf{Fe^{3+}})(Si, {}^{HS/LS}Fe^{3+})O_3$ and $(Mg, {}^{HS}Fe^{3+})(Si, {}^{\mathbf{HS/LS}}\mathbf{Fe^{3+}})O_3$ if the percentages of Fe in A site and B site and the spin state are known. The ^{56}Fe-enrichment order in bridgmanite follows the sequence: Fe^{2+} in A site $<$ Fe^{3+} in A site $<$ high spin Fe^{3+} in B site $<$ low spin Fe^{3+} in B site.

The $10^3 \ln \beta_{^{56/54}Fe}$ of pure HCP iron is also shown in figure 5.1, which shows negligible Fe isotope fractionation from $(Mg, {}^{\mathbf{HS}}\mathbf{Fe^{2+}})SiO_3$. The relationship between the bond lengths and $10^3 \ln \beta_{^{56/54}Fe}$ are shown in figure 5.2. Also, the pressure-depended force constants for Fe-bearing bridgmanite and HCP iron are shown in figure 5.3. The calculated force constant of metal iron agrees with the experimental results from Liu et al. [30] within the uncertainties of the measurement validate the accuracy of the calculations. The force constant is monotonically increased with pressure for all phases, and the relationship between $\langle F \rangle$ and P were fitted quadratically and listed in table 5.1, from which the force constant and the beta factor for all phases can be calculated.

5.4 Discussion

5.4.1 Effect of valence state of Fe in bridgmanite

The $10^3 \ln \beta_{^{56/54}Fe}$ of $(Mg, {}^{\mathbf{HS}}\mathbf{Fe^{2+}})SiO_3$ in either high or low quadrupole splitting (QS) and $(Mg, {}^{\mathbf{HS}}\mathbf{Fe^{3+}})(Si, Al)O_3$ show that Fe^{3+} tends to host more heavier isotopes than Fe^{2+} in the A site. This is consistent with previous studies for other multi-valence cations, for example, V^{5+} enrich heavier vanadium isotopes than the V^{3+} in the solution condition[178]. This is expected based on the understanding that sites having smaller

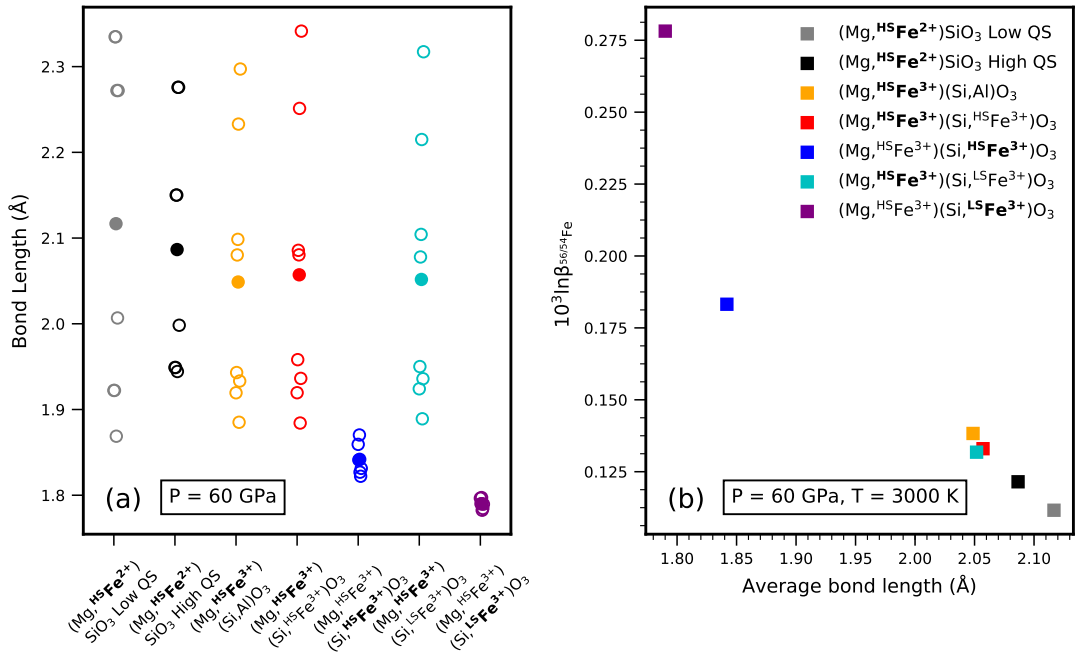

Figure 5.2: (a) The Fe-O bond lengths and the average bond length of each Fe in the Fe-bearing bridgmanite, the selected site considered for Fe-O bond length is represented by bold fonts, for example, the (Mg, $^{\mathbf{HS}}\mathbf{Fe}^{3+}$)(Si, $^{\mathrm{HS/LS}}\mathrm{Fe}^{3+}$)$\mathrm{O}_3$ and (Mg, $^{\mathrm{HS}}\mathrm{Fe}^{3+}$)(Si, $^{\mathbf{HS/LS}}\mathbf{Fe}^{3+}$)$\mathrm{O}_3$ represent the average Fe-O bond lengths in A site and B site, respectively. The solid circle denotes the average bond length of each system. (b) The beta factor versus average bond length of all modeled Fe-bearing bridgmanite at 60 GPa and 3000 K.

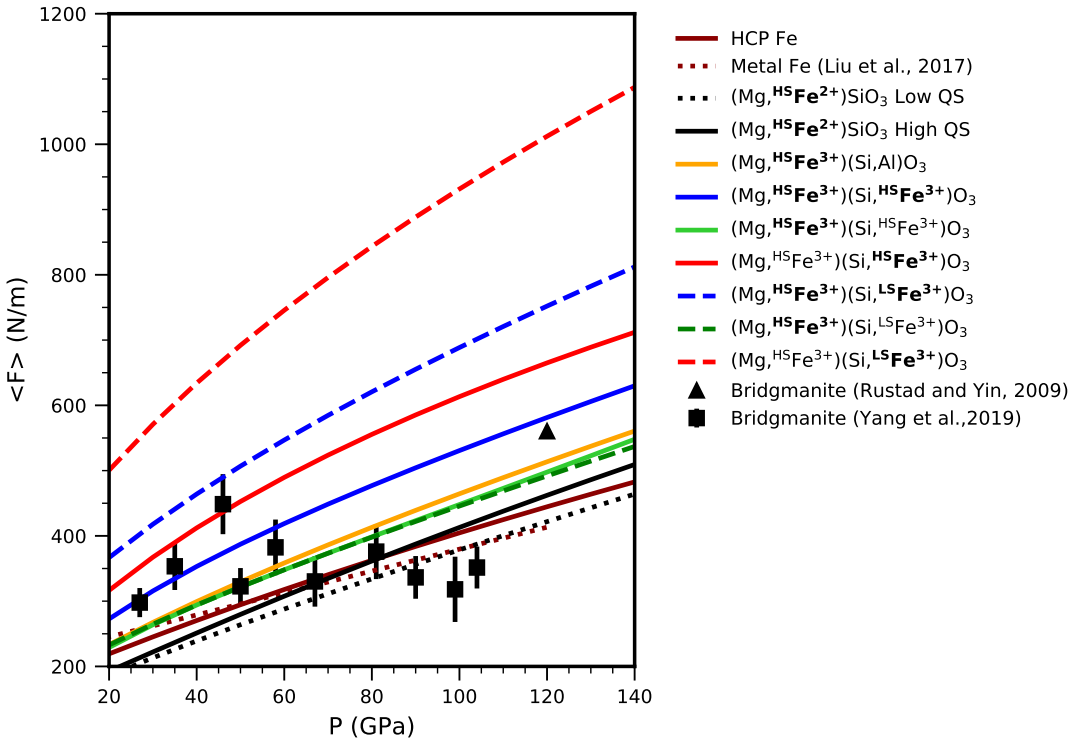

Figure 5.3: The averaged force constant $\langle F \rangle$ of the Fe-bearing bridgmanite and HCP Fe versus pressure, and the comparison with the recent measured result from Liu et al. [30] and Yang et al. [39] and the calculated result from Rustad and Yin[33].

Table 5.1: Pressure dependence of the force constant $\langle F \rangle$ values of Fe-bearing bridgmanite and HCP Fe. The relationship between the force constant $\langle F \rangle$ (unit in N/m) and pressure P (unit in GPa) were described as $\langle F \rangle = a \times P^2 + b \times P + c$, the valid pressure range is between 20 – 40 GPa.

Phase	a	b	c
$(Mg, {}^{\mathbf{HS}}\mathbf{Fe^{2+}})SiO_3$ high QS	-0.002842	3.070993	140.518891
$(Mg, {}^{\mathbf{HS}}\mathbf{Fe^{2+}})SiO_3$ low QS	-0.002335	2.652545	142.482044
$(Mg, {}^{\mathbf{HS}}\mathbf{Fe^{3+}})(Si, Al)O_3$	-0.004168	3.335824	179.505546
$(Mg, {}^{\mathbf{HS}}\mathbf{Fe^{3+}})(Si, {}^{\mathbf{HS}}\mathbf{Fe^{3+}})O_3$	-0.006397	3.888531	213.951361
$(Mg, {}^{\mathbf{HS}}\mathbf{Fe^{3+}})(Si, {}^{HS}Fe^{3+})O_3$	-0.002108	2.914729	185.397171
$(Mg, {}^{HS}Fe^{3+})(Si, {}^{\mathbf{HS}}\mathbf{Fe^{3+}})O_3$	-0.010685	4.862300	242.507287
$(Mg, {}^{\mathbf{HS}}\mathbf{Fe^{3+}})(Si, {}^{\mathbf{LS}}\mathbf{Fe^{3+}})O_3$	-0.008089	4.886690	290.271265
$(Mg, {}^{\mathbf{HS}}\mathbf{Fe^{3+}})(Si, {}^{LS}Fe^{3+})O_3$	-0.003291	3.001019	185.103635
$(Mg, {}^{HS}Fe^{3+})(Si, {}^{\mathbf{LS}}\mathbf{Fe^{3+}})O_3$	-0.012888	6.772426	395.438021
HCP Fe	-0.003119	2.662175	175.181727

average nearest neighbor distances (n.n.d.) produce larger isotope ratios [179, 180, 178, 181]. This also can be explained as "smaller sites" are less favored by isotopic lighter ions with larger vibrational amplitudes. As shown in figure 5.2(a), the average $Fe^{3+}-O$ distance (2.05 Å for the Fe in A site, 1.84 Å for the HS Fe in the B site and 1.79 Å for the LS Fe in the B site at 60 GPa) is shorter than the $Fe^{2+}-O$ distance (2.07 Å for the high QS $(Mg, {}^{\mathbf{HS}}\mathbf{Fe^{2+}})SiO_3$ and 2.12 Å for the low QS $(Mg, {}^{\mathbf{HS}}\mathbf{Fe^{2+}})SiO_3$ at 60GPa). The Fe^{3+}-bearing bridgmanite enriches more heavy isotopes than the Fe^{2+}-bearing bridgmanite, which shown in figure 5.2(b).

5.4.2 Effect of the crystallographic site in bridgmanite

The $10^3 \ln \beta_{56/54_{Fe}}$ of $(Mg, {}^{\mathbf{HS}}\mathbf{Fe^{3+}})(Si, {}^{HS}Fe^{3+})O_3$ and $(Mg, {}^{HS}Fe^{3+})(Si, {}^{\mathbf{HS}}\mathbf{Fe^{3+}})O_3$ in figure 5.1 and figure 5.2(b) show that the Fe^{3+} in the B site enriches heavy Fe isotopes compared to the Fe^{3+} in the A site. The $10^3 \ln \beta_{56/54_{Fe}}$ of $(Mg, {}^{\mathbf{HS}}\mathbf{Fe^{3+}})(Si, {}^{HS}Fe^{3+})O_3$ and $(Mg, {}^{\mathbf{HS}}\mathbf{Fe^{3+}})(Si, {}^{LS}Fe^{3+})O_3$ are undistinguishable, and both of them are very close to that of $(Mg, {}^{\mathbf{HS}}\mathbf{Fe^{3+}})(Si, Al)O_3$ showing that cations in the B site have limited influence on the fractionation properties of Fe in the A site. In addition, the average $Fe^{3+}-O$ bond length in the A site is very similar in all of the Fe-bearing bridgmanite models, but all are significantly larger than these in B site as shown in figure 5.2.

5.4.3 Effect of the spin state of Fe in bridgmanite

In Fe-bearing bridgmanite, Fe in the A site remains in the high spin (HS) state through the whole mantle pressure range, while Fe^{3+} in the B site undergoes spin crossover to the low spin (LS) state between 40-70 GPa [163, 46, 47, 171, 182, 183]. And the B site shrinks while this spin transition occurs. The β factors of $(Mg, {}^{HS}Fe^{3+})(Si, \mathbf{{}^{HS}Fe^{3+}})O_3$ and $(Mg, {}^{HS}Fe^{3+})(Si, \mathbf{{}^{LS}Fe^{3+}})O_3$ show that the spin state does affect the Fe isotope fractionation. Low spin Fe is richer in ^{56}Fe than high spin Fe. The rational for such influence is similar to that of valence and site. Low spin Fe^{3+} has shorter average Fe−O distances than high spin Fe^{3+} (see figure 5.2). This happens because low spin Fe has all five 3d electrons in the t2g orbitals pointing away from oxygen ions, while high spin Fe has two of the 3d electrons in the eg orbitals pointing toward the nearest oxygen ions, which increases the Fe-O distances .

In reality, Fe in the B site transforms from the high spin to the low spin state between 40 and 70 GPa[163, 46, 47, 183, 171, 182], so the β factor could shift from $(Mg, \mathbf{{}^{HS}Fe^{2+/3+}})(Si, Al, {}^{HS}Fe^{3+})O_3$ values to $(Mg, {}^{HS}Fe^{3+})(Si, \mathbf{{}^{LS}Fe^{3+}})O_3$ values proportionally to the fraction of iron in the B sites and spin state.

The β factors of $(Mg, \mathbf{{}^{HS}Fe^{2+}})SiO_3$ and $(Mg, \mathbf{{}^{HS}Fe^{3+}})(Si, Al)O_3$ are similar to the recent experimental data on basaltic glass at 60 GPa [30], which might demonstrate that Fe in basaltic glass in that experiment was in the high spin state and in the A-like (large) site. The calculated β factor of Fe-bearing bridgmanite at 60 GPa in Shahar et al.,[34] is slightly larger than that of $(Mg, \mathbf{{}^{HS}Fe^{2+}})SiO_3$ in our study for some unclear reason.

5.4.4 Effect of iron position in the A site of bridgmanite

Mössbauer quadrupole splitting (QS) experiments on Fe-bearing bridgmanite identified a transition from a low QS (LQS) to a high QS (HQS) [184, 185], suggesting the possibility of an intermediate spin state with S=1 [186, 187]. However, ab initio calculations showed that two HS states with different QS are possible in bridgmanite [188]. These states have HS Fe^{2+} in slightly different sites with different d-orbital occupancies, which produces different Mössbauer QS, one low and one high, as observed experimentally. Thus, the LQS-HQS transition corresponds to a change in atomic position of Fe, as shown in the

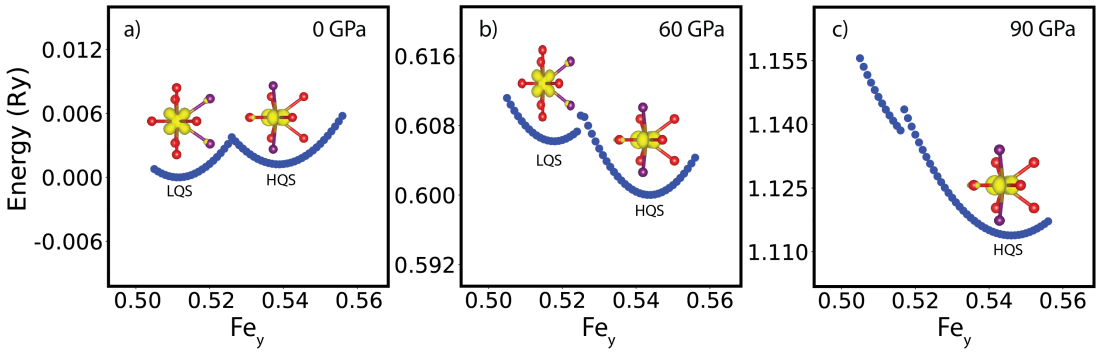

Figure 5.4: Energy as a function of y coordinate of iron in (Mg, $^{\mathbf{HS}}\mathbf{Fe}^{\mathbf{2}+}$)$SiO_3$ perovskite. The two minima at P = 0 and 60 GPa correspond to two stable positions, both with Fe^{2+} (with 3d6 configuration) in the HS state (S=2). Insets show the electronic charge density of the "spin down" electron in each stable position. These states have distinct iron Mössbauer quadrupole splitting. At 90 GPa only one of the positions is stable, corresponding to the HQS state. Purple spheres indicate oxygen atoms with the longest bond length.

figure 5.4. The minimum around 0.51 corresponds to the LQS, while the one around 0.54 corresponds to the HQS state, [188]. The effect of different QS states is also investigated here. The calculated Fe isotope fractionation signature of low QS and high QS states in (Mg, $^{\mathbf{HS}}\mathbf{Fe}^{\mathbf{2}+}$)$SiO_3$ are similar, particularly in the high-temperature range, as shown in figure 5.1.

The difference between the force constant obtained in recent measurements of Fe-bearing bridgmanite and those computed here are shown in figure 5.3. As shown in Yang et al., [39], the averaged force constant of bridgmanite increased with pressure up to 45 GPa, then it dropped and remains constant within the accuracy above 60 GPa. The reason behind this behavior remains unclear, but this might be caused by the highly anharmonic nature of this double well structure. The consequence of this effect is the average force constant of Fe is smaller than either the pure low QS or high QS state.

To sum up, the Fe isotope fractionation properties in Fe-bearing bridgmanite are influenced by valence, site, and spin state, which are related to the Fe incorporation mechanism in bridgmanite, as well as pressure.

5.4.5 The implication of Fe isotope fractionation during core formation in planets

The iron isotope fractionation between core and mantle during core formation has been extensively studied to understand the iron isotopic composition of the Earth. The enigmatic condition of core formation is constrained to be 50 GPa (not greater than 60GPa) [176]. The Fe isotopic composition of Earth's mantle can be calculated using the isotope mass balance relationship [29]:

$$\begin{aligned}\delta^{56}\mathrm{Fe_{BE}} &= \delta^{56}\mathrm{Fe_{Mantle}} \times f\mathrm{Fe_{Mantle}} + \delta^{56}\mathrm{Fe_{Core}} \times f\mathrm{Fe_{core}} \\ &= \delta^{56}\mathrm{Fe_{Mantle}} \times f\mathrm{Fe_{Mantle}} + (\delta^{56}\mathrm{Fe_{BSE}} - \Delta^{56}\mathrm{Fe_{Mantle-Core}}) \times (1 - f\mathrm{Fe_{Mantle}})\end{aligned} \tag{5.3}$$

where $\delta^{56}\mathrm{Fe_{BE}}$ is the Fe isotopic composition of bulk Earth, generally assumed to have the chondritic value (0‰). The fFe is the mass fraction of Fe in mantle or core, and the $f\mathrm{Fe_{Mantle}}$ is set to 0.161 according to McDonough[189]. As the Fe isotope fractionation between different Fe phases and the Fe alloy with light elements are typically very small [30, 34], pure HCP iron is used to represent the metal phase during the core-mantle segregation in the Earth. $\Delta^{56}\mathrm{Fe_{Mantle-Core}}$ is the isotope fractionation factor among different Fe-bearing bridgmanite models and the HCP iron.

The simulated Fe isotopic compositions of Bulk Silicate Earth (BSE) with different types of bridgmanite are shown in figure 5.5. The 60 GPa results are shown in solid/dash lines, and the 40 GPa (lower boundary) and 60 GPa (upper boundary) results are also shown in shade area as references. Figure 5.5 shows clearly that the occupation site and spin states of Fe in bridgmanite affect the isotopic composition of the mantle in our model. The overlap of the estimated Fe isotopic composition of BSE [41, 36] and model prediction in figure 5.5 show the evaluated Fe isotopic composition of Earth's upper mantle can be caused by core segregation at ∼40-60 GPa, 3000-4000 K, which is the proposed core-mantle segregation condition. To be more specific, Fe in the B site of bridgmanite, $((\mathrm{Mg},{}^{\mathrm{HS}}\mathrm{Fe}^{3+})(\mathrm{Si},{}^{\mathbf{HS}}\mathbf{Fe}^{\mathbf{3}+})\mathrm{O}_3)$, or mixture of Fe in low spin in the B site and Fe in the A site $((\mathrm{Mg},{}^{\mathbf{HS}}\mathbf{Fe}^{\mathbf{3}+})(\mathrm{Si},{}^{\mathbf{LS}}\mathbf{Fe}^{\mathbf{3}+})\mathrm{O}_3)$ can cause the elevated BSE value.

To further constrain the Fe isotope composition of the BSE, the proportions of the Fe in each site and spin state are required. Recent theoretical results indicated that

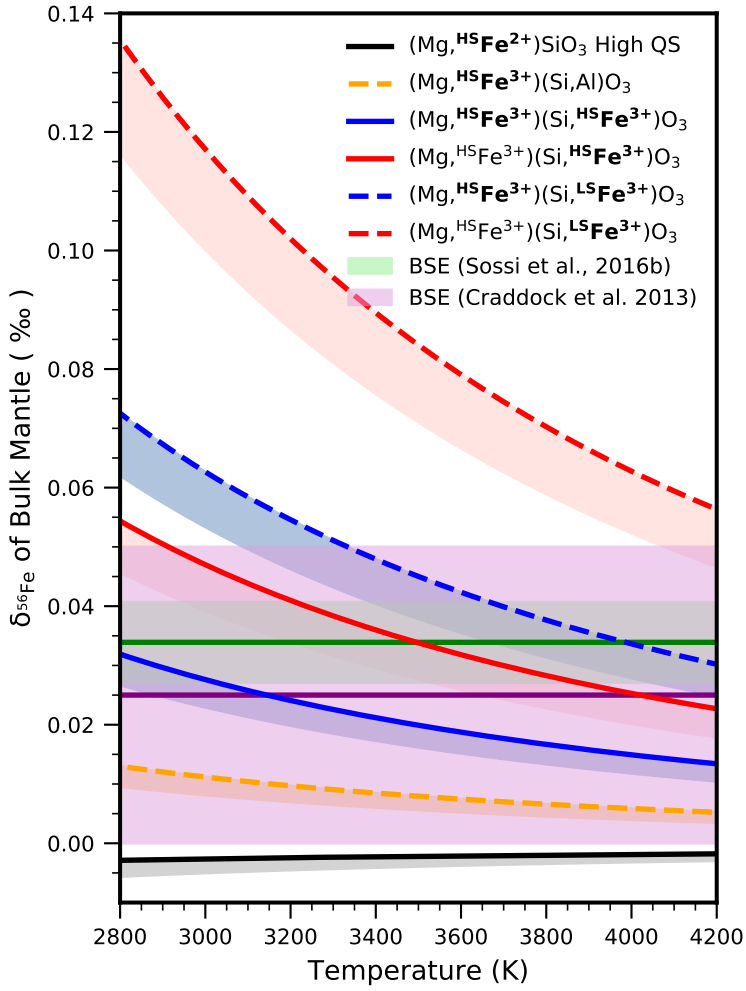

Figure 5.5: The range in Fe isotopic compositions of bulk mantle predicted from core segregation with different bridgmanite models at 60 GPa. The shaded area below the line shows the range of the simulated Fe isotopic composition for each model, which corresponding to the conditions at 40GPa (lower boundary), and 60 GPa (upper boundary) respectively. The light green or purple field is the estimated range for Bulk Silicate Earth based on Sossi et al.,[36] and Craddock et al.,[41], respectively.

about 1/4 Fe would be in low spin state at the proposed core formation condition [171]. Then the estimated Fe isotope composition of BSE will be 0.043‰ if all Fe^{3+} are in the B site, and 0.026‰ if the Fe^{3+} is equally split into A and B site. As Fe should also go into ferropericlase, according to recently published experimental force constant, ferropericlase also enriches heavy Fe isotopes compared to metal phase [39]. Therefore, the Fe isotope composition of the BSE can be even higher. In addition, as stated by Fujino et al. [164, 165], Fe^{3+} could replace Al in the B site and become low spin between 50-70 GPa. Then, the iron isotope would fractionate even further between the mantle and core phase. According to these assumptions, the core-mantle segregation on the Earth would elevate the Fe isotope signature of BSE to a distinguishable value compared with the average Fe isotope composition of chondrites.

For planets whose core formation occurs at a shallow depth, for example, Mars and Vesta, Fe in the silicate phases are in the high spin states, and the absence of Fe^{3+} in their samples implies that the majority of Fe in Mars and Vesta mantle must be in Fe^{2+} state [35, 36, 190] and high spin states during the core forming. The discussion above show that Fe isotope fractionation between high spin Fe-bearing silicate minerals/rocks and metal iron are very small and cannot cause large Fe isotope fractionation between silicate part during the core-mantle segregation process. Therefore, the core formation process in the Earth can cause the elevated Fe isotopic composition of the mantle but not in Mars or Vesta.

Chapter 6

The Si isotope evidence show Earth might be non-chondritic

Ab initio investigation of the isotope fractionation between bridgmanite and Fe-Si alloy at the mantle pressure range (20-140 GPa) reveals that the silicon isotope fractionates between the silicon and the metallic phases. The consequence of core-mantle segregation has also been studied by deriving the isotope composition of the bulk Earth (BE) or bulk silicate Earth (BSE) from the calculated silicon fractionation factor and the natural observations from recent literature. It turns that the Earth might be non-chondritic for silicon isotope.

6.1 Introduction

Iron and silicon are two of the major elements on the Earth, and they exist from the silicate surface to the metallic core in many different forms. For decades, the iron and silicon isotopes have been used to study the early histories of accretion and differentiation in the Earth and other planets in the solar system [28, 30, 31, 32, 33, 34, 37, 42, 39], and the elemental and isotopic composition of the Earth, such as constrain the possible light elements in the core[191, 34].

Recent studies reveal that the iron [40] and silicon [192] in terrestrial basalts ($\delta^{56}\,\mathrm{Fe}_{\mathrm{basalts}} = +\,0.1\,‰$ and $\delta^{30}\,\mathrm{Si}_{\mathrm{basalts}} = -\,0.29\,‰$) are isotopically heavier than that of chondrites (CI chondrites, $\delta^{56}\,\mathrm{Fe}_{\mathrm{chondrite}} = 0.0\,‰$ and $\delta^{30}\,\mathrm{Si}_{\mathrm{chondrite}} = -\,0.44\,‰$). This

could reflect the equilibrium isotope fractionation among silicate and metal phases during core-mantle segregation [32, 43], our recent study on iron isotope fractionation between Fe-bearing bridgmanite and HCP iron suggests that core formation can cause the mantle heavier in iron isotope (chapter 5), other interpretations include evaporation of light elements into space during the accretion [31, 44] or partial melting extract heavy isotopes out of the mantle [41, 37, 42], a more recent study indicates that silicon isotope can fractionate during the nebular processes [45].

Isotope fractionation occurs among phases with different chemical bonding environments [74, 180, 181] and the bond strength affects the isotope fractionation. Normally, the phase with stronger bond enriches more heavy isotopes. Therefore, isotopes fractionate among phases with cations in different bond environments, such as different valence, spin states, and the coordination number (CN) of cations. Since pressure affects spin states for iron and structural environments for silicon, the iron and silicon isotope fractionation data obtained at low pressure among silicate and metallic phases might not be extrapolated to the high-pressure range.

Silicon has a single valence state (Si^{4+}) on the Earth's mantle, but the structural environment of silicon changes drastically from the upper mantle (CN=4) to the lower mantle (CN=6), recent study has already showed that the silicon isotope can fractionate between the upper and lower mantle mainly due to this structure change [191]. Thus, the silicon isotopic composition of the upper mantle might not be used to represent the whole mantle. In addition, silicon in the core is alloyed with iron, and its valence is different compared with the silicon in the silicate phases. According to the fundamental ideas of isotope fractionation, all these would affect the silicon isotope fractionation. Recent measurements of the silicon isotope fractionation factor at low pressure ($\sim$ 1 GPa) between silicate and metal might not be used to study the event occurred in the high-pressure range, such as core-mantle segregation; besides, the derived isotope fractionation factors are inconsistent. For example, the prefactor, A, in the $\Delta^{30}\mathrm{Si}_{(\mathrm{silicate-metal})} = \mathrm{A} \times 10^{6}/\mathrm{T}^2$ ranges from 8.04 to 4.42 [193, 194, 195, 196]. Therefore, the silicon isotope fractionation behavior among silicate and metallic phases at high-pressure range needs further investigation to study the isotopic composition or the differentiation history of the Earth.

In this study, we investigated the silicon isotope fractionation between bridgmanite

and the Fe-Si alloy at a range of pressures and focus on core-mantle segregation condition specifically. We checked the effect of core-mantle segregation on the iron and silicon isotope fractionation simultaneously. Furthermore, a layered model is adopted to constrain the silicon isotopic composition of the lower mantle as well as that of the bulk silicate Earth (BSE) with the silicon content in the core.

6.2 Method and Calculation Details

6.2.1 Reduced partition function ratio, β factor

The silicon isotope fractionation is normally reported in the $^{30}Si/^{28}Si$ ratio with the standard NBS-28 in the notation δ^{30} Si. See definition below:

$$\delta^{30}\mathrm{Si} = \left[\frac{(^{30}\mathrm{Si}/^{28}\mathrm{Si})_{\mathrm{sample}}}{(^{30}\mathrm{Si}/^{28}\mathrm{Si})_{\mathrm{standard}}} - 1\right] \times 10^3 \tag{6.1}$$

The equilibrium Fe isotope fractionation between phase A and phase B is given in the α notation

$$10^3 \ln \alpha_{A-B} \approx \Delta^{30}\mathrm{Si}_{\mathrm{A-B}} = \delta^{30}\,\mathrm{Si}_{\mathrm{A}} - \delta^{30}\,\mathrm{Si}_{\mathrm{B}} \tag{6.2}$$

$\alpha_{\mathrm{A-B}}$ (defined as the ratio of isotope ratios in phase A and B:$\alpha_{\mathrm{A-B}} = \mathrm{R_A}/\mathrm{R_B}$) is called the isotope fractionation factor between phase A and phase B. If phase B is the X element, the isotope fractionation factor is defined as the reduced partition function ratio β [69]. Therefore, $\alpha_{\mathrm{A-B}}$ can be represented as $\alpha_{\mathrm{A-B}} = \beta_{\mathrm{A}}/\beta_{\mathrm{B}}$, and $\delta^{30}\mathrm{Si_A} - \delta^{30}\mathrm{Si_B} \approx 10^3\,(\ln\beta_{\mathrm{A}} - \ln\beta_{\mathrm{B}})$. Here the β factor can be calculated by equation (2.71) described in chapter 2.

6.2.2 DFT calculations

All calculations were performed using the local density approximation (LDA) augmented by the self- and structurally consistent Hubbard Usc (LDA+Usc method) [168, 169, 170] since standard DFT functionals do no capture strong correlation effects of 3d electrons properly. The pseudopotentials used here are the same as in [171]. The plane-wave kinetic energy and charge density cut-off are 80 Ry and 800 Ry, respectively. The Fe-Si alloy is modeled in a 16-atom supercell with the Si/Fe = 1/15. Electronic states were all

sampled on a shifted $4 \times 4 \times 4$ k-point grid [173]. The structure at arbitrary pressure was optimized using variable cell-shape damped molecular dynamics [98, 99] for pressure relaxation before conducting any further calculations. Total energy, residual atomic forces were less than 10^{-6} Ry, 10^{-5} Ry/a.u, respectively. Phonons have been calculated for all the system using density functional perturbation theory (DFTP) [64] within the LDA+U functional [174]. Calculated force constants and dynamical matrices sampled a regular $2 \times 2 \times 2$ q-point grid in the Brillouin Zone. Then they were interpolated in a denser q-point grid to obtain the vibrational density of states ($12 \times 12 \times 12$ for Fe-Si alloy), the key element to obtain the reduced partition function ratio, β, as in the equation (2.71). All the calculations are performed in the Quantum Espresso package [95, 94]

6.3 Results

The β factor of silicon of all phases studied at 60 GPa are shown in figure 6.1. The silicon isotope beta factor sometimes is reported with the prefactor A in the equation $10^{3} \ln \beta_{\mathrm{Si}} = \mathrm{A} \times 10^{6} / \mathrm{T}^{2}$. Here, the dependence of A for the silicon isotope fractionation with pressure is plotted, and the comparison with experimental results is shown in figure 6.2, respectively. The relationship between A and pressure is fitted for silicon isotopes and is shown in table 6.1.

Table 6.1: Fitted parameters for $A = a \times P^2 + b \times P + c$. The valid pressure range is between 20 – 140 GPa.

Phase	a	b	c
(Mg, $^{\mathrm{HS}}Fe^{2+}$)SiO_3 High QS	-0.000073	0.048605	4.227072
(Mg, $^{\mathrm{HS}}Fe^{2+}$)SiO_3 Low QS	-0.000074	0.048731	4.226928
(Mg, $^{\mathrm{HS}}Fe^{3+}$)(Si, Al)O_3	-0.000073	0.048139	4.239752
(Mg, $^{\mathrm{HS}}Fe^{3+}$)(Si, $^{\mathrm{HS}}Fe^{3+}$)O_3	-0.000080	0.048186	4.100707
(Mg, $^{\mathrm{HS}}Fe^{3+}$)(Si, $^{\mathrm{LS}}Fe^{3+}$)O_3	-0.000073	0.047843	4.140838
$Fe_{15}Si$	-0.000022	0.021434	2.022159

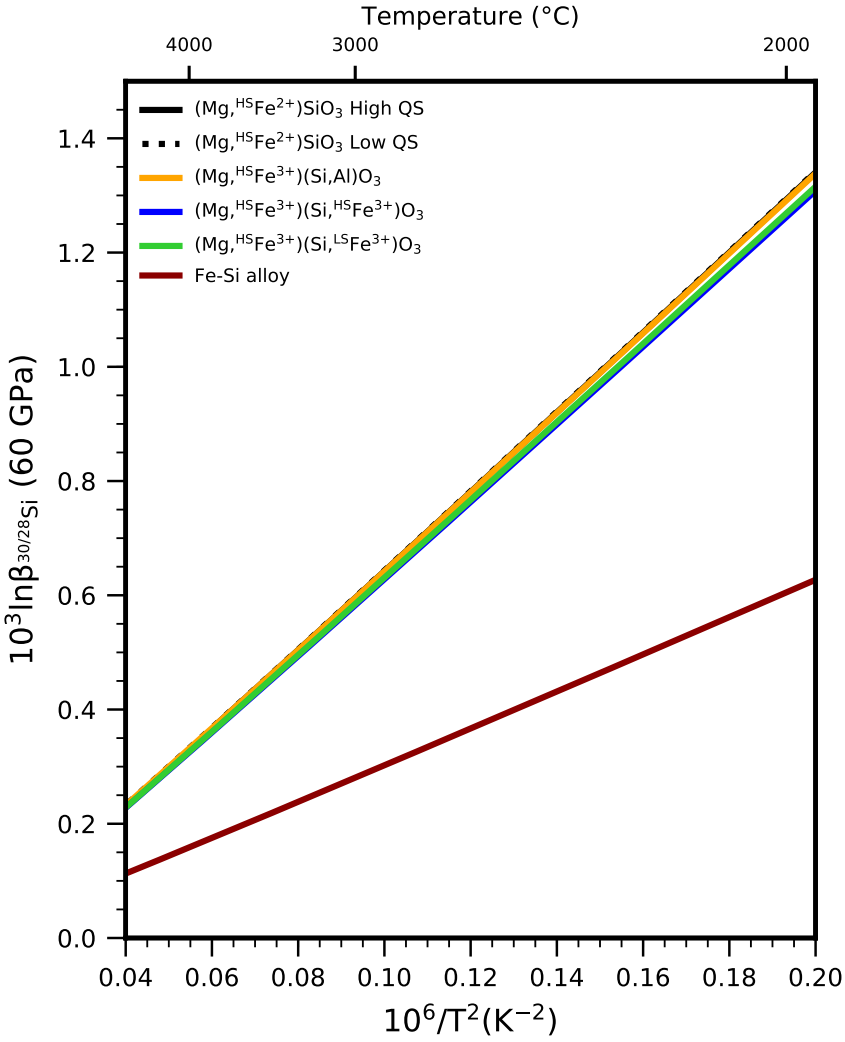

Figure 6.1: The dependence of calculated Si isotope β factor versus temperature. All the Fe-bearing bridgmanite have similar Fe isotope compositions, but all contain more heavy Fe isotope than the FeSi alloy.

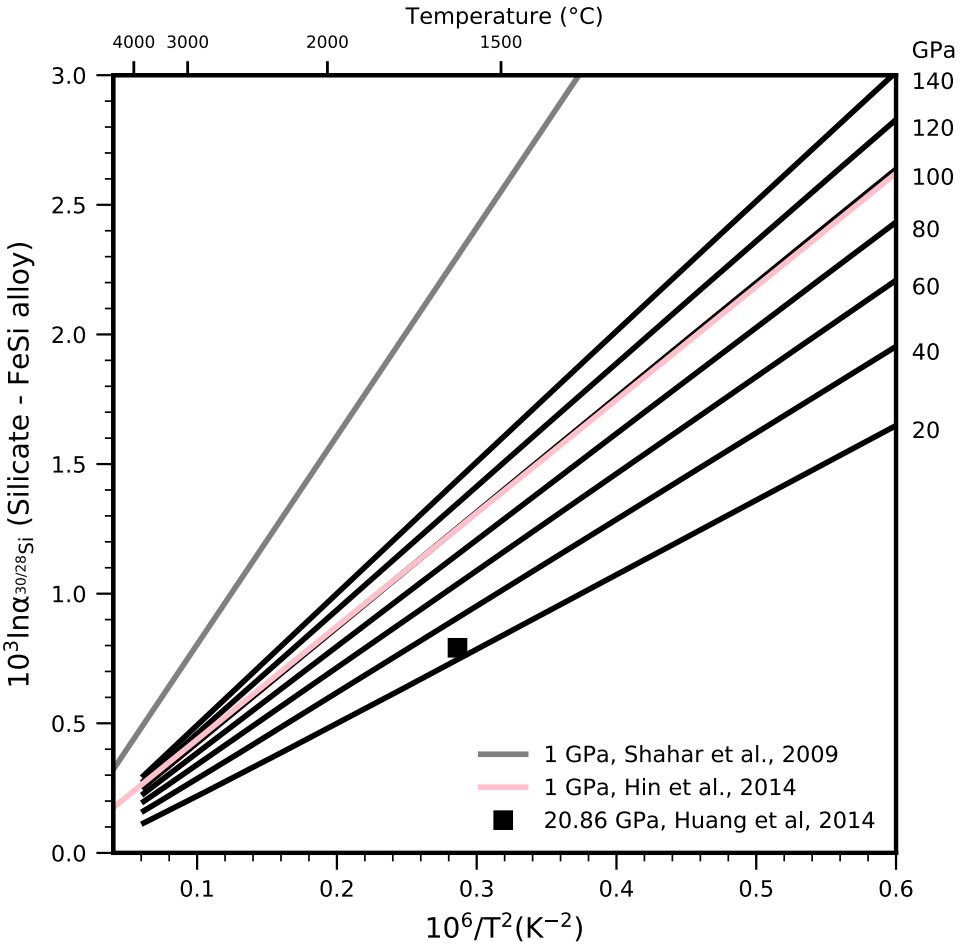

Figure 6.2: Pressure dependent silicon isotope factor $10^3 \ln \alpha$ between bridgmanite and FeSi alloy. The silicate phases from Shahar and Hin et al. (2014) are low pressure phase. 20.86 GPa data point from Huang et al. (2014) is from an ab initio calculation.

6.4 Discussion and implication

6.4.1 Si isotope fractionation between bridgmanite and Fe-Si alloy

Different models of bridgmanite show limited fractionation on the silicon isotope in the high-temperature range, but all significantly enrich heavy silicon isotope compared to the FeSi alloy as shown in figure 6.1. The recently determined silicon isotope fractionation factor between silicate and metallic phases at low pressure are significantly larger than the calculated isotope fractionation factor between bridgmanite and FeSi alloy at 60 GPa (see figure 6.2), where the core and mantle are believed to segregate [176]. For example, the isotope fractionation factor derived by Shahar et al.[194] is much higher than the calculated isotope fractionation factor between bridgmanite and the metallic phase. Even the silicon isotope fractionation factor derived from Hin et al. [193] is much smaller than values in Shahar et al. [194], even though it is still quite large compared with our calculated values.

The reason behind this might be related with the silicate phases used in different studies, for example, in both Shahar et al. [194] and Hin et al. [193], the equilibrium pressure was set at 1 GPa, the silicate phase could not be bridgmanite, but might be olivine instead. Thus, using the isotopic fractionation data from the low-pressure experimental range will overestimate the silicon isotope fractionation factor between silicate and metallic phase during the core-mantle segregation. Therefore, to better study the effect of core formation on silicon isotopic composition of the bulk silicate Earth (BSE) and bulk Earth (BE), or constrain the silicon content in the metallic core, an accurate silicon isotope fractionation factor at core-mantle segregation condition is required.

6.4.2 Implications for Si isotopic composition of BSE/BE and Si content in the core

With the knowledge of the silicon isotopic fractionation factor between bridgmanite and the metallic core, the silicon content in the Earth's core can be estimated by the mass balance principle if the silicon isotopic composition of BE and BSE is known. However, as summarized in Hin et al. [193], the choice for a silicon isotopic composition of the BE is relatively arbitrary. In addition, according to Huang et al. [191], as the structure of

Si-O polyhedron of upper and lower mantle minerals changes from CN=4 to CN=6, thus the silicon might fractionate among upper and lower mantle minerals. More specifically, the upper mantle might be isotopically heavier than the lower mantle in silicon isotope. Therefore, the isotopic composition of the upper mantle cannot be used to represent the lower mantle or the BSE.

To investigate the isotopic composition of the BSE, the amount of silicon in the metallic core, and whether BE is chondritic in silicon isotopes, two models are adopted here to check the silicon isotopic composition of BE and BSE. In the first model, the silicon isotopic composition of BSE is assumed known, for example, $\delta^{30}\,\mathrm{Si_{BSE}} = -0.34 \sim {}^{-}0.37\,‰$ [191], according to the mass balance principle, the relationship between $\delta^{30}\,\mathrm{Si_{BE}}$ and the silicon content in the core can be expressed by:

$$(\mathrm{f_{core}[Si]_{core}} + \mathrm{f_{BSE}[Si]_{BSE}})\delta^{30}\mathrm{Si_{BE}} = \mathrm{f_{core}[Si]_{core}}\,\delta^{30}\mathrm{Si_{core}} + \mathrm{f_{BSE}[Si]_{BSE}}\,\delta^{30}\mathrm{Si_{BSE}} \quad (6.3)$$

where $\mathrm{f_{BSE/core}}$ are the mass fractions of the BSE and the core; $\mathrm{[Si]_{BSE/core}}$ are the silicon content in these layers. According to McDonough [197] the $\mathrm{f_{BSE}}$=0.68, and $\mathrm{f_{core}}$=1-$\mathrm{f_{BSE}}$; and the content of silicon in the mantle is $\mathrm{[Si]_{BSE}}$=21.4%. The relationship between $\delta^{30}\,\mathrm{Si_{BE}}$ and silicon content in the core ($\mathrm{[Si]_{core}}$) are shown in figure 6.3(a), if the Earth is chondritic in silicon isotope, which equals approximately $-0.48\,‰$, then the silicon in the core required to be about 40 wt%. This value is much higher than the current best estimation, for example, 6 wt% [197]. Therefore, the Earth cannot be chondritic, or silicon isotopic composition of BSE estimated is inappropriate.

In the second model, BE is assumed to have chondritic silicon isotope composition, but the mantle is not homogeneous in silicon isotope, which means the silicon isotope can fractionate among upper mantle, lower mantle, and core. And we assume the silicon fractionated before the core-mantle segregation. Thus, the mass balance equation changes to:

$$\begin{aligned}(\mathrm{f_{core}[Si]_{core}} + \mathrm{f_{LM}[Si]_{LM}} + \mathrm{f_{UM}[Si]_{UM}})\delta^{30}\mathrm{Si_{BE}} = {} & \mathrm{f_{core}[Si]_{core}}\,\delta^{30}\mathrm{Si_{core}} \\ & + \mathrm{f_{LM}[Si]_{LM}}\,\delta^{30}\mathrm{Si_{LM}} \\ & + \mathrm{f_{UM}[Si]_{UM}}\,\delta^{30}\mathrm{Si_{UM}}\end{aligned} \quad (6.4)$$

where $\mathrm{f_{UM/LM/core}}$ are the mass fractions of the upper mantle, lower mantle, and the core;

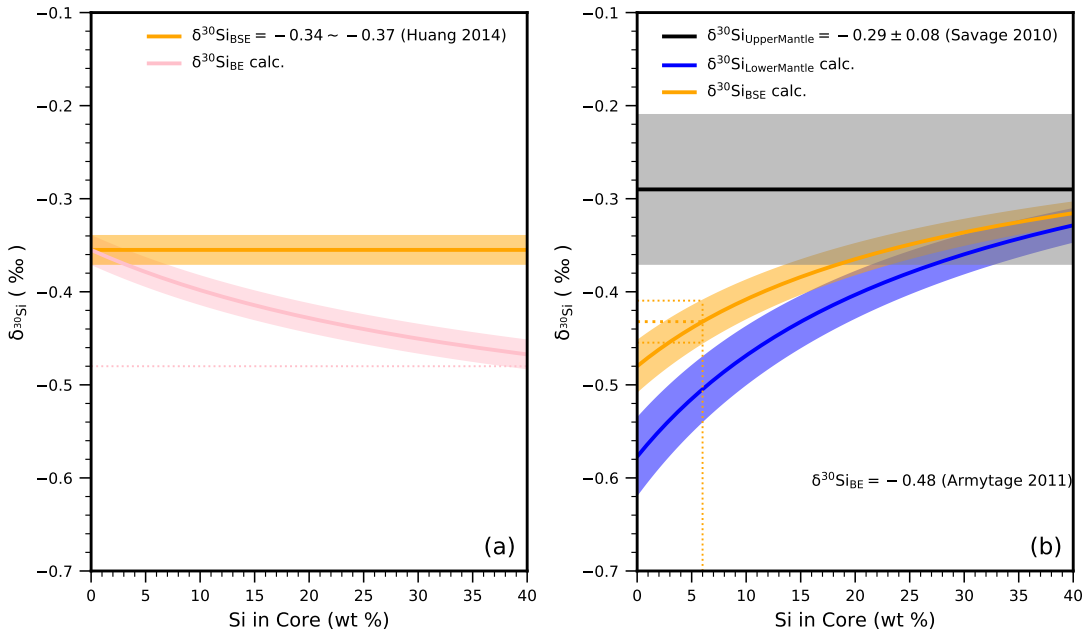

Figure 6.3: The relationship between the silicon isotope composition of different spheres of Earth and the Si content in the core (wt %) based on two models. (a) imagine the silicon isotopic composition of BSE is −0.34 ‰ to −0.37 ‰ based on the study from Huang et al. 2014, and derive the possible silicon isotopic composition of BE according to the calculated silicon isotope factor between silicate and metallic phases. (b) imagine the composition of BE is CI chondritic, mantle is not homogeneous, and there is silicon isotope fractionation between upper and lower mantle, and the isotope fractionation between lower mantle and metallic core are based on our calculation. Then the isotopic composition of lower mantle and BSE can be derived as a function of silicon content in the core based on the mass balance equation.

$[Si]_{UM/LM/core}$ are the silicon content in these layers. f_{UM}=0.23, and f_{LM}=0.45 according to McDonough [197]. The silicon isotope composition of BE, which has chondritic composition, and upper mantle are set to $-0.48\,‰$ [198] and $-0.29\,‰$, respectively. The relationship among silicon isotope composition of the lower mantle, BSE, and silicon content in the core ($[Si]_{core}$) are shown in figure 6.3(b). If we assume there is around 6 wt% silicon in the core, the $\delta^{30}\,Si_{BSE}$ should between $-0.41 \sim -0.45\,‰$, which is much lower than the estimation from previous studies [191, 194, 192].

From two different models described above, it seems that either the Earth is not chondritic in the silicon isotope or the current estimation of silicon isotopic composition of BSE is not accurate. Other possible explanations include fractionation might have occur during the early accretion, when light silicon isotopes evaporated into space, or during the big impact that occurred in the early history of Earth that could have added materials with heavy isotopes.

6.5 Conclusions

The silicon isotope fractionation factor between bridgmanite and the metallic phase has been determined from ab initio calculations, which is significantly smaller than the low-pressure experimental results. To study the isotope fractionation during the core-mantle segregation process, the silicate phase should be stable when the segregation process occurred. Using a lower pressure phase, for example olivine, might overestimate the silicon isotope fractionation factor between silicate and metallic phases. Our calculated results suggest that the Earth might not be chondritic in silicon isotopes, or the previously estimated silicon isotopic composition of BE and BSE are not accurate.

References

[1] Robin M Canup. Special Issue: Origin of Terrestrial Planets and the Earth–Moon System. *Physics Today*, 57(4):56–62, apr 2004.

[2] H. Palme and H.St.C. O'Neill. Cosmochemical Estimates of Mantle Composition. In *Treatise on Geochemistry*, volume 3, pages 1–39. Elsevier, 2014, 1312.1202.

[3] Daniel J Frost. The Upper Mantle and Transition Zone. *Elements*, 4(3):171–176, jun 2008.

[4] Donald J Weidner. Mantle Model Based on Measured Physical Properties of Minerals. In *Chemistry and physics of terrestrial planets*, pages 251–274. Springer, 1986.

[5] Craig R. Bina and Bernard J. Wood. Olivine-spinel transitions: Experimental and thermodynamic constraints and implications for the nature of the 400-km seismic discontinuity. *Journal of Geophysical Research*, 92(B6):4853, 1987.

[6] Craig R. Bina. Mutually consistent estimates of upper mantle composition from seismic velocity contrasts at 400 km depth. *Pure and Applied Geophysics PAGEOPH*, 141(1):101–109, 1993.

[7] A. E. Ringwood. *Composition and petrology of the earth's mantle.* New York : McGraw-Hill, 1975.

[8] Adam M. Dziewonski and Don L. Anderson. Preliminary reference Earth model. *Physics of the Earth and Planetary Interiors*, 25(4):297–356, jun 1981.

[9] B L N Kennett, E R Engdahl, and R Buland. Constraints on seismic velocities in the Earth from traveltimes. *Geophysical Journal International*, 122(1):108–124, jul 1995.

[10] D. R. Bell and G. R. Rossman. Water in Earth's Mantle: The Role of Nominally Anhydrous Minerals. *Science*, 255(5050):1391–1397, mar 1992.

[11] D. L. Kohlstedt, H. Keppler, and D. C. Rubie. Solubility of water in the α, β and γ phases of (Mg,Fe) 2 SiO 4. *Contributions to Mineralogy and Petrology*, 123(4):345–357, may 1996.

[12] Marc Hirschmann and David Kohlstedt. Water in Earth's mantle. *Physics Today*, 65(3):40, 2012.

[13] N. Bolfan-Casanova. Water in the Earth's mantle. *Mineralogical Magazine*, 69(3):229–258, jun 2005.

[14] D T Griggs and J D Blacic. Quartz: Anomalous Weakness of Synthetic Crystals. *Science*, 147(3655):292–295, jan 1965.

[15] David Griggs. Hydrolytic weakening of quartz and other silicates. *Geophysical Journal of the Royal Astronomical Society*, 14(506):19–31, 1967.

[16] Julian R Goldsmith. Al/Si interdiffusion in albite: effect of pressure and the role of hydrogen. *Contributions to Mineralogy and Petrology*, 95(3):311–321, mar 1987.

[17] Shun-ichiro Karato and Haemyeong Jung. Water, partial melting and the origin of the seismic low velocity and high attenuation zone in the upper mantle. *Earth and Planetary Science Letters*, 157(3-4):193–207, apr 1998.

[18] Shun-Ichiro Karato, Mervyn S. Paterson, and John D. FitzGerald. Rheology of synthetic olivine aggregates: Influence of grain size and water. *Journal of Geophysical Research*, 91(B8):8151, 1986.

[19] D. L. Kohlstedt. The Role of Water in High-Temperature Rock Deformation. *Reviews in Mineralogy and Geochemistry*, 62(1):377–396, 2006.

[20] S. J. Mackwell, D. L. Kohlstedt, and M. S. Paterson. The role of water in the deformation of olivine single crystals. *Journal of Geophysical Research*, 90(5):11319, 1985.

[21] S. Mei and D. L. Kohlstedt. Influence of water on plastic deformation of olivine aggregates: 1. Diffusion creep regime. *Journal of Geophysical Research: Solid Earth*, 105(B9):21457–21469, sep 2000.

[22] S. Mei and D. L. Kohlstedt. Influence of water on plastic deformation of olivine aggregates: 2. Dislocation creep regime. *Journal of Geophysical Research: Solid Earth*, 105(B9):21471–21481, sep 2000.

[23] Shun-ichiro Karato. The role of hydrogen in the electrical conductivity of the upper mantle. *Nature*, 347(6290):272–273, sep 1990.

[24] Greg Hirth and David L. Kohlstedt. Water in the oceanic upper mantle: implications for rheology, melt extraction and the evolution of the lithosphere. *Earth and Planetary Science Letters*, 144(1-2):93–108, oct 1996.

[25] Jacqueline E Dixon, T.H Dixon, D.R Bell, and R Malservisi. Lateral variation in upper mantle viscosity: role of water. *Earth and Planetary Science Letters*, 222(2):451–467, may 2004.

[26] Koichiro Umemoto, Renata M. Wentzcovitch, Marc M. Hirschmann, David L. Kohlstedt, and Anthony C. Withers. A first-principles investigation of hydrous defects and IR frequencies in forsterite: The case for Si vacancies. *American Mineralogist*, 96(10):1475–1479, oct 2011.

[27] David L. Kohlstedt and Stephen J. Mackwell. Diffusion of Hydrogen and Intrinsic Point Defects in Olivine. *Zeitschrift für Physikalische Chemie*, 207(Part_1_2):147–162, jan 1998.

[28] Brian L. Beard and Clark M. Johnson. Inter-mineral Fe isotope variations in mantle-derived rocks and implications for the Fe geochemical cycle. *Geochimica et Cosmochimica Acta*, 68(22):4727–4743, nov 2004.

[29] Stephen M Elardo and Anat Shahar. Non-chondritic iron isotope ratios in planetary mantles as a result of core formation. *Nature Geoscience*, 10(4):317–321, feb 2017.

[30] Jin Liu, Nicolas Dauphas, Mathieu Roskosz, Michael Y. Hu, Hong Yang, Wenli Bi, Jiyong Zhao, Esen E. Alp, Justin Y. Hu, and Jung-Fu Lin. Iron isotopic fractionation between silicate mantle and metallic core at high pressure. *Nature Communications*, 8(May 2016):14377, feb 2017.

[31] Franck Poitrasson. Does planetary differentiation really fractionate iron isotopes? *Earth and Planetary Science Letters*, 256(3-4):484–492, apr 2007.

[32] Veniamin B. Polyakov. Equilibrium Iron Isotope Fractionation at Core-Mantle Boundary Conditions. *Science*, 323(5916):912–914, feb 2009.

[33] James R Rustad and Qing-Zhu Yin. Iron isotope fractionation in the Earth's lower mantle. *Nature Geoscience*, 2(7):514–518, jul 2009.

[34] A. Shahar, E. A. Schauble, R. Caracas, A. E. Gleason, M. M. Reagan, Y. Xiao, J. Shu, and W. Mao. Pressure-dependent isotopic composition of iron alloys. *Science*, 352(6285):580–582, apr 2016.

[35] Paolo A. Sossi, Oliver Nebel, Mahesh Anand, and Franck Poitrasson. On the iron isotope composition of Mars and volatile depletion in the terrestrial planets. *Earth and Planetary Science Letters*, 449:360–371, 2016.

[36] Paolo A. Sossi, Oliver Nebel, and John Foden. Iron isotope systematics in planetary reservoirs. *Earth and Planetary Science Letters*, 452:295–308, oct 2016.

[37] Stefan Weyer, Ariel D. Anbar, Gerhard P. Brey, Carsten Münker, Klaus Mezger, and Alan B. Woodland. Iron isotope fractionation during planetary differentiation. *Earth and Planetary Science Letters*, 240(2):251–264, dec 2005.

[38] S. Weyer, A. D. Anbar, G. P. Brey, C. Münker, K. Mezger, and A. B. Woodland. Fe-isotope fractionation during partial melting on Earth and the current view on the Fe-isotope budgets of the planets (reply to the comment of F. Poitrasson and

to the comment of B.L. Beard and C.M. Johnson on "Iron isotope fractionation during planetary. *Earth and Planetary Science Letters*, 256(3-4):638–646, 2007.

[39] Hong Yang, Jung-Fu Lin, Michael Y. Hu, Mathieu Roskosz, Wenli Bi, Jiyong Zhao, Esen E. Alp, Jin Liu, Jiachao Liu, Renata M. Wentzowitch, Takuo Okuchi, and Nicolas Dauphas. Iron isotopic fractionation in mineral phases from Earth's lower mantle: Did terrestrial magma ocean crystallization fractionate iron isotopes? *Earth and Planetary Science Letters*, 506:113–122, jan 2019.

[40] Fang-Zhen Teng, Nicolas Dauphas, Shichun Huang, and Bernard Marty. Iron isotopic systematics of oceanic basalts. *Geochimica et Cosmochimica Acta*, 107:12–26, apr 2013.

[41] Paul R. Craddock, Jessica M. Warren, and Nicolas Dauphas. Abyssal peridotites reveal the near-chondritic Fe isotopic composition of the Earth. *Earth and Planetary Science Letters*, 365:63–76, mar 2013.

[42] Stefan Weyer and Dmitri A. Ionov. Partial melting and melt percolation in the mantle: The message from Fe isotopes. *Earth and Planetary Science Letters*, 259(1-2):119–133, 2007.

[43] Helen M. Williams, Bernard J. Wood, Jon Wade, Daniel J. Frost, and James Tuff. Isotopic evidence for internal oxidation of the Earth's mantle during accretion. *Earth and Planetary Science Letters*, 321-322:54–63, mar 2012.

[44] Franck Poitrasson, Alexander N. Halliday, Der-Chuen Lee, Sylvain Levasseur, and Nadya Teutsch. Iron isotope differences between Earth, Moon, Mars and Vesta as possible records of contrasted accretion mechanisms. *Earth and Planetary Science Letters*, 223(3-4):253–266, jul 2004.

[45] Remco C. Hin, Christopher D. Coath, Philip J. Carter, Francis Nimmo, Yi-Jen Lai, Philip A. E. Pogge von Strandmann, Matthias Willbold, Zoë M. Leinhardt, Michael J. Walter, and Tim Elliott. Magnesium isotope evidence that accretional vapour loss shapes planetary compositions. *Nature*, 549(7673):511–515, sep 2017.

[46] Han Hsu, Koichiro Umemoto, Matteo Cococcioni, and Renata M Wentzcovitch. The Hubbard U correction for iron-bearing minerals: A discussion based on

(Mg,Fe)SiO3 perovskite. *Physics of the Earth and Planetary Interiors*, 185(1-2):13–19, mar 2011.

[47] Han Hsu, Peter Blaha, Matteo Cococcioni, and Renata M. Wentzcovitch. Spin-State Crossover and Hyperfine Interactions of Ferric Iron in <math display="inline"> <msub> <mi>MgSiO</mi> <mn>3</mn> </msub> </math> Perovskite. *Physical Review Letters*, 106(11):118501, mar 2011.

[48] M. Born and R. Oppenheimer. Zur quantentheorie der molekeln. *Annalen der Physik*, 389(20):457–484, 1927.

[49] P. Hohenberg and W. Kohn. Inhomogeneous electron gas. *Phys. Rev.*, 136:B864–B871, Nov 1964.

[50] W. Kohn and L. J. Sham. Self-consistent equations including exchange and correlation effects. *Phys. Rev.*, 140:A1133–A1138, Nov 1965.

[51] D. M. Ceperley and B. J. Alder. Ground state of the electron gas by a stochastic method. *Phys. Rev. Lett.*, 45:566–569, Aug 1980.

[52] J. P. Perdew and Alex Zunger. Self-interaction correction to density-functional approximations for many-electron systems. *Phys. Rev. B*, 23:5048–5079, May 1981.

[53] John P Perdew and Yue Wang. Accurate and simple analytic representation of the electron-gas correlation energy. *Physical Review B*, 45(23):13244, 1992.

[54] John P. Perdew, Kieron Burke, and Matthias Ernzerhof. Generalized gradient approximation made simple. *Phys. Rev. Lett.*, 77:3865–3868, Oct 1996.

[55] ZhongQing Wu and WenZhong Wang. First-principles calculations of elasticity of minerals at high temperature and pressure. *Science China Earth Sciences*, 59(6):1107–1137, Jun 2016.

[56] D. R. Hamann, M. Schlüter, and C. Chiang. Norm-conserving pseudopotentials. *Phys. Rev. Lett.*, 43:1494–1497, Nov 1979.

[57] N. Troullier and José Luís Martins. Efficient pseudopotentials for plane-wave calculations. *Phys. Rev. B*, 43:1993–2006, Jan 1991.

[58] David Vanderbilt. Soft self-consistent pseudopotentials in a generalized eigenvalue formalism. *Phys. Rev. B*, 41:7892–7895, Apr 1990.

[59] Kari Laasonen, Alfredo Pasquarello, Roberto Car, Changyol Lee, and David Vanderbilt. Car-parrinello molecular dynamics with vanderbilt ultrasoft pseudopotentials. *Phys. Rev. B*, 47:10142–10153, Apr 1993.

[60] P. E. Blöchl. Projector augmented-wave method. *Phys. Rev. B*, 50:17953–17979, Dec 1994.

[61] G. Kresse and D. Joubert. From ultrasoft pseudopotentials to the projector augmented-wave method. *Phys. Rev. B*, 59:1758–1775, Jan 1999.

[62] Kanchan Sarkar, Mehmet Topsakal, NAW Holzwarth, and Renata M Wentzcovitch. Evolutionary optimization of paw data-sets for accurate high pressure simulations. *Journal of Computational Physics*, 347:39–55, 2017.

[63] R. P. Feynman. Forces in molecules. *Phys. Rev.*, 56:340–343, Aug 1939.

[64] Stefano Baroni, Stefano De Gironcoli, Andrea Dal Corso, and Paolo Giannozzi. Phonons and related crystal properties from density-functional perturbation theory. *Reviews of Modern Physics*, 73(2):515, 2001.

[65] Stefano Baroni, Paolo Giannozzi, and Eyvaz Isaev. Density-functional perturbation theory for quasi-harmonic calculations. *Reviews in Mineralogy and Geochemistry*, 71(1):39–57, 2010.

[66] Dario Alfè. Phon: A program to calculate phonons using the small displacement method. *Computer Physics Communications*, 180(12):2622–2633, 2009.

[67] Jean-Paul Poirier. *Introduction to the Physics of the Earth's Interior*. Cambridge University Press, 2000.

[68] Michael Berglund and Michael E Wieser. Isotopic compositions of the elements 2009 (iupac technical report). *Pure and applied chemistry*, 83(2):397–410, 2011.

[69] Pascal Richet, Yan Bottinga, and Marc Javoy. A review of hydrogen, carbon, nitrogen, oxygen, sulphur, and chlorine stable isotope fractionation among gaseous molecules. *Annual Review of Earth and Planetary Sciences*, 5(1):65–110, 1977.

[70] Harold C. Urey. The thermodynamic properties of isotopic substances. *J. Chem. Soc.*, pages 562–581, 1947.

[71] Jacob Bigeleisen and Maria Goeppert Mayer. Calculation of equilibrium constants for isotopic exchange reactions. *The Journal of Chemical Physics*, 15(5):261–267, 1947.

[72] Thomas Chacko, David R Cole, and Juske Horita. Equilibrium oxygen, hydrogen and carbon isotope fractionation factors applicable to geologic systems. *Reviews in mineralogy and geochemistry*, 43(1):1–81, 2001.

[73] Takanobu Ishida. Isotope effect and isotope separation: a chemist's view. *Journal of nuclear science and technology*, 39(4):407–412, 2002.

[74] Marc Blanchard, Etienne Balan, and Edwin A Schauble. Equilibrium fractionation of non-traditional isotopes: a molecular modeling perspective. *Reviews in Mineralogy and Geochemistry*, 82(1):27–63, 2017.

[75] B. B. Karki, R. M. Wentzcovitch, S. de Gironcoli, and S. Baroni. First-principles determination of elastic anisotropy and wave velocities of mgo at lower mantle conditions. *Science*, 286(5445):1705–1707, 1999, http://science.sciencemag.org/content/286/5445/1705.full.pdf.

[76] Renata M Wentzcovitch, Yonggang G Yu, and Zhongqing Wu. Thermodynamic properties and phase relations in mantle minerals investigated by first principles quasiharmonic theory. *Reviews in Mineralogy and Geochemistry*, 71(1):59–98, 2010.

[77] Renata M Wentzcovitch, Zhongqing Wu, and Pierre Carrier. First principles quasiharmonic thermoelasticity of mantle minerals. *Reviews in Mineralogy and Geochemistry*, 71(1):99–128, 2010.

[78] Michel L. Marcondes, Renata M. Wentzcovitch, and Lucy V.C. Assali. Importance of van der Waals interaction on structural, vibrational, and thermodynamic properties of NaCl. *Solid State Communications*, 273(November 2017):11–16, may 2018.

[79] Michel L Marcondes and Renata M Wentzcovitch. Hybrid ab-initio/experimental high temperature equations of state: Application to the nacl pressure scale. *Journal of Applied Physics*, 117(21):215902, 2015.

[80] Niladri Sengupta, Jefferson E Bates, and Adrienn Ruzsinszky. From semilocal density functionals to random phase approximation renormalized perturbation theory: A methodological assessment of structural phase transitions. *Physical Review B*, 97(23):235136, 2018.

[81] Zhongqing Wu, Renata M Wentzcovitch, Koichiro Umemoto, Baosheng Li, Kei Hirose, and Jin-Cheng Zheng. Pressure-volume-temperature relations inMgO: An ultrahigh pressure-temperature scale for planetary sciences applications. *Journal of Geophysical Research: Solid Earth*, 113(B6), 2008.

[82] Göran Grimvall. *Thermophysical properties of materials*. Elsevier, 1999.

[83] Liang-Feng Huang, Xue-Zeng Lu, Emrys Tennessen, and James M. Rondinelli. An efficient ab-initio quasiharmonic approach for the thermodynamics of solids. *Computational Materials Science*, 120:84 – 93, 2016.

[84] Duane C Wallace. *Thermodynamics of crystals*. Courier Corporation, 1998.

[85] Alberto Otero-de-la Roza, David Abbasi-Pérez, and Víctor Luaña. Gibbs2: A new version of the quasiharmonic model code. ii. models for solid-state thermodynamics, features and implementation. *Computer Physics Communications*, 182(10):2232–2248, 2011.

[86] Mauro Palumbo and Andrea Dal Corso. Lattice dynamics and thermophysical properties of hcp os and ru from the quasi-harmonic approximation. *Journal of Physics: Condensed Matter*, 29(39):395401, 2017.

[87] Atsushi Togo and Isao Tanaka. First principles phonon calculations in materials science. *Scripta Materialia*, 108:1–5, 2015.

[88] Renata M Wentzcovitch, Koichiro Umemoto, Taku Tsuchiya, and Jun Tsuchiya. Thermodynamic properties and stability field of $MgSiO_3$ post-perovskite. *Post-Perovskite: The Last Mantle Phase Transition*, pages 79–97, 2007.

[89] RM Wentzcovitch, BB Karki, M Cococcioni, and S De Gironcoli. Thermoelastic properties of $MgSiO_3$-perovskite: Insights on the nature of the earth's lower mantle. *Physical Review Letters*, 92(1):018501, 2004.

[90] Zhongqing Wu and Renata M Wentzcovitch. Quasiharmonic thermal elasticity of crystals: an analytical approach. *Physical Review B*, 83(18):184115, 2011.

[91] Koichiro Umemoto, Renata M Wentzcovitch, Stefano de Gironcoli, and Stefano Baroni. Order–disorder phase boundary between ice vii and viii obtained by first principles. *Chemical Physics Letters*, 499(4-6):236–240, 2010.

[92] Tian Qin, Renata M Wentzcovitch, Koichiro Umemoto, Marc M Hirschmann, and David L Kohlstedt. Ab initio study of water speciation in forsterite: Importance of the entropic effect. *American Mineralogist*, 103(5):692–699, 2018.

[93] Gaurav Shukla and Renata M Wentzcovitch. Spin crossover in $(Mg, Fe^{3+})(Si, Fe^{3+})O_3$ bridgmanite: Effects of disorder, iron concentration, and temperature. *Physics of the Earth and Planetary Interiors*, 260:53–61, 2016.

[94] P Giannozzi, O Andreussi, T Brumme, O Bunau, M Buongiorno Nardelli, M Calandra, R Car, C Cavazzoni, D Ceresoli, M Cococcioni, N Colonna, I Carnimeo, A Dal Corso, S de Gironcoli, P Delugas, R A DiStasio, A Ferretti, A Floris, G Fratesi, G Fugallo, R Gebauer, U Gerstmann, F Giustino, T Gorni, J Jia, M Kawamura, H-Y Ko, A Kokalj, E Küçükbenli, M Lazzeri, M Marsili, N Marzari, F Mauri, N L Nguyen, H-V Nguyen, A Otero-de-la Roza, L Paulatto, S Poncé, D Rocca, R Sabatini, B Santra, M Schlipf, A P Seitsonen, A Smogunov, I Timrov, T Thonhauser, P Umari, N Vast, X Wu, and S Baroni. Advanced capabilities for materials modelling with Quantum ESPRESSO. *Journal of Physics: Condensed Matter*, 29(46):465901, November 2017.

[95] Paolo Giannozzi, Stefano Baroni, Nicola Bonini, Matteo Calandra, Roberto Car, Carlo Cavazzoni, Davide Ceresoli, Guido L Chiarotti, Matteo Cococcioni, Ismaila Dabo, Andrea Dal Corso, Stefano de Gironcoli, Stefano Fabris, Guido Fratesi, Ralph Gebauer, Uwe Gerstmann, Christos Gougoussis, Anton Kokalj, Michele Lazzeri, Layla Martin-Samos, Nicola Marzari, Francesco Mauri, Riccardo Mazzarello, Stefano Paolini, Alfredo Pasquarello, Lorenzo Paulatto, Carlo Sbraccia,

Sandro Scandolo, Gabriele Sclauzero, Ari P Seitsonen, Alexander Smogunov, Paolo Umari, and Renata M Wentzcovitch. QUANTUM ESPRESSO: a modular and open-source software project for quantum simulations of materials. *Journal of Physics: Condensed Matter*, 21(39):395502, September 2009.

[96] J Hafner and G Kresse. The vienna ab-initio simulation program vasp: An efficient and versatile tool for studying the structural, dynamic, and electronic properties of materials. In *Properties of Complex Inorganic Solids*, pages 69–82. Springer, 1997.

[97] Xavier Gonze, J-M Beuken, R Caracas, F Detraux, M Fuchs, G-M Rignanese, Luc Sindic, Matthieu Verstraete, G Zerah, F Jollet, et al. First-principles computation of material properties: the abinit software project. *Computational Materials Science*, 25(3):478–492, 2002.

[98] Renata M Wentzcovitch. Invariant molecular-dynamics approach to structural phase transitions. *Physical Review B*, 44(5):2358, 1991.

[99] Renata M. Wentzcovitch, José Luís Martins, and G. D. Price. Ab initio molecular dynamics with variable cell shape: Application to MgSiO 3. *Physical Review Letters*, 70(25):3947–3950, jun 1993.

[100] N Troullier and José Luís Martins. Efficient pseudopotentials for plane-wave calculations. ii. operators for fast iterative diagonalization. *Physical Review B*, 43(11):8861, 1991.

[101] Koichiro Umemoto, Emiko Sugimura, Stefano de Gironcoli, Yoichi Nakajima, Kei Hirose, Yasuo Ohishi, and Renata M. Wentzcovitch. Nature of the volume isotope effect in ice. *Phys. Rev. Lett.*, 115:173005, Oct 2015.

[102] Guido Petretto, Shyam Dwaraknath, Henrique PC Miranda, Donald Winston, Matteo Giantomassi, Michiel J Van Setten, Xavier Gonze, Kristin A Persson, Geoffroy Hautier, and Gian-Marco Rignanese. High-throughput density-functional perturbation theory phonons for inorganic materials. *Scientific data*, 5:180065, 2018.

[103] R. F. Martin and G. Donnay. Hydroxyl in the mantle. *American Mineralogist*, 57:554–570, 1972.

[104] Joseph R. Smyth. A crystallographic model for hydrous wadsleyite (beta-Mg2 SiO4); an ocean in the Earth's interior? *American Mineralogist*, 79(9-10):1021–1024, 1994.

[105] D G Pearson, F E Brenker, F Nestola, J McNeill, L Nasdala, M T Hutchison, S Matveev, K Mather, G Silversmit, S Schmitz, B Vekemans, and L Vincze. Hydrous mantle transition zone indicated by ringwoodite included within diamond. *Nature*, 507(7491):221–224, mar 2014.

[106] Simon A Peacock. Fluid Processes in Subduction Zones. *Science*, 248(4953):329–337, apr 1990.

[107] E. Ohtani. Water in the Mantle. *Elements*, 1(1):25–30, jan 2005.

[108] William W Rubey. Geologic history of sea water An attempt to state the problem. *GSA Bulletin*, 62(9):1111–1148, sep 1951.

[109] Peter E. van Keken, Bradley R. Hacker, Ellen M. Syracuse, and Geoff A. Abers. Subduction factory: 4. Depth-dependent flux of H2O from subducting slabs worldwide. *Journal of Geophysical Research*, 116(B1):B01401, jan 2011.

[110] M. Nishi, T. Irifune, J. Tsuchiya, Y. Tange, Y. Nishihara, K. Fujino, and Y. Higo. Stability of hydrous silicate at high pressures and water transport to the deep lower mantle. *Nature Geoscience*, 7(3):224–227, feb 2014.

[111] Duojun Wang, Mainak Mookherjee, Yousheng Xu, and Shun-ichiro Karato. The effect of water on the electrical conductivity of olivine. *Nature*, 443(7114):977–980, oct 2006.

[112] Takashi Yoshino and Tomoo Katsura. Electrical Conductivity of Mantle Minerals: Role of Water in Conductivity Anomalies. *Annual Review of Earth and Planetary Sciences*, 41(1):605–628, may 2013.

[113] Neville L. Carter and Hans G. Ave'lallemant. High Temperature Flow of Dunite and Peridotite. *Geological Society of America Bulletin*, 81(8):2181, 1970, arXiv:1011.1669v3.

[114] P. N. Chopra and M. S. Paterson. The role of water in the deformation of dunite. *Journal of Geophysical Research: Solid Earth*, 89(B9):7861–7876, sep 1984.

[115] I. Kushiro. Effect of Water on the Composition of Magmas Formed at High Pressures. *Journal of Petrology*, 13(2):311–334, jun 1972.

[116] Kei Hirose. Melting experiments on Iherzolite KLB-1 under hydrous conditions and generation of high-magnesian andesitic melts. *Geology*, 25(1):42–44, 1997.

[117] Q Bai and D. L. Kohlstedt. Substantial hydrogen solubility in olivine and implications for water storage in the mantle. *Nature*, 357(6380):672–674, jun 1992.

[118] Quan Bai and D. L. Kohlstedt. Effects of chemical environment on the solubility and incorporation mechanism for hydrogen in olivine. *Physics and Chemistry of Minerals*, 19(7):460–471, 1993.

[119] S. Matveev, H. St. C. O'Neill, C. Ballhaus, W. R. Taylor, and D. H. Green. Effect of Silica Activity on OH- IR Spectra of Olivine: Implications for Low-aSiO2 Mantle Metasomatism. *Journal of Petrology*, 42(4):721–729, apr 2001.

[120] Andrew J. Berry, Jörg Hermann, Hugh S.C. O'Neill, and Garry J. Foran. Fingerprinting the water site in mantle olivine. *Geology*, 33(11):869, 2005.

[121] Joseph R Smyth and Steven D Jacobsen. Nominally anhydrous minerals and Earth's deep water cycle. In *Geophysical Monograph*, pages 1–11. American Geophysical Union, 2006.

[122] Yasuhiro Kudoh, Takahiro Kuribayashi, Hiroyuki Kagi, and Toru Inoue. Cation vacancy and possible hydrogen positions in hydrous forsterite, Mg1.985Si0.993H0.06O4, synthesized at 13.5 GPa and 1300 °C. *Journal of Mineralogical and Petrological Sciences*, 101(5):265–269, 2006.

[123] A. Hushur, M. H. Manghnani, Joseph R. Smyth, Fabrizio Nestola, and Daniel J. Frost. Crystal chemistry of hydrous forsterite and its vibrational properties up to 41 GPa. *American Mineralogist*, 94(5-6):751–760, may 2009.

[124] István Kovács, Hugh St C O'neIll, Jörg Hermann, and Erik H. Hauri. Site-specific infrared O-H absorption coefficients for water substitution into olivine. *American Mineralogist*, 95(2-3):292–299, 2010.

[125] Kazuhiko Otsuka and Shun-ichiro Karato. Control of the water fugacity at high pressures and temperatures: Applications to the incorporation mechanisms of water in olivine. *Physics of the Earth and Planetary Interiors*, 189(1-2):27–33, nov 2011.

[126] J. Ingrin, J. Liu, C. Depecker, S. C. Kohn, E. Balan, and K. J. Grant. Low-temperature evolution of OH bands in synthetic forsterite, implication for the nature of H defects at high pressure. *Physics and Chemistry of Minerals*, 40(6):499–510, 2013.

[127] Etienne Balan, Marc Blanchard, Michele Lazzeri, and Jannick Ingrin. Contribution of interstitial OH groups to the incorporation of water in forsterite. *Physics and Chemistry of Minerals*, 41(2):105–114, feb 2014.

[128] Peter M. E. Tollan, Rachel Smith, Hugh St.C. O'Neill, and Jörg Hermann. The responses of the four main substitution mechanisms of H in olivine to H2O activity at 1050 °C and 3 GPa. *Progress in Earth and Planetary Science*, 4(1):14, dec 2017.

[129] Marc Blanchard, Jannick Ingrin, Etienne Balan, István Kovács, and Anthony C. Withers. Effect of iron and trivalent cations on OH defects in olivine. *American Mineralogist*, 102(2):302–311, feb 2017.

[130] Nathalie Bolfan-Casanova, Gilles Montagnac, and Bruno Reynard. Measurement of water contents in olivine using Raman spectroscopy. *American Mineralogist*, 99(1):149–156, 2014.

[131] Simon C Kohn. Solubility of H20 in nominally anhydrous mantle minerals using IH MAS NMR. *American Mineralogist*, 81(11-12):1523–1526, dec 1996.

[132] Xianyu Xue, Masami Kanzaki, Doreen Turner, and Dominik Loroch. Hydrogen incorporation mechanisms in forsterite: New insights from 1 H and 29 Si NMR spectroscopy and first-principles calculation. *American Mineralogist*, 102(3):519–536, mar 2017.

[133] Kate Wright and C.R.A. Catlow. A computer simulation study of (OH) defects in olivine. *Physics and Chemistry of Minerals*, 20(7):515–518, jan 1994.

[134] John Brodholt. Ab initio calculations on point defects in forsterite (Mg2SiO4) and implications for diffusion and creep. *American Mineralogist*, 82(11-12):1049–1053, 1997.

[135] Michael Haiber, Pietro Ballone, and Michele Parrinello. Structure and dynamics of protonated Mg2SiO4: An ab-initio molecular dynamics study. *American Mineralogist*, 82(9-10):913–922, 1997.

[136] J. Spencer Braithwaite, Peter V. Sushko, Kate Wright, and C. Richard A. Catlow. Hydrogen defects in Forsterite: A test case for the embedded cluster method. *The Journal of Chemical Physics*, 116(6):2628–2635, feb 2002.

[137] J. Spencer Braithwaite, Kate Wright, and C. Richard A. Catlow. A theoretical study of the energetics and IR frequencies of hydroxyl defects in forsterite. *Journal of Geophysical Research: Solid Earth*, 108(B6):2284, jun 2003.

[138] Andrew M. Walker, Sylvie Demouchy, and Kate Wright. Computer modelling of the energies and vibrational properties of hydroxyl groups in α- and β-Mg2SiO4. *European Journal of Mineralogy*, 18(5):529–543, 2006.

[139] a. M. Walker, J. Hermann, a. J. Berry, and H. St C O'Neill. Three water sites in upper mantle olivine and the role of titanium in the water weakening mechanism. *Journal of Geophysical Research*, 112(B5):B05211, may 2007.

[140] John P. Brodholt and Keith Refson. An ab initio study of hydrogen in forsterite and a possible mechanism for hydrolytic weakening. *Journal of Geophysical Research: Solid Earth*, 105(B8):18977–18982, aug 2000.

[141] F.A. Kröger and H.J. Vink. Relations between the concentrations of imperfections in crystalline solids. In *Solid state physics*, volume 3, pages 307–435. Elsevier, 1956.

[142] S. Demouchy and S. Mackwell. Water diffusion in synthetic iron-free forsterite. *Physics and Chemistry of Minerals*, 30(8):486–494, sep 2003.

[143] C. Lemaire, S. C. Kohn, and R. a. Brooker. The effect of silica activity on the incorporation mechanisms of water in synthetic forsterite: A polarised infrared spectroscopic study. *Contributions to Mineralogy and Petrology*, 147(1):48–57, 2004.

[144] Etienne Balan, Marc Blanchard, Michele Lazzeri, and Jannick Ingrin. Theoretical Raman spectrum and anharmonicity of tetrahedral OH defects in hydrous forsterite. *European Journal of Mineralogy*, 29(2):201–212, apr 2017.

[145] Céline Crépisson, Hélène Bureau, Marc Blanchard, Jannick Ingrin, and Etienne Balan. Theoretical infrared spectrum of partially protonated cationic vacancies in forsterite. *European Journal of Mineralogy*, 26(2):203–210, mar 2014.

[146] Andrea Dal Corso, Stefano Baroni, Raffaele Resta, and Stefano de Gironcoli. Ab initio calculation of phonon dispersions in II-VI semiconductors. *Physical Review B*, 47(7):3588, 1993.

[147] Koichiro Umemoto, Renata M. Wentzcovitch, Yonggang G. Yu, and Ryan Requist. Spin transition in (Mg,Fe)SiO3 perovskite under pressure. *Earth and Planetary Science Letters*, 276(1-2):198–206, nov 2008.

[148] K. Umemoto. Computer Simulations on Phase Transitions in Ice. *Reviews in Mineralogy and Geochemistry*, 71(1):315–335, jan 2010.

[149] Yonggang G. Yu, Zhongqing Wu, and Renata M. Wentzcovitch. α–β–γ transformations in Mg2SiO4 in Earth's transition zone. *Earth and Planetary Science Letters*, 273(1-2):115–122, aug 2008.

[150] Yonggang G. Yu, Renata M. Wentzcovitch, and Ross J. Angel. First principles study of thermodynamics and phase transition in low-pressure (P21/c) and high-pressure (C2/c) clinoenstatite MgSiO3. *Journal of Geophysical Research: Solid Earth*, 115(2):1–10, 2010.

[151] Ashok K Verma and Bijaya B Karki. Ab initio investigations of native and protonic point defects in Mg₂SiO₄ polymorphs under high pressure. *Earth and Planetary Science Letters*, 285(1-2):140–149, jul 2009.

[152] Etienne Balan, Jannick Ingrin, Simon Delattre, István Kovács, and Marc Blanchard. Theoretical infrared spectrum of OH-defects in forsterite. *European Journal of Mineralogy*, 23(3):285–292, jun 2011.

[153] Koichiro Umemoto and Renata M. Wentzcovitch. Amorphization in quenched ice VIII: A first-principles study. *Physical Review B*, 69(18):180103, may 2004.

[154] Koichiro Umemoto and Renata M. Wentzcovitch. Theoretical study of the isostructural transformation in ice VIII. *Physical Review B*, 71(1):012102, jan 2005.

[155] Koichiro Umemoto, Emiko Sugimura, Stefano de Gironcoli, Yoichi Nakajima, Kei Hirose, Yasuo Ohishi, and Renata M. Wentzcovitch. Nature of the Volume Isotope Effect in Ice. *Physical Review Letters*, 115(17):173005, oct 2015.

[156] X.-z. Yang and Hans Keppler. In-situ infrared spectra of OH in olivine to 1100 C. *American Mineralogist*, 96(2-3):451–454, feb 2011.

[157] Ronny Schoenberg and Friedhelm von Blanckenburg. Modes of planetary-scale Fe isotope fractionation. *Earth and Planetary Science Letters*, 252(3-4):342–359, dec 2006.

[158] H. M. Williams, A. Markowski, G. Quitté, A. N. Halliday, N. Teutsch, and S. Levasseur. Fe isotope fractionation in iron meteorites: New insights into metal-sulphide segregation and planetary accretion. *Earth and Planetary Science Letters*, 250(3-4):486–500, 2006.

[159] Remco C Hin, Max W Schmidt, and Bernard Bourdon. Experimental evidence for the absence of iron isotope fractionation between metal and silicate liquids

at 1 gpa and 1250–1300 c and its cosmochemical consequences. *Geochimica et Cosmochimica Acta*, 93:164–181, 2012.

[160] Franck Poitrasson, Mathieu Roskosz, and Alexandre Corgne. No iron isotope fractionation between molten alloys and silicate melt to 2000 °C and 7.7 GPa: Experimental evidence and implications for planetary differentiation and accretion. *Earth and Planetary Science Letters*, 278(3-4):376–385, 2009.

[161] Jan A. Schuessler, Ronny Schoenberg, and Olgeir Sigmarsson. Iron and lithium isotope systematics of the Hekla volcano, Iceland — Evidence for Fe isotope fractionation during magma differentiation. *Chemical Geology*, 258(1-2):78–91, jan 2009.

[162] Franck Poitrasson, Sylvain Levasseur, and Nadya Teutsch. Significance of iron isotope mineral fractionation in pallasites and iron meteorites for the core–mantle differentiation of terrestrial planets. *Earth and Planetary Science Letters*, 234(1-2):151–164, 2005.

[163] Krystle Catalli, Sang-Heon Shim, Vitali B. Prakapenka, Jiyong Zhao, Wolfgang Sturhahn, Paul Chow, Yuming Xiao, Haozhe Liu, Hyunchae Cynn, and William J. Evans. Spin state of ferric iron in MgSiO3 perovskite and its effect on elastic properties. *Earth and Planetary Science Letters*, 289(1-2):68–75, jan 2010.

[164] Kiyoshi Fujino, Daisuke Nishio-Hamane, Yusuke Seto, Nagayoshi Sata, Takaya Nagai, Toru Shinmei, Tetsuo Irifune, Hirofumi Ishii, Nozomu Hiraoka, Yong Q Cai, et al. Spin transition of ferric iron in al-bearing mg–perovskite up to 200gpa and its implication for the lower mantle. *Earth and Planetary Science Letters*, 317:407–412, 2012.

[165] Kiyoshi Fujino, Daisuke Nishio-Hamane, Takaya Nagai, Yusuke Seto, Yasuhiro Kuwayama, Matthew Whitaker, Hiroaki Ohfuji, Toru Shinmei, and Tetsuo Irifune. Spin transition, substitution, and partitioning of iron in lower mantle minerals. *Physics of the Earth and Planetary Interiors*, 228:186–191, mar 2014.

[166] Daisuke Nishio-Hamane, Takaya Nagai, Kiyoshi Fujino, Yusuke Seto, and Naoto Takafuji. Fe3+ and al solubilities in mgsio3 perovskite: implication of the fe3+

alo3 substitution in mgsio3 perovskite at the lower mantle condition. *Geophysical research letters*, 32(16), 2005.

[167] N. Dauphas, M. Roskosz, E.E. Alp, D.C. Golden, C.K. Sio, F.L.H. Tissot, M.Y. Hu, J. Zhao, L. Gao, and R.V. Morris. A general moment NRIXS approach to the determination of equilibrium Fe isotopic fractionation factors: Application to goethite and jarosite. *Geochimica et Cosmochimica Acta*, 94:254–275, oct 2012.

[168] Matteo Cococcioni and Stefano de Gironcoli. Linear response approach to the calculation of the effective interaction parameters in the <math display="inline"> <mrow> <mi>LDA</mi> <mo>+</mo> <mi mathvariant="normal">U</mi> </mrow> </math> method. *Physical Review B*, 71(3):035105, jan 2005.

[169] Han Hsu, Koichiro Umemoto, Matteo Cococcioni, and Renata Wentzcovitch. First-principles study for low-spin <math display="inline"> <mrow> <msub> <mrow> <mtext>LaCoO</mtext> </mrow> <mn>3</mn> </msub> </mrow> </math> with a structurally consistent Hubbard <math display="inline"> <mi>U</mi> </math>. *Physical Review B*, 79(12):125124, mar 2009.

[170] Heather J. Kulik, Matteo Cococcioni, Damian A. Scherlis, and Nicola Marzari. Density functional theory in transition-metal chemistry: A self-consistent hubbard U approach. *Physical Review Letters*, 97(10):1–4, 2006, 0608285.

[171] Gaurav Shukla and Renata M. Wentzcovitch. Spin crossover in (Mg,Fe3+)(Si,Fe3+)O3 bridgmanite: Effects of disorder, iron concentration, and temperature. *Physics of the Earth and Planetary Interiors*, 260:53–61, nov 2016.

[172] Gaurav Shukla, Matteo Cococcioni, and Renata M Wentzcovitch. Thermoelasticity of Fe 3+ - and Al-bearing bridgmanite: Effects of iron spin crossover. *Geophysical Research Letters*, 43(11):5661–5670, jun 2016.

[173] Hendrik J Monkhorst and James D Pack. Special points for Brillouin-zone integrations. *Physical Review B*, 13(12):5188–5192, jun 1976.

[174] A. Floris, S. de Gironcoli, E. K U Gross, and M. Cococcioni. Vibrational properties of MnO and NiO from DFT +U -based density functional perturbation theory. *Physical Review B*, 84(16):161102, oct 2011.

[175] Gaurav Shukla, Mehmet Topsakal, and Renata M. Wentzcovitch. Spin crossovers in iron-bearing MgSiO3 and MgGeO3: Their influence on the post-perovskite transition. *Physics of the Earth and Planetary Interiors*, 249:11–17, dec 2015.

[176] Julien Siebert, James Badro, Daniele Antonangeli, and Frederick J. Ryerson. Metal–silicate partitioning of Ni and Co in a deep magma ocean. *Earth and Planetary Science Letters*, 321-322:189–197, mar 2012.

[177] J. Siebert, J. Badro, D. Antonangeli, and F. J. Ryerson. Terrestrial Accretion Under Oxidizing Conditions. *Science*, 339(6124):1194–1197, mar 2013.

[178] Fei Wu, Tian Qin, Xuefang Li, Yun Liu, Jen-How Huang, Zhongqing Wu, and Fang Huang. First-principles investigation of vanadium isotope fractionation in solution and during adsorption. *Earth and Planetary Science Letters*, 426:216–224, sep 2015.

[179] Chongqin Feng, Tian Qin, Shichun Huang, Zhongqing Wu, and Fang Huang. First-principles investigations of equilibrium calcium isotope fractionation between clinopyroxene and Ca-doped orthopyroxene. *Geochimica et Cosmochimica Acta*, 143:132–142, oct 2014.

[180] Tian Qin, Fei Wu, Zhongqing Wu, and Fang Huang. First-principles calculations of equilibrium fractionation of O and Si isotopes in quartz, albite, anorthite, and zircon. *Contributions to Mineralogy and Petrology*, 171(11):91, nov 2016.

[181] Edwin A Schauble. First-principles estimates of equilibrium magnesium isotope fractionation in silicate, oxide, carbonate and hexaaquamagnesium(2+) crystals. *Geochimica Et Cosmochimica Acta*, 75(3):844–869, 2011.

[182] Koichiro Umemoto, Han Hsu, and Renata M. Wentzcovitch. Effect of site degeneracies on the spin crossovers in (Mg, Fe)SiO3 perovskite. *Physics of the Earth and Planetary Interiors*, 180(3-4):209–214, 2010.

[183] Jung-Fu Lin, Zhu Mao, Jing Yang, Jin Liu, Yuming Xiao, Paul Chow, and Takuo Okuchi. High-spin fe2+ and fe3+ in single-crystal aluminous bridgmanite in the lower mantle. *Geophysical Research Letters*, 43(13):6952–6959, 2016, https://agupubs.onlinelibrary.wiley.com/doi/pdf/10.1002/2016GL069836.

[184] Jennifer M Jackson, Wolfgang Sturhahn, Guoyin Shen, Jiyong Zhao, Michael Y Hu, Daniel Errandonea, Jay D Bass, and Yingwei Fei. A synchrotron mossbauer spectroscopy study of (mg, fe) sio3 perovskite up to 120 gpa. *American Mineralogist*, 90(1):199–205, 2005.

[185] J Li, W Sturhahn, JM Jackson, VV Struzhkin, JF Lin, J Zhao, HK Mao, and G Shen. Pressure effect on the electronic structure of iron in (mg, fe)(si, al) o 3 perovskite: A combined synchrotron mössbauer and x-ray emission spectroscopy study up to 100 gpa. *Physics and Chemistry of Minerals*, 33(8-9):575–585, 2006.

[186] Jung-Fu Lin, Heather Watson, György Vankó, Esen E Alp, Vitali B Prakapenka, Przemek Dera, Viktor V Struzhkin, Atsushi Kubo, Jiyong Zhao, Catherine McCammon, et al. Intermediate-spin ferrous iron in lowermost mantle post-perovskite and perovskite. *Nature geoscience*, 1(10):688, 2008.

[187] C. McCammon, I Kantor, O Narygina, J Rouquette, U Ponkratz, I Sergueev, M Mezouar, V Prakapenka, and L Dubrovinsky. Stable intermediate-spin ferrous iron in lower-mantle perovskite. *Nature Geoscience*, 1(10):684–687, oct 2008.

[188] Han Hsu, Koichiro Umemoto, Peter Blaha, and Renata M Wentzcovitch. Spin states and hyperfine interactions of iron in (mg, fe) sio3 perovskite under pressure. *Earth and Planetary Science Letters*, 294(1-2):19–26, 2010.

[189] W.F. McDonough. Compositional Model for Earth's Core. *Treatise on Geochemistry*, pages 547–568, 2003.

[190] Kun Wang, Frédéric Moynier, Nicolas Dauphas, Jean-Alix Barrat, Paul Craddock, and Corliss K. Sio. Iron isotope fractionation in planetary crusts. *Geochimica et Cosmochimica Acta*, 89:31–45, jul 2012.

[191] F. Huang, Zhongqing Wu, Shichun Huang, and Fei Wu. First-principles calculations of equilibrium silicon isotope fractionation among mantle minerals. *Geochimica et Cosmochimica Acta*, 140:509–520, September 2014.

[192] R. Bastian Georg, Alex N. Halliday, Edwin A. Schauble, and Ben C. Reynolds. Silicon in the Earth's core. *Nature*, 447(7148):1102–1106, June 2007.

[193] Remco C. Hin, Caroline Fitoussi, Max W. Schmidt, and Bernard Bourdon. Experimental determination of the Si isotope fractionation factor between liquid metal and liquid silicate. *Earth and Planetary Science Letters*, 387:55–66, February 2014.

[194] Anat Shahar, Karen Ziegler, Edward D. Young, Angele Ricolleau, Edwin A. Schauble, and Yingwei Fei. Experimentally determined Si isotope fractionation between silicate and Fe metal and implications for Earth's core formation. *Earth and Planetary Science Letters*, 288(1-2):228–234, October 2009.

[195] Anat Shahar, Valerie J. Hillgren, Edward D. Young, Yingwei Fei, Catherine A. Macris, and Liwei Deng. High-temperature Si isotope fractionation between iron metal and silicate. *Geochimica et Cosmochimica Acta*, 75(23):7688–7697, December 2011.

[196] Karen Ziegler, Edward D. Young, Edwin A. Schauble, and John T. Wasson. Metal–silicate silicon isotope fractionation in enstatite meteorites and constraints on Earth's core formation. *Earth and Planetary Science Letters*, 295(3-4):487–496, July 2010.

[197] W.F. McDonough. Compositional Model for the Earth's Core. In *Treatise on Geochemistry*, pages 559–577. Elsevier, 2014.

[198] R.M.G. Armytage, R.B. Georg, P.S. Savage, H.M. Williams, and A.N. Halliday. Silicon isotopes in meteorites and planetary core formation. *Geochimica et Cosmochimica Acta*, 75(13):3662–3676, July 2011.

Appendix A

Acronyms

Care has been taken in this thesis to minimize the use of jargon and acronyms, but this cannot always be achieved. This appendix defines jargon terms in a glossary, and contains a table of acronyms and their meaning.

A.1 Acronyms

Table A.1: Acronyms

Acronym	Meaning
DFT	density functional theory
DFPT	density functional perturbation theory
HA	harmonic approximation
QHA	quasi harmonic approximation
EOS	equation of state
VDOS	vibrational density of state
NAMs	nominally anhydrous minerals
HCP	hexagonal close-packed
BE	bulk Earth
BSE	bulk silicate Earth